Nanoscale Electron Spin Resonance

Von der Fakultät 8 Mathematik und Physik der Universität Stuttgart zur
Erlangung der Würde eines Doktors der Naturwissenschaften
(Dr. rer. nat.) genehmigte Abhandlung

Vorgelegt von

LUKAS SCHLIPF

aus Aalen

Hauptberichter:	Prof. Dr. Jörg Wrachtrup
Mitberichter:	Prof. Dr. Klaus Kern

Tag der mündlichen Prüfung:	9. Oktober 2017

3. Physikalisches Institut der Universität Stuttgart

2017

Du kannst für eine Weile dein Umfeld belügen, doch dein eigenes Herz wirst du nicht betrügen.
Man erntet, was man sät -
drum wird's dein Herz sein, das dich verrät.

Die Ärzte, Lied vom Scheitern

Summary

Modern technologies are becoming increasingly reliant on effects which occur on nanometer length-scales. For example, the critical dimensions in commercially available silicon-based integrated-circuits have already breached the 10 nm limit. Another example can be found in the field of pharmaceutics, where properties of single-protein molecules now pose boundaries on their function. Hence, techniques which investigate materials on the nanoscale have become steadily more and more important to communities even outside of basic academic interest. In particular, the properties of electromagnetism greatly vary in form and strength when going from the macro- to the nanoscale. A proper understanding of magnetism at ever shrinking sizes is necessary for the development of current technologies, such as medical imaging, data storage and emerging ones, namely quantum computation. Here, our classical measurement techniques start to break down and quantum-mechanical effects, observable only at very small dimensions, affect our interpretation of magnetic fields emanating from single molecules, atoms or electrons. This has, in recent years, sparked an interest in the development of devices now popularly known as quantum sensors.

Such a sensor, which exploits quantum effects, is the nitrogen-vacancy (NV–) center in diamond. This defect allows for the optical fluorescence readout of its electron's spin state, which can then be manipulated to any desired state using microwave radiation. These key features of high fidelity readout and manipulation of a single spin together with the ability to produce stable single NV–centers a few nanometers below the diamond surface have enabled their application as versatile sensors in different fields. Apart from the ability to detect electric fields, temperature changes and pressure variations with high sensitivity, sensing of nuclear spins and single electron spins in nanometer-sized volumes has been demonstrated. The possibility to detect single spins is particularly exciting since only a few other techniques have come close to this limit. Nonetheless, single spin sensitivity is necessary for a deeper understanding of, for example, quantum communication, and will answer open questions in e.g. medicine through investigations of single molecules.

The presented thesis significantly advances the field of nanoscale electron spin resonance on arbitrary samples by using NV–centers as quantum sensors for magentic fields. While other proof of principle studies have established the possibility to sense electron spins outside the diamond [1] and to perform measurements on a single electron spin attached to a molecule [2], here it is shown for the first time that a virtually unlimited stability of coupled molecules on the diamond surface can be reached at cryogenic conditions. This stability allows for the development of novel sensing schemes which enable readout and manipulation of very few external spins and their dipolar coupling.

Over the course of this thesis, the NV–center will be established as a tool for the detection and readout of electron spins outside the diamond lattice. A sensitivity of less than 10 electron spins attached to molecules and the measurement of their dipolar coupling is demonstrated in this work. In chapter 2 the relevant theoretical framework of NV–center physics and applications for understanding and achieving these results are discussed, while in chapter 3 the experimental apparatus and its unique properties are presented. An application of the versatility of the introduced sensing protocols is outlined in chapter 4 by tracking the temperature dynamics of single ferritin molecules over a large frequency range. Although this demonstrated sensitivity surpasses what can be achieved with most other techniques, a double resonance technique for sensing electron spins is established to enhance the sensitivity from a magnetic moment of $300\ \mu_B$ to even a single electron spin. This method is then applied to sense dangling bond spins on the diamond surface. Finally in chapter 5, double resonance spectroscopy is used to detect the coupling of an NV–center to less than 10 nitroxide spin labels attached to polyproline peptides. For the first time, the extraction of the specific, predetermined coupling between these spin labels by the means of NV magnetometry is shown.

Zusammenfassung

Moderne Technologien basieren zunehmend auf Effekten, die sich auf Längenskalen von Nanometern abspielen. Beispielsweise haben kritische Dimensionen in kommerziellen Silizium-basierten integrierten Schaltkreisen die Größe von 10 nm unterschritten. Ein anderes Beispiel ist die moderne Pharmazie, in der Eigenschaften einzelner Proteine Randbedingungen für ihr Verhalten festlegen. Folglich werden Techniken für Untersuchungen auf der Nanoskala zunehmend wichtiger, auch außerhalb rein akademischer Interessengebiete. Speziell elektromagnetische Phänomene unterscheiden sich in hohem Maße in Erscheinung und Stärke, wenn man von der Makro- zur Nanoskala wechselt. Das Verständnis von Magnetismus in immer kleiner werdenden Dimensionen ist notwendig für die Entwicklung von modernen Technologien, wie Bildgebung in der Medizin und Datenspeicherung, oder gerade entstehenden Technologien, wie dem Quantencomputer. Dabei sind klassische Messtechniken meist unzureichend und quantenmechanische Effekte, die nur auf kleinsten Skalen auftreten, müssen bei der Interpretation von magnetischen Feldern beachtet werden, die von einzelnen Molekülen, Atomen oder Elektronen ausgehen. In den letzten Jahren hat dies zu regem Interesse an der Entwicklung von Instrumenten geführt, die heute häufig als Quanten-Sensoren bekannt sind.

Solch ein Sensor, der Quanteneffekte ausnutzt, ist das Stickstoff-Fehlstellen (NV–) Zentrum in Diamant. Dieser Defekt erlaubt die optische Fluoreszenz-Auslese seines elektronischen Spinzustandes, welcher dann mit Mikrowellenstrahlung in jeden erdenklichen Zustand gebracht werden kann. Die Möglichkeiten der genauen Auslese und Manipulation eines einzelnen Spins, zusammen mit der Fähigkeit einzelne, stabile NV–Zentren nur wenige Nanometer unterhalb der Diamantenoberfläche zu produzieren, haben ihre Anwendung als vielseitige Sensoren in unterschiedlichen Gebieten ermöglicht. Abgesehen von der Fähigkeit elektrische Felder, Temperaturschwankungen und Druckveränderungen mit hoher Empfindlichkeit zu detektieren, wurden mit dem NV–Zentrum Kernspins und einzelne Elektronenspins in Volumina weniger Kubiknanometer nachgewiesen. Die Möglichkeit einzelne Spins zu detektieren ist besonders interessant, da dieses Limit nur von wenigen anderen Techniken erreicht wird. Nichtsdestotrotz ist es durchaus notwendig einzelne Spins zu detektieren, um zum Beispiel ein besseres Verständnis von Quantenkommunikation zu erreichen. Zusätzlich können durch die Untersuchung einzelner Moleküle offene Fragen in der Medizin beantwortet werden.

Die vorliegende Arbeit leistet einen entscheidenden Beitrag zum Feld der Elektronenspinresonanz auf der Nanoskala, indem NV–Zentren als Quantensensoren für Magnetfelder von beliebigen Systemen benutzt werden. Während andere grundlegende Experimente gezeigt haben, dass es möglich ist Elektronenspins außerhalb des Diamanten zu detektieren [1] und Messungen an einem einzelnen Elektronenspin, der an ein Molekül angebunden ist, durchzuführen [2], wird hier zum ersten Mal gezeigt, dass eine nahezu unbegrenzte Stabilität der gekoppelten Moleküle auf der Diamantenoberfläche bei tiefen Temperaturen erreicht werden kann. Diese Stabilität ermöglicht die Entwicklung neuer Detektions-Schemata, welche das Lesen und Manipulieren sehr weniger externer Spins, inklusive ihrer dipolaren Kopplung, erlauben.

Im Verlaufe dieser Dissertation wird das NV–Zentrum als Hilfsmittel zur Detektion und Auslese von Elektronenspins etabliert, die sich außerhalb des Diamanten befinden. Dabei wird in dieser Arbeit eine Empfindlichkeit von weniger als 10 Elektronenspins, die an Molekülen angebracht sind und die Messung ihrer dipolaren Wechselwirkung demonstriert. In Kapitel 2 werden die relevanten theoretischen Grundlagen und Anwendungen der Physik von NV–Zentren diskutiert, die zum Verständnis der Ergebnisse notwendig sind, während in Kapitel 3 der experimentelle Aufbau und seine einzigartigen Merkmale vorgestellt werden. In Kapitel 4 wird die Vielseitigkeit der eingeführten Detektions-Protokolle demonstriert, indem die Temperatur-Dynamik von einzelnen Ferritin-Molekülen über einen breiten Frequenzbereich verfolgt wird. Obwohl die so nachgewiesene Empfindlichkeit bereits das übersteigt, was mit vielen anderen Techniken erreicht werden kann, wird eine Doppelresonanz-Technik zur Detektion von Elektronenspins vorgestellt, die die Empfindlichkeit von einem magnetischen Moment von $300\mu_B$ auf das magnetische Moment eines einzelnen Elektronenspins erhöht. Diese Methode wird dann dazu benutzt, ungebundene Zustände auf der Diamantenoberfläche nachzuweisen. Schließlich wird diese Doppelresonanz-Spektroskopie in Kapitel 5 dazu verwendet, die Kopplung eines NV–Zentrums mit weniger als 10 Nitroxid-Spinmarkern, die an Polyprolin-Peptide angebunden sind, zu detektieren. Zum ersten Mal wird hier gezeigt, dass man mittels NV Magnetometrie die spezifisch vorbestimmte Kopplung zwischen diesen Spinmarkern herausfinden kann.

Contents

1. Introduction

In their Nobel Prize winning experiment Otto Stern and Walther Gerlach observed in 1922, that atoms must possess an attribute that makes them align along a magnetic field in two discrete or *quantized* directions [3]. Later, theoretically formulated by Pauli in 1927 and derived in Dirac's equation in 1928, this attribute termed quantum spin is in essence a postulate that needs to be made in the framework of quantum mechanics to rationalize the properties and behavior of quantum-mechanical particles that carry charge. Using a classical analogue, spin can be rationalized with the magnetic moment of a pointlike, charged, rotating particle and is integral in the explanation of magnetism on the nanoscale. Today quantum mechanical spin is of utmost importance for the understanding, development and advancement of modern applications.

The way single spins behave and interact has, for example, large implications in modern information technology, for example giving rise to the field of spintronics where the spin degree of freedom is exploited for electronic transport [4]. The size of a single commercial transistor in silicon chips currently approaches 10 nm, where quantum tunneling starts to be significant and further down-scaling becomes increasingly difficult. As the classical computer is entering the quantum realm, quantum properties can be harnessed to construct a so-called quantum computer, which holds the promise to significantly increase computation speed for specific problems [5]. The realization of quantum computers is currently a widely pursued goal in research and one possible design is an interacting network of single spins [6]. It is required to study and control single spins among such a quantum spin network to use it for quantum computing applications. To find methods that allow investigations on a single spin level is therefore a major objective for the realization of modern quantum technologies.

A powerful and widely used method study spins is magnetic resonance. The method has been introduced in 1938 by Isidor Rabi as an extension of the groundbreaking work by Stern and Gerlach and gathers information about spins by detecting their response to electromagnetic radiation at their resonance frequency. Analogous to a classical magnetic moment, spins will rotate in an external magnetic field at a frequency proportional to their magnetic moment. Measurement of this Larmor precession frequency thus allows to identify the spin carrying nuclear species or the orbital structure of an electron. Moreover, this frequency is highly dependent on other closeby spins, can be modified by the binding state of an atom, which is called chemical shift and its lineshape is heavily influenced by motional dynamics. Owing to the simultaneous developments of high frequency equipment and the resulting spectral resolution, magnetic resonance nowadays allows to determine positions of atoms and their bonding to each other with a resolution of $\mathrm{\AA}$ [7]. With its nondestructive nature, it is also a powerful tool to study molecular structure and dynamics in chemistry, biochemistry and medicine. Most recently, for example, the molecular structure of a form of the amyloid-β protein was determined by using nuclear magnetic resonance (NMR), which is believed to play a major role in Alzheimer's disease [8–10].

Under the impression of these results one could argue that magnetic resonance techniques are sufficient to tackle any problem that arises in the field of nanoscale magnetism and structure determination. However, it is often required to look at a single magnetic domain, cell, protein or even spin, which greatly challenges the spatial resolution of classical magnetic resonance techniques. The signal in a regular magnetic resonance spectrometer is typically recorded by the induction in coils around the sample spins. This prevents detection of a magnetic moment with much smaller dimensions than the coil itself, since in this configuration the magnetic flux through the coil is close to zero. A measurable signal thus requires a large number of spins that add up to a sizable magnetic moment, typically around 10^{15} nuclear or 10^{12} electron spins. Consequently, the above results were only achieved by using large quantities of the amyloid-β protein. Magnetic resonance imaging (MRI) uses magnetic gradient fields (around 70 mT/m [11]) which allows to image spin concentrations within a human body with a resolution of (1 mm)^3 in clinical spectrometers. This resolution can still be increased to a voxel size of $(4\ \mu\text{m})^3$, by using gradient coils that have dimensions around a few 100 µm [12, 13].

A further increase in resolution requires to find a different detection method. To achieve resolution on the nanometer scale, the sensor must be brought into close proximity to the sample since the magnetic dipole moment decreases with $1/r^3$ and must be of comparable size to the sample. There are a couple of different techniques that made significant headway in this respect. Magnetic resonance force microscopy (MRFM), for example, has been shown to be able to detect a single electron spin [14]. In this approach, the force that a spin exerts on a magnetic tip is measured by the slight shift of the mechanical resonance frequency of a tuning fork. MRFM, however, is a highly complex technique, that requires ultra-sensitive cantilevers which are able to detect forces on the order of attonewton and operation at mK temperatures. The same goes for electron spin resonance (ESR) techniques in scanning tunneling microscopy, where spins can be detected via spin polarized tips [15].

A fundamentally different and novel way to measure "tiny" signals has emerged over recent years, which can be labeled *quantum sensing* [16]. Its premise seems quite logical: As we want to investigate quantum mechanical properties, why do we not utilize the very same effects for their measurement? In fact, the occurrence of quantum effects seems inevitable when attempting to measure nanoscale entities. The principles of such a sensor rely on the detection of the energy difference between two quantum mechanical states and how this energy difference is influenced by an external physical quantity, like the magnetic field. Such concepts have been developed over many decades already.

Prominent examples are e.g. atomic vapor magnetometers, in which a vapor of mostly alkali-atoms is held in a cell at room temperature for sensing magnetic fields [17]. The atoms are polarized via resonant (laser) pump radiation, and the evolution of their quantum state due to an orthogonal magnetic field is monitored by a second probe beam. These magnetometers reach a sensitivity of 100 aT/Hz$^{1/2}$, which is equivalent to measuring a magnetic field of 100 aT in 1 s with a signal-to-noise ratio (SNR) of 1. However, the smallest size of an atomic vapor magnetometer is a few mm^3 [18], and thus not sufficient to detect nanoscale magnetism. In a somewhat similar fashion, cold neutral atoms can be trapped via magnetic gradient fields and laser cooling. Their level transitions can be utilized for sensing of magnetic fields, with around 20 µm^3 spatial resolution [19]. In principle, an atomic clock also qualifies as a quantum sensor. Here the precise frequency of optically active transitions in for example a trapped ion is monitored to serve as a time standard [20], which finds application for example in the global positioning system (GPS). Yet, these transitions are specifically chosen to not interact with the environment, which of course does not allow to measure external quantities.

Another type of quantum effect is used for sensing in superconducting quantum interference devices (SQUIDs), which measure magnetic flux through a superconducting loop interrupted by two weak links. For this the Josephson effect plays a crucial role. In SQUIDs magnetic field sensitivities as high as 10 aT/Hz$^{1/2}$ can be reached [21], which constitutes the most sensitive magnetometer up to date. However, their implementation as sensors for the nanoscale is challenging as it involves the miniaturization of the superconducting circuit. Nonetheless, development of "nanoSQUIDs" in a scanning geometry has been successful [22] and even demonstrated to have single electron spin sensitivity with a loop-diameter as small as 46 nm [23]. This system was recently employed as a thermometer on the nanoscale [24].

This thesis will be concerned with yet another class of quantum sensors for magnetic fields, which are single spins in solids. Among the many realizations of such a system, which include phosphorus in silicon [25], semiconductor quantum dots [26, 27] or even single organic molecules [28], the nitrogen vacancy defect center in diamond (NV–center) [29] has emerged as a versatile quantum sensor, which received increasing attention over recent years.

Consisting of a carbon vacancy adjacent to a nitrogen atom that is substituted for a carbon atom in the diamond lattice, the NV–center has an electronic spin state that can be read out and polarized using confocal fluorescence microscopy. Combined with active manipulation of the spin using resonant microwave fields, electron spin resonance (ESR) on this electron spin with a spatial dimension of only two diamond lattice sites can be performed [30]. This so called optically detected magnetic resonance (ODMR) grants the precise measurement of the spin sublevel energies in a single NV–center. The sensing capabilities stem from the interaction of the spin with its environment and Zeeman effect, Stark effect and temperature dependent shifts have been used to demonstrate magnetometry [31, 32], electrometry [33], pressure sensing [34] and thermometry [35], respectively. The outstanding characteristics of the NV–center are the ability to operate it at room temperature, its essentially atomic size and its long quantum coherence [36].

The quantum properties of this sensor manifest, for example, in the fact, that magnetic field sensitivity is limited by its quantum coherence [37]. Hand in hand with developments in diamond growth and implantation techniques, the predicted and experimentally demonstrated magnetic sensitivity of NV–centers has reached $10\ \mathrm{nT/Hz^{1/2}}$ [36]. While this sensitivity might not be as high as for other quantum sensing techniques, most notably the NV–center can be brought within a few nm to a sample spin system by shallow implantation just below the diamond surface [38] without losing its stability. This has lead to the detection of nanoscale ensembles of nuclear spins [39, 40] and electron spins [1, 41] and later even a single electron spin [2, 42], which will also be the main focus of this thesis. What establishes the NV–center as a true quantum sensor is also the upcoming of sensing schemes that fully harness quantum properties, like entanglement and quantum state storage. For eample, quantum state transfer with swap gates between the NV–center electron and nuclear spin have recently shown an increase in spectral resolution [43] and enabled the detection of nuclear magnetic resonance from a single protein [44].

Moreover, the NV–center can be incorporated into a scanning probe architecture enabling spatial magnetic imaging with atomic resolution. This has sparked many efforts to develop scanning diamond tips containing NV–centers for a combination with atomic force microscopy (AFM), either by attaching nanodiamonds to existing tips [32, 45] or by etching them from bulk diamonds [46, 47], an approach gaining more and more traction in recent years. Together with the above discussed sensitivity, this has already enabled the observation of many effects in nanoscale magnetism too numerous to mention here. Excellent reviews on this topic are given in references [16, 48, 49].

This thesis aims to advance the field of nanoscale investigations of magnetism from electron spins for which the NV–center quantum sensing capabilities will be used. In particular, the atomic sized magnetic field sensor will be employed to perform electron spin resonance on nanoscale volumes and few electron spins. Chapter 2 reviews basic physics of NV–centers in diamond together with established methods relevant for magnetic field sensing and the properties as a quantum sensor. In chapter 3 the measurement apparatus is introduced and it is demonstrated how its scanning probe capabilities can be used for nanoscale magnetometry. The application of the NV–center as a quantum sensor will be demonstrated with measurements of temperature dependent relaxation in ferritin nanomagnets presented in chapter 4. Subsequently, measurement schemes for performing nanoscale electron spin resonance on samples outside the diamond will be introduced and applied to detect electron spins on the diamond surface. Chapter 5 applies these principles to sense electron spins attached to specific sites on polyproline peptides, after which the ability to sense less than 10 electron spins and novel schemes to access their dipolar coupling are demonstrated. In chapter 6 an outlook on future developments and experiments under the light of the progress presented in this thesis is given.

2. The NV–Center in Diamond as a Spin–Sensitive Magnetometer

As all of this work will revolve around the nitrogen vacancy center in diamond as a magnetic field sensor, this chapter is dedicated to the development of a solid framework for a detailed understanding. For this, the diamond material and structure as well as electronic and optical properties of the NV–center are described. Within the second section it is explained how these properties make the NV–center an extremely versatile magnetic field sensor. Various measurement protocols that can be utilized for magnetic field sensing in different bandwidths are presented. The last section focuses on a quantum mechanical description of the defect, where special emphasis is put on the spin physics and magnetic interactions. This theoretical basis will be used throughout the thesis to rationalize measurement results.

2.1. The NV–Center in Diamond

Diamond is a metastable phase of carbon, however only at rather extreme conditions a transformation to graphite happens at observable rates [50]. Initially, diamond is believed to have been discovered in India more than 6000 years ago [51] and has ever since received widespread attention, mostly due to its outstanding Young's modulus [52] and chemical inertness [53] or aesthetics, which can nowadays even ramp its value to 5.97 million USD/g (Pink Star diamond [54]) in the form of a cut gemstone. Here we discuss diamond for its ability to host stable atomic defects, whose spins are optically accessible and therefore provide us with means to investigate phenomena on the nanoscale.

2.1.1. Structural Properties

Diamond consists solely of carbon atoms in a face centered cubic Bravais lattice that has a two-atom unit cell, with one atom shifted by $1/4$ on the (111)-axis relative to the other. Diamond belongs to the space group $Fd\bar{3}m$ and has a lattice constant of

$a = 3.57$ Å. To form a crystal the four electrons in the s- and p- orbitals of the second shell carbon orbitals form sp^3 hybrid orbitals, which covalently overlap to give the distinct tetrahedral structure. These extremely stable bonds make it the hardest material on Earth, with a Young's modulus of 1050 GPa and give it a large thermal conductivity of $22\ \mathrm{Wcm}^{-1}\mathrm{K}^{-1}$ [55]. Furthermore, diamond is bio-compatible [56], i.e. it mostly does not perturb biological system, due to its inertness. In contrast to most of the other elements in group 14 (IVa) which are semiconductors, diamond is often regarded as an insulator, due to its large bandgap of $5.48\ \mathrm{eV}$, which makes it also transparent up to ultraviolet (UV) wavelengths. Additionally diamond has a rather high refractive index of $n = 2.39$.

These properties make it a highly desirable material for all sorts of applications. One of these applications where active research is ongoing, is to use diamond as a semiconductor, since its thermal properties would for example greatly benefit power electronics [57]. Here one of the main challenges is the incorporation of defects into the diamond lattice, hindered by the stable bonds between carbon atoms, to tune and control the doping level required for transistors.

Diamonds can be classified according to the amount and type of impurities they contain. There are in total four commonly used classes according to the nitrogen and boron content in the crystal [58]:

- **Type Ia**: very high nitrogen content of < 3000 ppm, in the form of aggregated nitrogen clusters. Pale yellow color.
- **Type Ib**: high nitrogen content of < 500 ppm, in the form of paramagnetic single nitrogen impurities. Yellow to brown color.
- **Type IIa**: very low nitrogen content of < 1 ppm. Colorless.
- **Type IIb**: very low nitrogen content of < 1 ppm, significant content of boron ($10^{22}\ \mathrm{m}^{-3} - 10^{23}\ \mathrm{m}^{-3}$), effectively acting as a p-dopant resulting in a low electrical resistivity. Light blue or grey color.

Type I diamonds contain a high amount of nitrogen impurities, which are the most common natural diamonds to be found, while Type II diamonds are much cleaner from an impurity point of view. It needs to be pointed out that a diamond can contain multiple areas of different categories and additionally these categories can be refined into sub-categories (especially Type Ia).

Additional to mining diamond from the earth's crust, nowadays diamonds are also readily produced artificially in essentially two distinct approaches. For the first approach, high pressure and high temperature (HPHT) is applied to graphite or some other form of carbon for a certain amount of time which eventually forms diamond. This is in principle the same way diamonds are produced within the lithospheric mantle of earth over long periods of time. With this approach, large quantities of material can be produced, however often of poor quality and mostly of Type I containing many impurities [59]. Clean diamonds of Type II are artificially created using chemical vapor deposition (CVD). Here, a seed crystal of high quality is subjected to high temperature gas of some hydrocarbonate, which can bond to the carbon surface dangling bonds [60]. This way, high quality diamond (strongly depending on the substrate quality) with extremely low defect concentration can be grown layer by layer. In this thesis only Type IIa host material was be used.

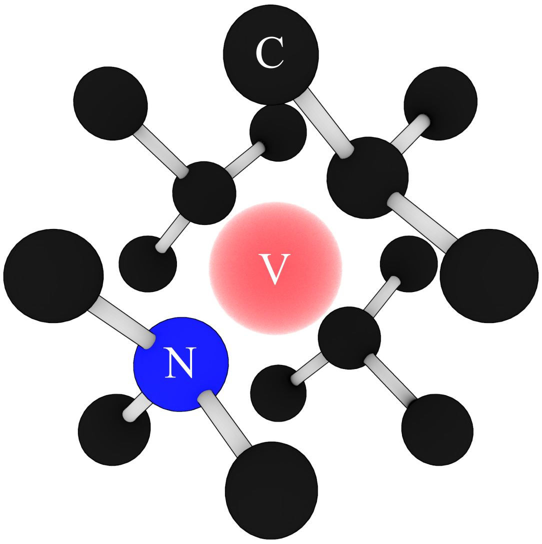

Figure 2.1.: Depiction of the NV–center in diamond. A nitrogen atom (blue) is substituted for a carbon atom (black). Additionally one near-neighbor carbon atom is removed to create a vacancy, where actually the highest concentration of electron density resides (red).

Despite the difficulty to introduce other atoms than carbon into diamond, there is a vast variety of known defects, studied extensively over many decades [61]. The main doping elements of diamond, as suggested from the classifications given above, are boron and nitrogen, relatively easy to be introduced into diamond due to similar size to lattice sites in diamond. Acting as electron donor or acceptor the impurity atoms pin electron concentrations leading to local paramagnetism and sometimes strong transitions in the visible range, responsible for coloring of diamonds. One of the most explored optically active defects in diamond is the NV–center, giving a rather unique combination of spin and optical properties, as will be discussed in detail within the next chapters. The NV–center consists of a substitution of carbon by a nitrogen atom and an adjacent carbon vacancy (see fig. 2.1). The symmetry point group of this two atom defect in a diamond lattice is the one of a regular triangle, C_{3v}. This symmetry is manifested in four different spatial orientations, due a four-fold symmetry operation in the diamond space group (corresponding to the four different spatial orientations of the (111)-direction). The defect was first identified in 1965 [62] and further optical and electron spin resonance experiments eludicated quite early, that optical photons can have an effect on its spin state, attributed to an intersystem crossing [63, 64].

The NV–center defect can be found in natural diamonds, since nitrogen or vacancies can migrate through the diamond over time until they eventually combine, but can also be created artificially. Due to the increasing interest in the spin and optical properties of the NV–center, there has been a simultaneously growing interest in artificial creation of NV–centers in an otherwise defect free diamond. Two approaches are used for this purpose nowadays which are (i) implantation of nitrogen ions in high purity diamonds and subsequent annealing and (ii) incorporation of nitrogen during CVD diamond growth and subsequent irradiation with ions or electrons.

The first approach allows for control of the depth of NV–centers formed via the chosen kinetic energy of implanted ions. A subsequent annealing step at temperatures over 650 °C makes the vacancies, which were formed during crystal penetration, mobile and thus increases NV–center yield [65, 66]. Disadvantages of this technique are that the ion straggling creates a large amount of crystal faults, which can have an impact on NV spin properties. Furthermore, the depth and position of the NV–centers can have a large spread.

The incorporation of nitrogen during growth has the disadvantage that there is no control where the nitrogen atoms will be located. However, it is possible to precisely control the depth due to the atomically stepwise growth, so called δ-doping [38]. Again, vacancies have to be created via irradiation with high energy particles like electrons and a subsequent annealing step is needed to mobilize the vacancies. Overall, this approach creates much less unwanted crystal defects and results in overall better NV–center spin properties.

Nonetheless, both approaches have the fascinating ability to create vacancies within a few nanometers below the diamond surface in a deterministic way. This is key for many applications that require interaction with diamond external systems.

2.1.2. Electronic Structure

To describe the electronic structure of a molecule or a localized defect within a solid state system, we need to consider the full electronic Hamiltonian. According to the Born-Oppenheimer approximation [67], we can however separate nuclear motion from electronic motion, i.e. all nuclei are fixed. Hence we can write the NV–center Hamiltonian as:

$$
\begin{aligned}
H_{\text{NV}}^{\text{full}} = & \sum_i \left(H_{\text{kinetic}}^i + H_{\text{Coulomb-crystal}}^i + H_{\text{spin-orbit}}^i + H_{\text{hyperfine}}^i \right) \\
& + \sum_{i,j} H_{\text{Coulomb-ee}}^{i,j} + H_{\text{spin-spin}}^{i,j} .
\end{aligned}
\tag{2.1}
$$

Here, H_{kinetic}^i describes the kinetic energy of the i-th electron, $H_{\text{Coulomb-crystal}}^i$ is the Coulomb potential imposed by the crystal nuclei and electrons on the NV electrons, $H_{\text{spin-orbit}}^i$ is the electronic spin orbit coupling, $H_{\text{hyperfine}}^i$ is the hyperfine interaction of the NV electrons with the crystal nuclei, and $H_{\text{Coulomb-ee}}^{i,j}$, $H_{\text{spin-spin}}^{i,j}$ are the Coulomb potential and spin-spin potential between the NV electrons [68].

This Hamiltonian cannot be solved exactly. However, one approach to tackle this problem is to use atomic orbitals (AO), which are a solution of the one-electron problem (first two terms in eq. 2.1) and construct molecular orbitals (MO) as a linear combination of them (LCAO), which are then filled up with electrons. Following this path one can include many-particle effects as perturbations. The AOs in the case of the NV–center are sp^3-hybridized orbitals from three carbon atoms and one nitrogen atom.

Since this approach imposes a rather large approximation, group theory can further simplify the problem. For example, one needs to find LCAOs that transform according to irreducible representations of C$_{3v}$. This, for example, immediately predicts the existence of two single and one double degenerate energy levels[1] [69]. An example of MOs constructed this way can be seen in figure 2.2a. *Ab initio* calculations [70, 71] and experiments can then finally reveal the energy-order of the states, where in the case of the NV–center the first a_1-level lies within the valence band of diamond, while the others lie within the bandgap.

Up to date, three different electronic charge states of the NV-defect have been suggested and experimentally verified. In total, the three electrons in dangling sp^3 vacancy orbitals and the two additional free electrons in the nitrogen impurity orbitals give rise to five

---

[1] Since this requires some deeper knowledge of group theory not in the scope of this thesis, the interested reader is reffered to the excellent literature on the topic.

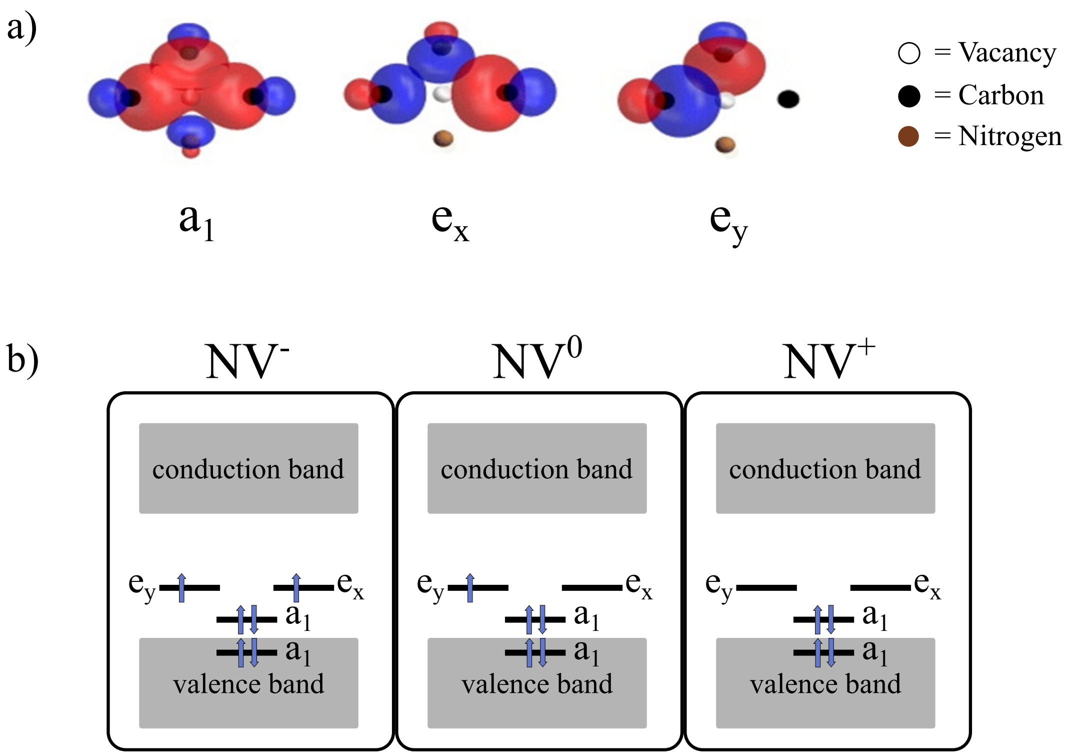

Figure 2.2.: Molecular orbitals of the NV–center defect. a) The molecular orbitals that result from a LCAO of atomic orbitals from carbon and nitrogen. The orbitals are named corresponding to the irreducible representation of the C_{3v} group they transform under symmerty operations. Red are positive, blue negative parts of the wavefunction. Figure adapted from [72]. b) Energy level diagram of the NV–center electronic ground state in its three different charge states within the bandgap of diamond.

electrons that fill up the molecular NV orbitals, termed neutral NV^0. This configuration has a total electronic spin quantum number of $S = 1/2$, leaving a single electron in the highest $\mathrm{e_x}, \mathrm{e_y}$ orbital (figure 2.2b). It is naturally possible for the defect to trap or release electrons from or to the energy bands in diamond, depending on the position of the Fermi-level, as well as from or to other closeby defects. Thus, a positively charged version of the defect, NV^+, has been predicted and very recently also realized deterministically in experiments [73, 74]. A key to this charge state control is the implementation of gates on the diamond surface for Fermi-level control, which can be realized by hydrogen termination. The NV^+ defect has a total spin quantum number of $S = 0$ (figure 2.2b), is not optically active and could so far only be detected with a passive sensing scheme of its nuclear spin state [74]. The negative version of the NV–center, NV^-, manifests more effortless and is also more stable. It is readily found in natural and implanted diamonds, stabilized by other close-by defects (supposedly a nitrogen impurity [75]) or environmental Fermi-level bending. Its six electrons give rise to an electronic $S = 1$ system, which can be accessed optically. This optical accessibility forms the foundation for magnetic field sensing as will be discussed in detail in section 2.2. It has been shown that not only surface modification can induce charge state switches, but also optical excitation with selective wavelengths [76].

While more paramagnetic defects with optically accessible spin states have been discovered in diamond [77, 78] and in other promising host materials [79], up to date, the negatively charged nitrogen vacancy center remains the most prominent and well-studied one. Most importantly, all NV–center magnetometry schemes presented in this thesis will be based on the negatively charged NV$^-$ state and hence we will exclusively discuss this charge state and omit the $-$ sign from now on.

2.1.3. Optical Properties

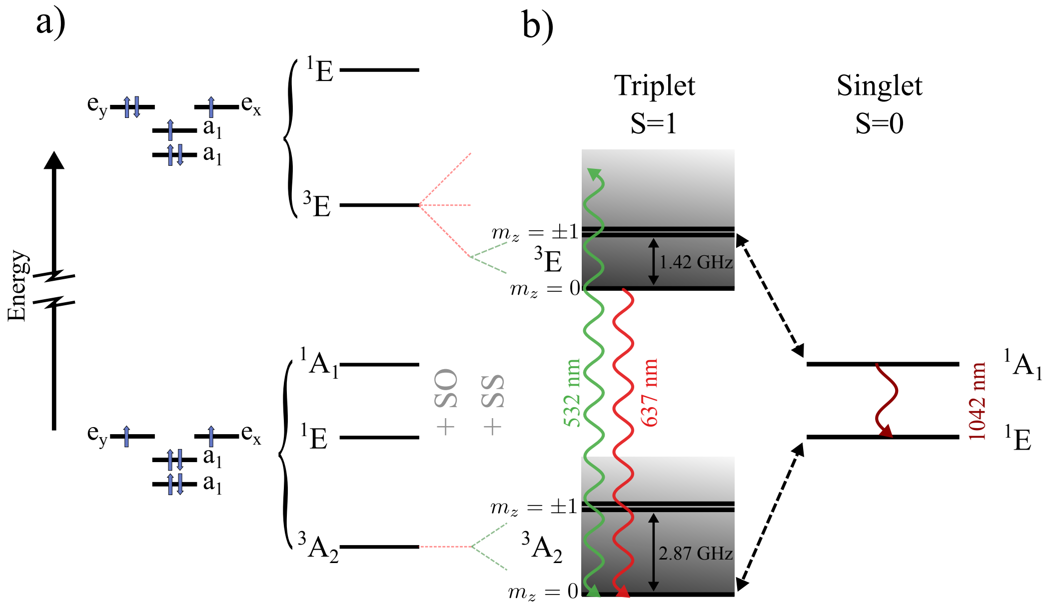

Figure 2.3.: a) Ground and first excited electronic states of the NV–center. b) ground and first excited state with inclusion of fine structure. Dashed arrows are allowed transitions that occur with a rather high probability, while sinusoidal waves depict optical photons. For the singlet state decay near infrared photons have been observed [80].

To describe the optical transitions that can occur in the negative NV–center, we need to take a more careful look at the orbital structure (figure 2.3). When constructing ground state and first excited state configurations from the single electron MOs shown in figure 2.2, one finds that the respective electron configurations are $\mathrm{a}_1^2\mathrm{a}_1^2\mathrm{e}_x^1\mathrm{e}_y^1$, $\mathrm{a}_1^2\mathrm{a}_1^2\mathrm{e}_x^2$, $\mathrm{a}_1^2\mathrm{a}_1^2\mathrm{e}_y^2$ for ground state and $\mathrm{a}_1^2\mathrm{a}_1^1\mathrm{e}_x^2\mathrm{e}_y^1$, $\mathrm{a}_1^2\mathrm{a}_1^1\mathrm{e}_x^1\mathrm{e}_y^2$ for excited states [72]. Construction of orbitals from those configurations is accomplished by linear combination of products of the above MOs that must transform according to irreducible representations of the C_{3v} group, while the spin is subsequently included as a direct product [72]. The resulting orbital levels are depicted in figure 2.3a. Hereby the orbitals are noted by the irreducible representation of the orbital symmetry (A_1, A_2, E) with spin degeneracy in the exponent. All three orbitals in the ground state transform according to a different irreducible representations of the C_{3v} group, which means that there are two non degenerate (A_1, A_2) and a double degenerate (E) level[2]. There are two spin singlets and one triplet state present, with the spin triplet being the lowest in energy and thus the ground state (GS) of the NV–center [81, 82]. The exact positions of the two remaining spin singlet levels is still under debate [83], however they most certainly lie above the ground state and their energy difference has been experimentally verified [84]. In the first excited state (ES) level two orbitals with E-symmetry are present, one a spin singlet (which will not play a role for the optical transitions) and a spin triplet.

Upon including fine structure in the Hamiltonian, which means adding spin-orbit interaction (SO) and spin-spin interaction (SS) due to the interaction of the two uncoupled electrons, the symmetry dictated level degeneracy is partly lifted (figure 2.3b).

The ground state levels are not influenced by SO interaction, since either the state has no orbital ($^3\mathrm{A}_2$), or no spin momentum ($^1\mathrm{E}$, $^1\mathrm{A}_1$). However, the $m_S = \pm 1$ levels are split by 2.87 GHz from the $m_S = 0$ level due to SS [63].

The excited ($^3\mathrm{E}$) state structure is more complex. Including SO splits the $^3\mathrm{E}$ doublet into three orbital doublets, which are then further shifted with respect to each other via SS and are strongly influenced by strain [85, 86] to reveal six excited state energy levels. At room temperature however, this orbital structure is completely averaged out (and not shown in figure 2.3b) due to thermal phonons. In turn, the excited state can simply be described by an effective orbital singlet, where the levels appear at their averaged value, split similar to the ground state via SS interaction by 1.42 GHz [87]. Thus we finally arrive at the effective level structure (still excluding hyperfine and magnetic field interactions) depicted in figure 2.3b, where the higher levels which do not play a role in optical transitions have been omitted.

---

[2] This follows directly from group theory, since the dimensions of the irreducible representations give the degeneracy of energy levels. Note that this degeneracy is *not* an orbital degeneracy. The reader is again referred to respective literature on group theory.

As indicated in the graph, transitions between the $^3\mathrm{A}_2$ and the $^3\mathrm{E}$ levels are possible due to spin-conserving dipole moment interactions that lead to the characteristic optical fluorescence spectrum, shown in figure 2.4a at low temperatures. Optical excitation promotes an electron from the a_1 to the e_x or e_y level whose dipole lies perpendicular to the NV-axis (figure 2.2). Therefore it is most efficient to excite the NV–center with a laser beam propagating parallel to its axis. The emission spectrum reveals a zero phonon line (ZPL) at 637 nm and a broad phonon sideband. According to the Franck-Condon principle, a phonon transition is more likely to happen alongside the optical transition and thus only about 4% of the photons are found in the ZPL and the rest stems from relaxation into the phonon sideband. In fact, this is the reason why it is far more efficient to excite the NV–center electronic state with a lower wavelength, the most commonly used being 532 nm, instead of a resonant excitation at the ZPL. Furthermore, due to excitation into the phonon sideband the usage of the simplified, averaged excited state level scheme is still valid, even at low temperatures. The complex and strain sensitive excited state level structure can however be probed via resonant excitation at low temperatures.

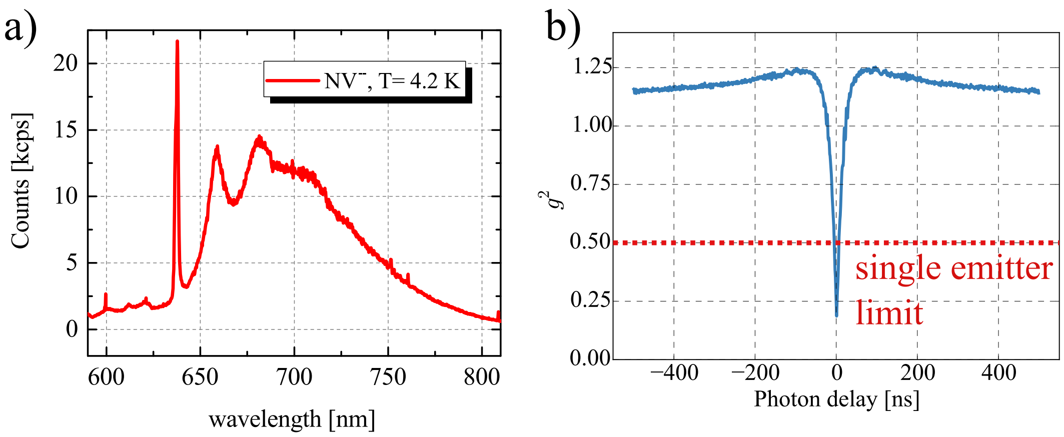

Figure 2.4.: Optical emission properties of NV–centers under 532 nm illumination. All measurements performed at $T = 4.2$ K in the cryogenic system described in chapter 3. a) Photoemission from an ensemble of NV–centers. b) Autocorrelation measurement of emission from a single NV–center. The shown curve is recorded by two single avalanche photon detectors in a Hanbury Brown and Twiss geometry (see also chapter 3).

The NV–center proves to be of extraordinary stability under optical illumination, unlike e.g. quantum dots or other defects in solids. One of the reasons is the large bandgap of diamond and the resulting isolation of energy levels, that make a non-reversible transition to other energetically stable configurations highly unlikely. As mentioned earlier, transitions to NV^0 are possible [83] and frequently observed, however excitation with green light has the ability to rapidly pump the NV–center back into the negatively charged state [76], which constitutes another reason to use green light for excitation. The remarkable stability of the NV defect enables one to identify single stable defects using the optical signal. Upon recording the photon-photon autocorrelation, i.e. the probability of two photons being emitted at the same time, it is readily possible to characterize single NV–centers as single photon sources (2.4b) with a dip at zero photon delay. To classify as a single NV–center (or a single photon emitter) the autocorrelation function needs to drop below 0.5, which is observed frequently, given an adequately low implantation dosage.

Spin State Dependent Fluorescence and Optical Polarization

The most important feature of the optical transitions is the depicted spin dependent intersystem crossing from the excited state spin $^3\mathrm{E}$ triplet to the $^1\mathrm{A}_1$ singlet level, which leads to a couple of highly interesting phenomena under optical illumination, namely the ability to read out the spin state optically and to polarize it with a high fidelity. The reason for this ISC is the spin orbit coupling, which includes cross-relaxation terms between singlet and triplet states. As can be seen in figure 2.3b, this transition is actually spin state selective, i.e. it has a much higher probability (comparable to the optical transition) for the $m_S = \pm 1$ manifold (lifetime $\tau \sim 7.8$ ns) to occur, than for the $m_S = 0$ manifold ($\tau \sim 12$ ns) [88]. Subsequently the $^1\mathrm{A}_1$ level actually has an extremely short lifetime below $\tau < 1$ ns and the electron quickly decays to the lower lying $^1\mathrm{E}$ level, which is metastable ($\tau \sim 250$ ns). From this shelving state, the NV decays predominantly to the $m_S = 0$ substate of the $^3\mathrm{A}_2$ ground state with extremely high probability [89].

The ISC decay channel leads, in contrast to the spin conserving optical decay channel, to a spin state of $m_S = 0$ with a very high fidelity. The direct consequence of this is a spin state polarization into the non-magnetic $m_S = 0$ state after optical excitation with non resonant light, *regardless* of the spin state prior to the excitation. If the spin is in the $m_S = \pm 1$ manifold of the ground state, the excitation and subsequent phononic relaxation will lead to the $m_S = \pm 1$ manifold of the excited state, where it eventually (after repeated optical pumping) decays via the singlet states to the $m_S = 0$ ground state without radiation of a photon[3]. If the NV spin is in $m_S = 0$ prior to excitation, it will always decay under the emission of a red photon to the $m_S = 0$ ground state. In fact, spin polarization under 532 nm illumination has been measured to

---

[3] Taking into account, that the detectors used in this work will not be sensitive for photons with wavelengths as high as 1042 nm.

surpass 90% (for excitation of single NV–centers) [90]. It needs to be pointed out that above $T = D/k_B = 2.87$ GHz/$k_B \sim 0.14$ K the Boltzmann distribution mitigates equal population in all spin triplet states. Optical pumping with wavelengths higher than the ZPL however leads to a spin polarization corresponding to an effective spin temperature of ~ 100 mK, even if the surrounding crystal is at room temperature or higher.

The second important feature is that the emission of the NV–center can now be correlated with its spin state before the excitation. Since the decay via singlet levels does not contribute to red emission, fluorescence is significantly decreased if the NV–center resides in $m_S \pm 1$ spin states in comparison to the $m_S = 0$ spin state. Notably, this occurs because the spin state is shelved for 250 ns in the metastable ^1E state, where it does not contribute to emission. This spin dependent photon contrast regularly surpasses 30% for single NV–centers, which is in principle determined by the transition ratios to and from the singlet states.

The combination of close-to-perfect spin polarization and the ability to determine the spin S_z-component by pure optical means in single photostable defect centers constitutes the reason why there has been an ever increasing interest in NV–centers. We can therefore fully polarize and read out the NV–center spin state, which will be explained in more detail in chapter 2.2. Harnessing these effects is called optically detected magnetic resonance (ODMR). An exceptional feature of the NV–center is however, that it allows one to perform electron spin resonance with a single spin [29]. This makes it a prime candidate for quantum sensing and quantum computation and likewise sparked large interest following the discovery of its properties.

2.2. Optically Detected Magnetic Resonance

Optically detected magnetic resonance (ODMR) combines the techniques of photoluminescence and electron spin resonance, which has been proposed and demonstrated in 1952 by Brossel and Bittner [91] and subsequently used for excited state spectroscopy and recombination in semiconductors [92, 93]. To this end, instead of detecting the microwave absorption as it is done in conventional ESR methods, one detects changes in fluorescence upon manipulating spin states via resonant microwave radiation.

A detailed description is given here, how one can exploit the spin dependent luminescence and optical spin polarization of the NV–center in diamond, to perform ODMR experiments on a single spin. In this section the concepts and measurement protocols are described, while the experimental apparatus is described in chapter 3.

2.2.1. ODMR Spectroscopy

Continuous Wave ODMR Spectroscopy

A first intuitive approach for a spectroscopic measurement is to continuously apply both microwave and laser radiation, that promotes the NV into the phonon broadened excited state. Simultaneously the fluorescence from the ES into the GS phonon sideband (> 650 nm) is monitored depending on the applied microwave frequency. This so called continuous wave (cw) ODMR yields information about the fine structure and Zeeman interactions of the NV–center under investigation. As discussed in detail in section 2.1.3, upon application of laser radiation, the NV–center will be quickly polarized to the $m_S = 0$ substate. This results in a constant high fluorescence count, since almost every excitation photon leads to a fluorescence photon. Sweeping the frequency the microwave will eventually be in resonance with one of the $m_S = 0 \leftrightarrow m_S = \pm 1$ transitions and flip the NV to the $m_S = \pm 1$ states. This results in a decrease of fluorescence due to a non-radiative decay via the singlet states (see figure 2.3).

A typical measurement on a single NV–center in high purity diamond is shown in figure 2.5. At zero magnetic field, there is a single dip corresponding to the double degenerate ± 1 level transitions. This directly gives the value of the zero field splitting parameter D (2.88 GHz at $T = 4$ Kelvin). Furthermore, strain would lift this degeneracy (ZFS parameter E), if present. The degeneracy is lifted in any case through the application of a static external field via Zeeman interaction and splits the $+1$ and -1 transitions in a symmetrical fashion if the external field direction coincides with the NV–center principal axis. For any misalignment of the external field, the Zeeman shift is asymmetric, which has a number of consequences due to the mixing terms in the Hamiltonian like added decoherence or loss of fluorescence.

The sensitivity of ODMR spectroscopy is naturally limited by inhomogeneous effects in the environment of the NV–center, which are expressed through the characteristic timescale T_2^*. This also determines the lineshape of shown spectra, governed by microwave absorption of the spin, which has the form of a Gaussian with width $\sim 1/T_2^*$. With the described scheme however, usually the intrinsic inhomogeneous broadening is overshadowed by broadening through power and frequency fluctuations of the laser and microwave radiation. This prevents for example the resolution of hyperfine interactions in graph 2.5. To overcome these limitations either power stabilized equipment can be used or the power can be reduced with an accompanying loss of contrast. The other approach is to switch to pulsed readout techniques, which also form the basis for coherent control of the NV–center spin.

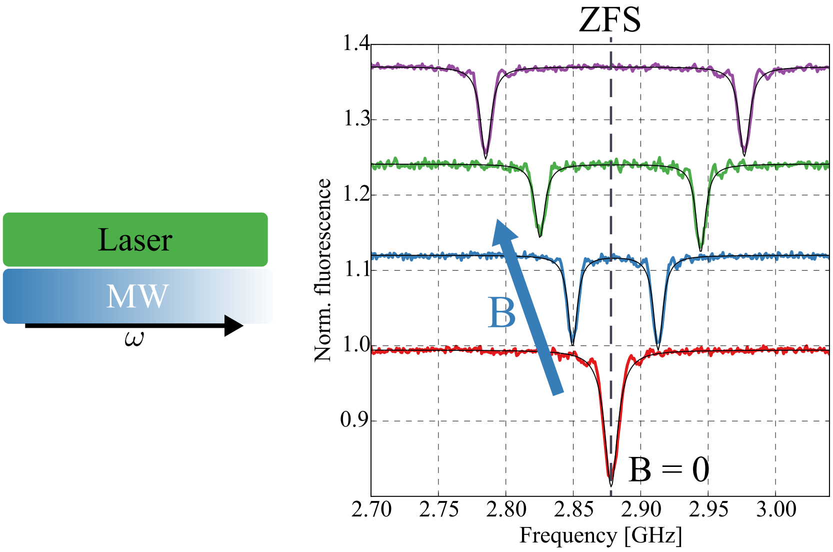

Figure 2.5.: ODMR spectroscopy on single NV–centers. Left: Measurement scheme for cw ODMR. Right: cw-ODMR with increasing magnetic field applied roughly along the NV axis (red curve: zero magnetic field). Slight asymmetry is caused by magnetic field misalignment.

Pulsed ODMR Spectroscopy

The basic idea of pulsed ODMR schemes is to polarize the spin state via laser radiation of appropriate length and *subsequently* manipulate it with microwave radiation in the dark. Finally the spin state is read out by another laser pulse and simultaneously polarized again. This basic pulsed ODMR scheme is depicted in figure 2.6 and has two major advantages. The first is that since the spins state is manipulated in absence of laser radiation the measurement will become more robust against laser power and frequency instabilities. Secondly, we are now able to *coherently* manipulate the NV–center spins state between laser pulses. In principle, coherent manipulation is simply achieved by microwave of a certain length in time, corresponding to a certain phase between quantum states (see next chapter 2.2.2). However, in the previously described cw ODMR no coherent manipulation was possible, since the constant probabilistic absorption of an optical photon and the connected polarization mechanism continuously destroyed the created phase difference. Using this sequential scheme, the spin state remains unchanged until it is either deliberately manipulated or affected by magnetic signals in the environment, which is the key to quantum sensing.

As is clear from the duration of the polarization mechanism ($=$ lifetime of singlet states) and the measured fluorescence response in figure 2.7, one needs to detect the fluorescence photons in the first ~ 400 ns after onset of laser radiation to determine

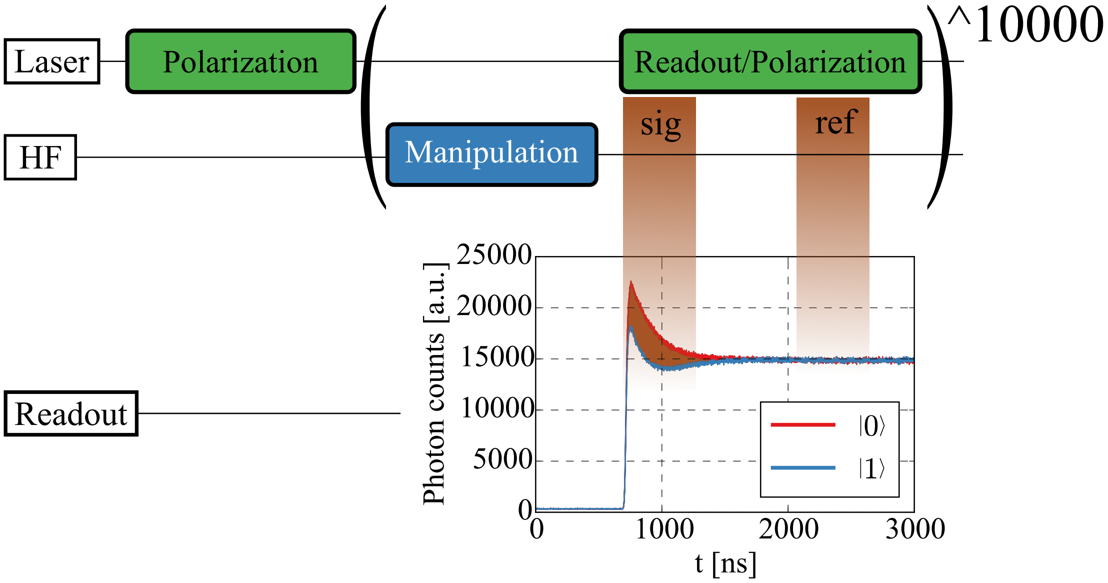

Figure 2.6.: Pulsed measurement scheme for NV manipulation and spin state determination. HF is a series of microwave and/or radiofrequency pulses that coherently manipulate the NV spin state. The readout is achieved by a single photon counting module and appropriately fast electronics.

the spin state with high fidelity. If the NV is in the $m_S = 0$ state before excitation, there will be an initial high fluorescence response, which decays to a steady state value. Although the NV is almost fully polarized into $m_S = 0$ the steady state fluorescence will be lower, since there is a constant shelving in the ^3E singlet state due to the small but non negligible ISC from $m_S = 0$ to the singlets. If the NV is in the $m_S = \pm 1$ states however, the fluorescence response will rapidly decrease due to the high ISC probability to the non fluorescing singlet states and eventually recover towards the same steady state value due to polarization into $m_S = 0$. The timescale of this dynamics is governed by the lifetime of the ^3E singlet level ($\tau = 250$ ns). To determine the spin state the integrated photon counts in the first ~ 400 ns, which is the signal window, are divided by the integrated steady state fluorescence in a second ~ 400 ns window after ~ 1.5 μs, which is termed reference window (figure 2.6). This procedure leads to a spin state contrast between $m_S = 0$ and $m_S = \pm 1$ of 30 $\%$. Normalization with the reference window additionally decreases noise from unsteady fluorescence.

Typical countrates for fluorescence photons from single NV–centers can reach up to 10^6 photons/s in optimized setup at room temperature (see chapter 3.1). Even for this state-of-the-art fluorescence collection, there are on average only 0.3 photons arriving in the signal window for a single readout run. With typical spin contrast values at 30 $\%$,

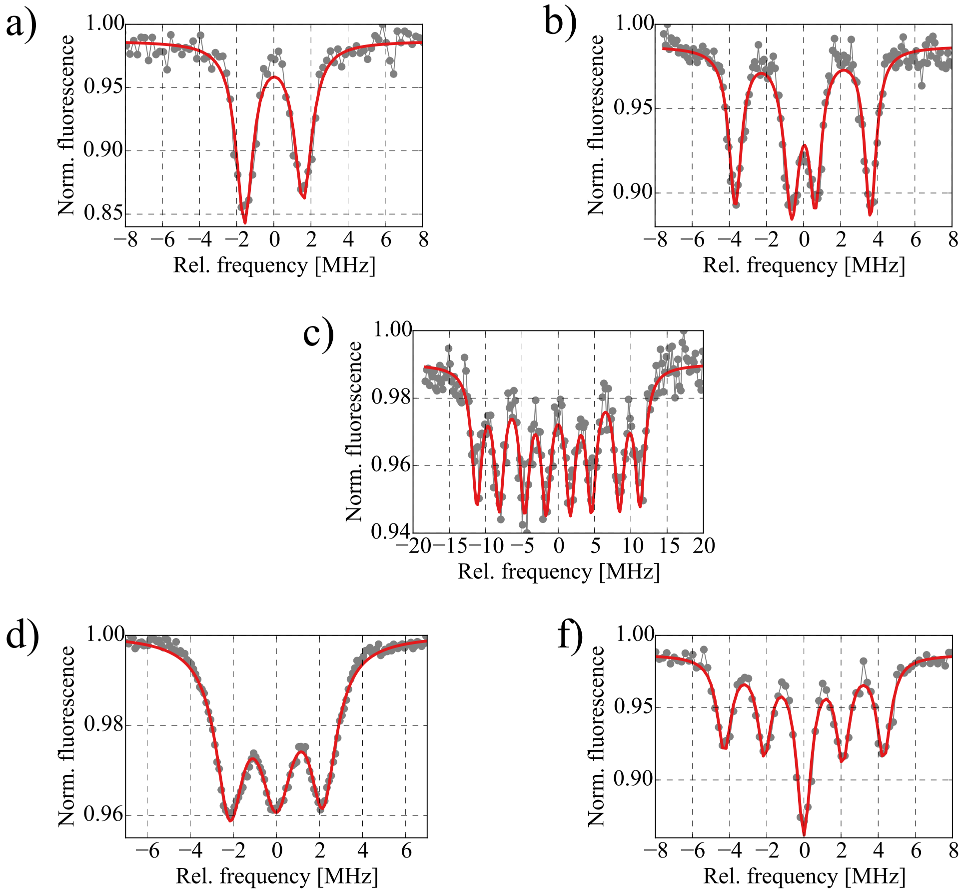

Figure 2.7.: Pulsed ODMR spectroscopy on single NV–centers with different hyperfine couplings. a) ^{15}N b) ^{15}N and $2{\cdot}^{13}$C c) ^{15}N and $2{\cdot}^{13}$C d) ^{14}N f) ^{14}N and ^{13}C.

only 0.1 photons per run contribute to the spin state signal. Therefore, to achieve an acceptable signal to noise ratio (SNR) the experiment needs to be repeated several thousand times. These low photon numbers also illustrate that NV spin state readout is dominated by photon shot noise as the main noise source.

By using a pulsed ODMR scheme power broadening effects are overcome and it is now possible to resolve hyperfine interactions of single NV–centers. Here the manipulation part is a single microwave pulse of appropriate length that fully flips the spins state to $m_S = -1$, also referred to as a π-pulse (see next subsection). When sweeping the frequency of the microwave, the spin state will only be changed when the attempt frequency excites the transition. In this case, the ESR linewidth is given by the Fourier transform of the product between the approximately rectangular profile of the π-pulse and the Gaussian profile due to inhomogeneous broadening of width $1/T_2^*$ [94]. To resolve features on the MHz scale, T_2^* and the π-pulse length need to be longer than a 1 µs, which can be achieved by lowering the microwave power and therefore reducing the Rabi frequency (see 2.2.2).

In figure 2.7 measurements on various NV–centers are shown, which reveal different hyperfine couplings upon the application of the pulsed ODMR scheme. Naturally, hyperfine coupling to the nitrogen nucleus of the NV–center is always observed. Since two stable isotopes of nitrogen exist, namely ^{14}N with nuclear spin $I_{14}^N = 1$ and ^{15}N with nuclear spin $I_{15}^N = 1/2$, we likewise observe three and twofold splittings respectively (figures 2.7a+d). Since the nitrogen atoms are always fixed in spatial position, the splitting of ESR lines is 2.2 MHz for ^{14}N and 3.05 MHz for ^{15}N respectively. These different splittings are used to distinguish between implanted and natural NV–centers, since the natural abundance of ^{15}N is only about 0.4%. Although the much more abundant ^{12}C atoms are spin-less, there also exists a stable isotope of carbon, ^{13}C with nuclear spin $I_{13}^C = 1/2$ of 1.1% abundance, which can also couple to the NV–center electron spin via hyperfine interaction. Here, the strength is dependent on the distance between the carbon nuclear spin and the position of the NV–center and can be as high as 126 MHz for a nearest neighbor ^{13}C [95]. In figure 2.7b+c+e, different interactions with one or two nuclear carbon spins are shown. Since the secular approximation for the hyperfine interaction is valid (i.e., the electron Zeeman and electron ZFS is orders of magnitude larger than nuclear energy terms), the hyperfine interaction simply splits the electron energy levels by the coupling strength. The hyperfine couplings observed this way for example also allow to use nuclear spins as a resource for quantum computing [30]. Due to the aforementioned natural abundance of 1.1% for ^{13}C spins, for many NV–centers hyperfine coupling of single carbon nuclear spins is not resolved in pulsed ODMR spectroscopy (but can still be unraveled with more advanced sensing schemes [96]). The spin bath formed by the carbon spins due to dipolar coupling among them induces decoherence as discussed in chapter 2.2.5.

2.2.2. Rabi Oscillations

Since the presence of an external magnetic field removes the $|\pm 1\rangle$ states' degeneracy, we can effectively think of the NV–center as a two level system (often also referred to as a quantum mechanical bit, or qubit) when applying microwave radiation selective to either the $|0\rangle \rightarrow |+1\rangle$ or $|0\rangle \rightarrow |-1\rangle$ electron spin transitions. Application of this oscillatory driving field on the two level system allows to coherently drive the spin system, which implies that we can create any superposition of the eigenstates $|\Psi\rangle = \alpha\,|0\rangle + \beta\,|-1\rangle$

with complex factors α, β, by varying the pulse length and phase of the microwave radiation [97].

Indeed, the application of the measurement sequence figure 2.8a, in which the length τ of the resonant microwave pulse is varied between readouts, reveals an oscillatory behavior called a Rabi oscillation as shown in figure 2.8b.

These findings can be rationalized conveniently in the Bloch sphere picture (2.8c), which depicts the spin state on a sphere in a frame rotating at the resonance frequency ω_0 (also known as rotating frame, see chapter 2.3.3 for more details). The two eigenstates $|0\rangle$ and $|-1\rangle$ lie at the poles of the sphere. Any superposition state can be visualized by a vector in between the poles. Especially the coherent superposition states

$$|\sigma\rangle = \frac{1}{\sqrt{2}} \Big(|0\rangle + e^{-i\phi} |-1\rangle \Big) \tag{2.2}$$

are points on the equator of the sphere, where the complex phase ϕ determines the direction, e.g. $\phi = 0$ along the x-axis $\phi = \pi/2$ along the y-axis.

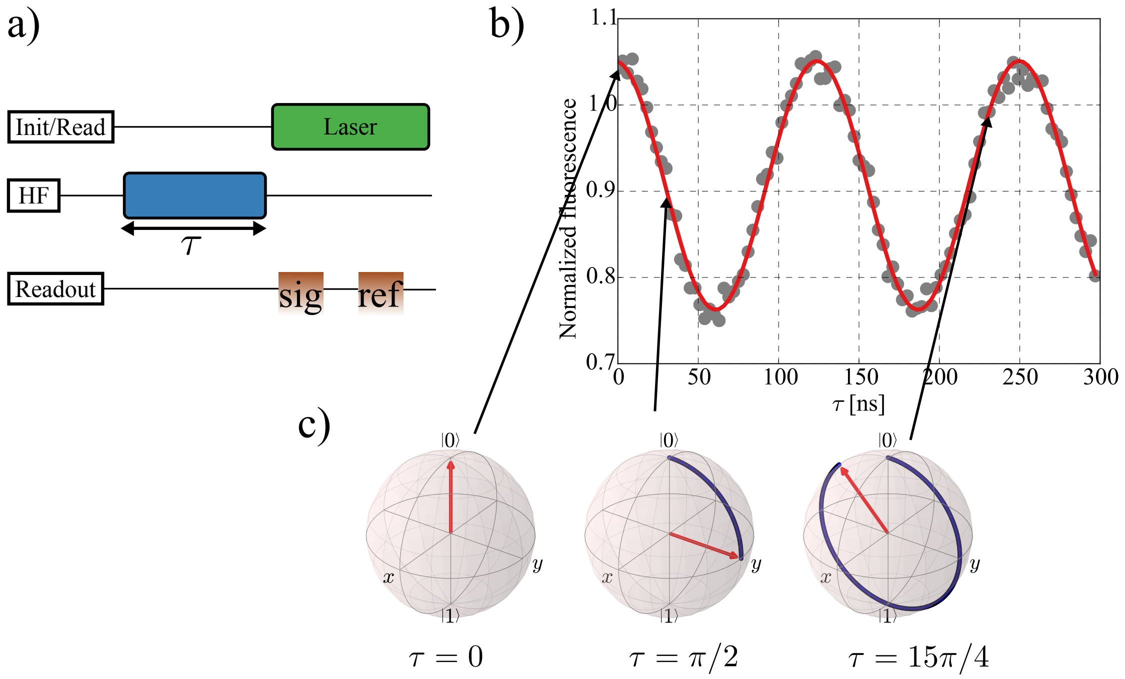

Figure 2.8.: Rabi oscillations of the NV–center spin between two Zeeman substates. a) Measurement sequence, the resonant microwave pulse length is varied. b) Measurement of Rabi oscillations between $|0\rangle$ and $|-1\rangle$ at an external field of 100 Gauss. The signal is normalized using a division of signal against reference window counts. c) Bloch sphere representation of the spin state after the application of the microwave pulse at different points in time.

A driving field at the resonance frequency ω_0 with magnitude B_1 in the Bloch sphere picture is simply a constant field pointing along the x-axis. The direction of the constant field is initially arbitrary and can therefore without loss off generality be chosen along the x-direction. When applying multiple microwave pulses with different phases with respect to each other, direction is set by the phase (e.g. a microwave phase of $\pi/2$ corresponds to a driving field along the y-axis). In a semi-classical picture, the constant driving field in x-direction will cause a Larmor precession of the spin dipole and therefore rotate the spin state by an angle $\Omega\tau = \gamma B_1 \tau$ around the x-axis. This means, that the spin state will continuously oscillate between the poles of the Bloch sphere. Since a laser spin state readout is effectively a projection measurement along $\hat{S}_z$ we accordingly see a sinusoidal oscillation. Indeed, when calculating the expectation value to find the spin state in $|0\rangle$, which is proportional to the acquired fluorescence signal, we get:

$$|\langle\Psi(\tau)|0\rangle|^2 = \left(\frac{\Omega}{2\Omega_{\text{eff}}}\right)\sin^2\left(\frac{\Omega_{\text{eff}}\tau}{2}\right) \tag{2.3}$$

with effective Rabi-frequency $\Omega_{\text{eff}} = \sqrt{\Omega^2 + \Delta^2}$, where $\Delta = \omega - \omega_0$ describes the detuning of applied radiation frequency ω from the actual resonance frequency ω_0. When the excitation is perfectly on resonance, $\Delta = 0$, the expression simplifies to a simple cosine oscillation, which is also used to fit the measurement in figure 2.8b. For this case it is also possible to fully transfer the spin state polarization from $|0\rangle$ to $|1\rangle$ with a microwave pulse of precisely the length $\tau = \pi/(\gamma B_1/2)$, which is referred to as a π pulse, since it corresponds to a rotation in the Bloch sphere by 180°. Accordingly we can note microwave pulses with the amount of rotation they induce and around which direction in the subscript if necessary, for example $(\pi/2)_y$ is a rotation of the spin state around the y-axis by $\pi/2$. In principle, this allows the creation of any superposition of states desired by the application of microwave pulses of appropriate length to determine the flip angle and appropriate phase to determine the flip axis. This kind of coherent control over the NV–center spin state is the key for more advanced sensing schemes described and used in the remainder of this thesis.

2.2.3. Lifetime

At this point, the reader might wonder how long the prepared states described in the last subsection actually persist over time. This question actually lies at the heart of quantum sensing and can yield a lot of information about the environment of the NV–centers under investigation. For this, we have to distinguish between processes that have an effect of the actual spin state population, often referred to as longitudinal relaxation, and processes that affect the coherence of prepared states, sometimes referred to as transverse relaxation, which will be discussed in the next sections.

The quantity that describes how long a quantum state is preserved before decaying into its thermal equilibrium population due to environmental processes is often referred to as spin state lifetime, longitudinal, or spin-lattice relaxation with the corresponding timescale T_1. This corresponds to the decay of spin polarization, or in a sense an actual 'flip' of the spin state due to random energy exchange with the environment. Therefore this quantity is susceptible to processes resonant with the NV spin state transitions $|0\rangle \leftrightarrow |\pm1\rangle$, tunable by an external magnetic field.

These transitions usually fall in the range of lattice phonons, which can therefore act as a relaxation channel for spin polarization via direct electron-phonon interaction. Additionally, an indirect phonon-mediated process can provide energy for spin flips, namely inelastic scattering of higher energy phonons (Raman process). However, due to the high Debye temperature of diamond ($T_D = 1800$ K) the phonon DOS is low[4] even at room temperature which results in comparatively long T_1 times, theoretically several tens of seconds at room temperature [36].

These very long longitudinal relaxation times are however rarely achieved in the experiment. Due to the presence of other paramagnetic impurities within the diamond lattice, e.g. nitrogen impurities or other NV–centers, dipolar or hyperfine coupling causes spin flip-flops. Accordingly, even at lower temperatures where the influence of phonons is negligible, T_1 is usually limited by these couplings and rarely exceeds a second [98].

In figure 2.9a the measurement sequence to probe a T_1 relaxation is shown. It is comprised of two successive laser pulses of variable delay τ. Via fluorescence readout we therefore directly measure how much population remains in the $|0\rangle$ state after τ, having polarized the spin to $|0\rangle$ via laser irradiation beforehand. As can be seen on the blue curve in figure 2.9b, this is already enough to extract a value for T_1. However, many measurements, unlike the shown one, suffer from instabilities in the laser count or overshadowing processes like NV charge state switching. This can cause an indistinguishable zero-point of the decay and hence it is not clear when the NV spin is in its thermal state. For this reason we can shuffle the population to the $|\pm1\rangle$-levels via a π-pulse directly after polarization, which will induce an inverse decay. The fluorescence level increase in this case is only 50% of the $|0\rangle$ decay. This is explained by the fact that both $|+1\rangle$ and $|-1\rangle$ states are dark, while only the $|0\rangle$ state is bright. In the thermally

---

[4] Special attention has to be paid to the Zeeman splitting which can, for certain magnetic fields, bring the transition frequencies into ranges where this is not true any more.

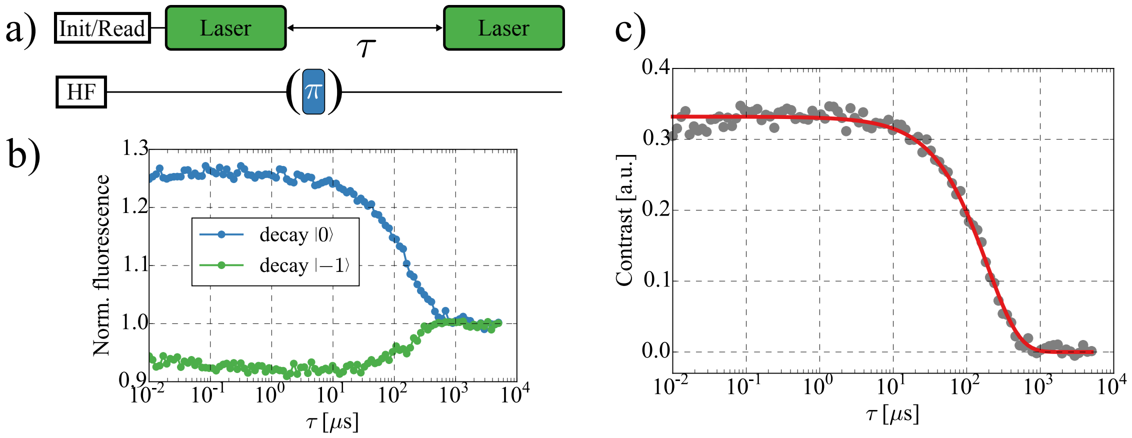

Figure 2.9.: Determination of spin state lifetime T_1 at $T = 300$ K. a) Readout scheme for a lifetime measurement. The waiting time τ between two Laser pulses is swept, while there can be a π pulse at the beginning of the waiting time to either probe the $|0\rangle$ or the $|\pm1\rangle$ spin substate lifetime. b) Measurement of two substate lifetimes on a shallow NV–center. The decay of the $|\pm1\rangle$ has 33% contrast of the $|0\rangle$ state. c) Total NV–center T_1. The data is described by a simple exponential decay.

mixed state all three states are populated equal and thus the bright decay amounts to twice the contrast of the dark ones.

One can now subtract both measurements to generate a spin contrast decay curve, which will yield the T_1-time free from other decay processes as shown in figure 2.9c. This procedure of measuring a contrast instead of pure fluorescence aids significantly in removing artifacts from measurement curves and will be used in most of the pulsed measurements as described later on.

Spectral Filter Function

The NV spin state lifetime can be influenced by external magnetic field noise that has some spectral overlap with the two electronic ground state transitions. As for all of the following measurement sequences, we can assign a specific filter function $F(\omega)$ to the measurement scheme, which expresses how the NV–center spin state is influenced by magnetic noise in the environment under this pulse sequence. This is a central point, widely employed in spin relaxometry in regular ESR and NMR techniques. The additional environmental relaxation rate Γ_{env} is therefore comprised by a convolution of the (environmental) magnetic noise spectral density $\delta(\omega)$ and the sequence specific filter function $F(\omega)$:

$$\Gamma \propto \int_0^\infty F(\omega)\delta(\omega)\mathrm{d}\omega. \tag{2.4}$$

For a longitudinal relaxation measurement this boils down to the application of Fermi's golden rule, i.e. the filter function for a T_1 measurement $F_{T_1}(\omega)$ consists of two Lorentzians at frequencies $\omega_\pm = D \pm \gamma B_z$ with a linewidth due to inhomogeneous broadening $\nu = 1/T_2^*$:

$$F_{T_1}(\omega) = \frac{\nu}{\pi\nu^2 + (\omega - \omega_+)^2} + \frac{\nu}{\pi\nu^2 + (\omega - \omega_-)^2}. \tag{2.5}$$

Owing to the relatively large zero field splitting parameter D, even at zero magnetic field, environmental magnetic noise needs to be fluctuating at GHz frequencies to have an influence on longitudinal relaxation of the NV–center (see chapter 2.2.6 for further discussion).

2.2.4. Free Induction Decay

While it was explained how long the population remains in spin substates of the NV–center in the previous chapter, there is another quantity that is much more sensitive towards external magnetic fields. This quantity is called quantum coherence, which is the property of a quantum mechanical system, that refers to the phase of a quantum state and the ability of this phase to generate interference. In general this refers to the time dependent phase $\phi(\tau)$ in the previously introduced superposition state (eq. 2.2):

$$|\sigma\rangle = \frac{1}{\sqrt{2}}\left(|0\rangle + e^{-i\phi(\tau)}\,|-1\rangle\right) \tag{2.6}$$

and specifically how long this phase relationship holds.

Commonly $\phi(\tau)$ is affected by magnetic fields due to the Zeeman interaction. Namely, the spin substate $|0\rangle$ is insensitive to Zeeman interaction ($\mathrm{m_S} = 0 \Rightarrow H_{\mathrm{Zeeman}} = 0$), while states $|\pm1\rangle$ will have a Zeeman interaction differing from zero. Hence, if Zeeman interaction is present, it will lead to a phase pickup of the state $|\pm1\rangle$ with respect to the state $|0\rangle$. In the Bloch picture, this phase pickup corresponds to a rotation around the z-axis. In an interaction free world with perfectly on-resonant pulses, the phase gain would be zero in the rotating Bloch frame, since here the static magnetic field vanishes (no Zeeman interaction). However, any fields that have a detuning to the Larmor frequency set by the static magnetic field give rise to a Zeeman interaction term, and thus give rise to a phase. The phase pickup can be expressed as:

$$\begin{aligned} \phi(\tau) &= \gamma \int_0^\tau b_{\text{eff}}(t)\ \mathrm{d}t \\ \text{with} \quad b_{\text{eff}}(t) &= \frac{1}{\gamma} \sum_i^n \omega_0 - \omega_i(t) \end{aligned} \tag{2.7}$$

where b_{eff} is a sum over all sources of magnetic field detunings at the position of the NV–center. Naturally those fields can hold a time dependency, according to the nature of the source. A nuclear spin close to the NV–center for example generates a magnetic field oscillating at the nuclear Larmor frequency, while a paramagnetic species on the diamond surface might cause a constant magnetic field, which can however flip at random points in time due to thermal processes.

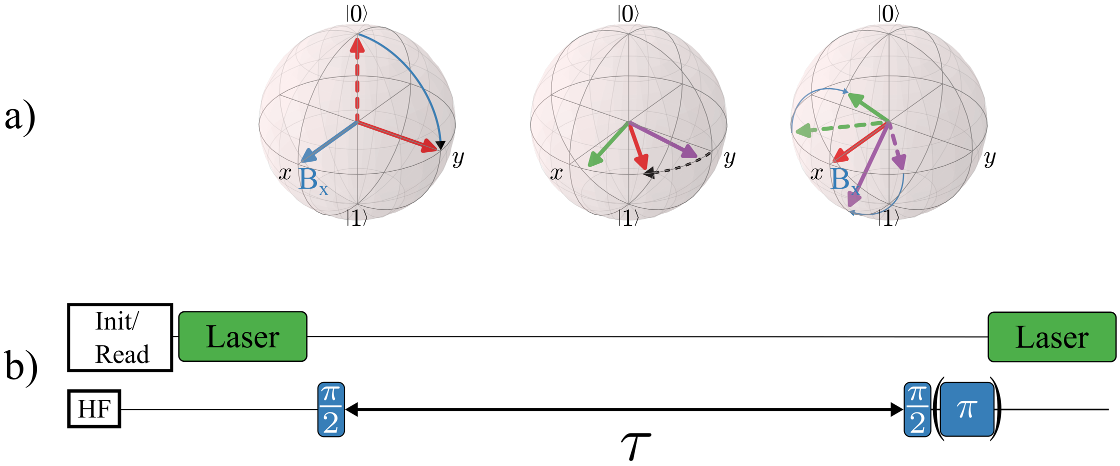

Figure 2.10.: Sequence for a free induction decay measurement. a) Evolution of the spin state in the Bloch sphere picture at different points in time of the sequence. b) Measurement sequence. Every point is measured twice with an additional π pulse to generate spin contrast.

To probe this coherent behavior, a so-called Ramsey sequence or free induction decay (FID) is used, which is in complete analogy to conventional EPR-experiments. The sequence is depicted in figure 2.10 and consists of two consecutive $(\pi/2)_x$-pulses with a variable time delay τ between them before a population-readout. The action of the first $(\pi/2)_x$-pulse is to create the superposition $|\sigma\rangle$, where the phase is zero in the beginning (see first Bloch sphere in fig. 2.10a). In the variable delay time a phase will be picked up due to fields in the environment. There can be multiple field sources present which is represented by three differently colored spin state arrows in fig. 2.10a. A final $(\pi/2)_x$ will convert this phase pickup to an actual population difference on the z-axis that is readable by a laser pulse. This way we directly transfer phase information to an actual fluorescence. To make the measurement readout more robust against artifacts, every point is measured twice, once with an additional π_x pulse at the end generating fluorescence contrast upon subtracting the results of both measurements.

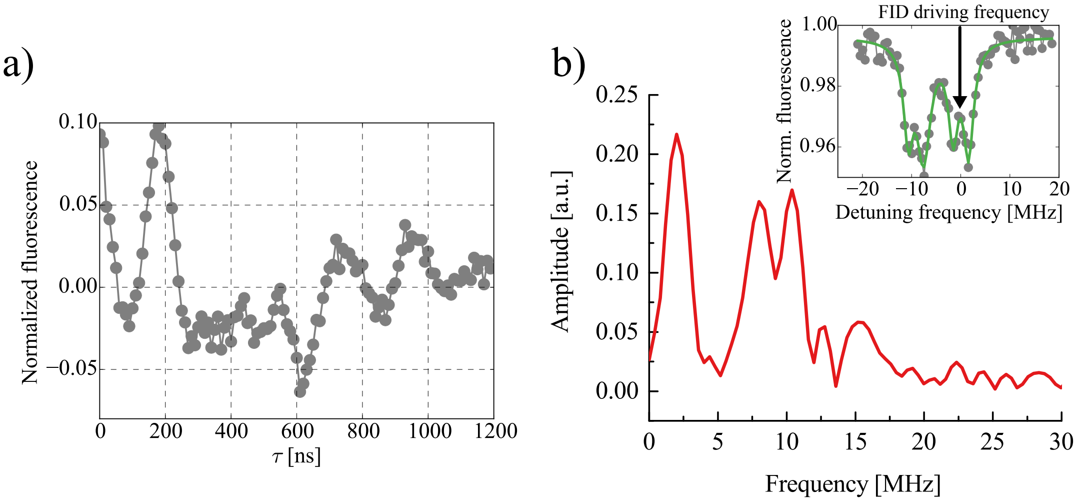

Figure 2.11.: FID measurement. a) Measurement data on a typical NV–center. The envelope yields the T_2^* time, usually below 1 μs for shallow implanted NV–centers. b) FFT of the measured signal. We can distinguish couplings that most likely stem from the closeby ^{15}N nuclear spin and a weakly coupled ^{13}C spin.

An actual FID measurement on a shallow NV–center is shown in figure 2.11a. A clear beating of the spin contrast is visible. This becomes even more apparent when applying a Fourier transformation (FFT) on the acquired data, shown in figure 2.11b. The beating is caused in this case by the hyperfine interaction of the NV–center with surrounding nuclear spins. Obviously, there is always a hyperfine interaction with the connected nitrogen nucleus of the NV–center. For the case of ^{15}N, there are two hyperfine transitions possible which yields two detunings to the applied microwave pulse frequency. In the case of the present measurement, the microwave frequency was applied directly in between these two hyperfine transitions(see pulsed ODMR spectrum inset), which gives one degenerate detuning around 1.5 MHz. The other two peaks stem from hyperfine coupling to a closeby ^{13}C carbon nuclear spin, which gives two additional detunings at approximately 7 MHz and 10 MHz. All of these detunings cause a time dependent phase pickup and hence the oscillation frequencies which can be directly observed in our measurement.

Furthermore, the measurement contrast decays over time. This is caused by random magnetic field noise, inducing decoherence and eventually rendering the phase relationship of equation 2.6 invalid. The decay envelope of an FID measurement has a typical timescale, usually labeled T_2^*, which for shallow NV–centers is usually on the order of $1\ \mu$s as for the one shown in graph 2.11a. The main source of decoherence in the diamonds used in this work is the nuclear spin from $^{13}\mathrm{C}$ carbon atoms, which can be found with a 1.1% abundance within the diamond lattice. The hyperfine coupling of the magnetic moments from these nuclear spins to the electronic spin of the NV–center induces random magnetic noise, eventually destroying any phase relationship between the electronic spin eigenstates. This is due to the fact that the carbon spins are coupled among each other by spin flip-flop terms and correspondingly can change their conformation at random points in time. Such a system of hyperfine coupled, flipping spins is termed a spin bath and will be described in more detail in the next section. Since a single measurement is always averaged over many millions of runs, the different magnetic conformations cause an overall decay, called inhomogeneous broadening. Obviously there can also be inhomogeneous broadening due to imperfections in the experimental equipment, like power instabilities, which is however assumed to be too small to observe for this work.

Spectral Filter Function

Considering the sequence used for Ramsey spectroscopy, it becomes apparent that a time-constant (i.e. constant in time over the duration of the measurement τ) frequency detuning will have the largest impact on the measurement signal. In contrast to this a quickly oscillating magnetic field will be averaged out (see eq. 2.7) and will have no influence on the measurement. Accordingly, one can calculate the FID filter function to [99]:

$$F_{\mathrm{FID}}(\omega) = \left| \frac{\sin \frac{\omega\tau}{2}}{\frac{\omega}{2}} \right|^2 . \tag{2.8}$$

In the time domain, sensitivity to magnetic fields of the FID sequence is a rectangular function (maximally sensitive to magnetic fields in between the two microwave pulses, zero otherwise). A Fourier transformation of this time dependent rectangular function leads to the above shown sinc-function. Accordingly, the FID sequence is most sensitive to constant magnetic fields, where the sensitivity limit is set by the dephasing T_2^* time (see section 2.2.6 for further discussion).

2.2.5. Spin Echo

A powerful method to extend the coherence of a superposition state $|\sigma\rangle$ is to refocus the spin state dephasing mechanism. This can be achieved by applying a π-pulse after some time of free evolution. This way the magnetic interactions are inverted (i.e. sign of picked up phase changes) and a so called spin echo will occur after the same amount of time when the acquired phase has canceled. This technique is also, in its simplest form, referred to as Hahn echo after physicist Erwin Hahn, who pioneered the field of pulsed spectroscopy [100] in NMR.

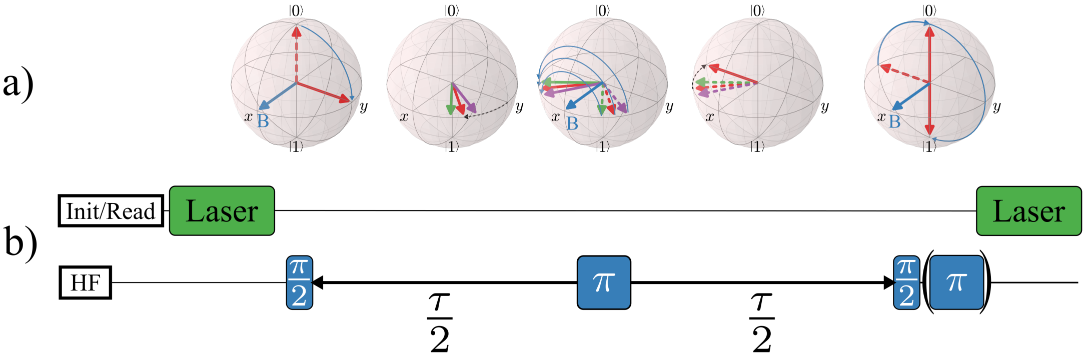

c) $$|\Psi\rangle = |0\rangle \Rightarrow |0\rangle + |1\rangle \Rightarrow |0\rangle + e^{-i\phi_1 \frac{\tau}{2}}\,|1\rangle \Rightarrow e^{-i\phi_1 \frac{\tau}{2}}\,|0\rangle + e^{-i\phi_2 \frac{\tau}{2}}\,|1\rangle \Rightarrow e^{-i(\phi_1-\phi_2)\frac{\tau}{2}}\,|0\rangle$$
$$e^{-i(\phi_1-\phi_2)\frac{\tau}{2}}\,|1\rangle$$

Figure 2.12.: Measurement scheme of a Hahn Echo on an NV–center. Alongside the microwave pulses, Bloch spheres are shown. These illustrate the evolution of the NV–center qubit state.

Hahn Echo

The measurement sequence for a Hahn echo is depicted in fig. 2.12. In principle, it is an FID measurement as described in the previous section with a refocusing $\pi_{x,y}$ pulse at half the evolution period (direction of the microwave field does not matter for a single pulse). Again, the superposition state $|\sigma\rangle$ is created by a combined laser and $(\pi/2)_x$-pulse as depicted in figure 2.12a. During the free evolution period of duration $\tau/2$ a phase $\phi_1(\tau/2)$ will be picked up according to equation 2.7. In the Bloch picture (fig. 2.12a this can again be expressed by arrows that acquire a phase of different magnitude corresponding to varying magnetic environments at multiple measurement runs. The application of a resonant π_x-pulse corresponds to a flip of these differently evolved spin states by $180°$

around the x-axis. This effectively changes the sign of phase accumulation[5] $\phi_2(\tau/2)$ during the second free evolution period. Consequently, the phase pickup is canceled if both time intervals are chosen to be the same and thus the original state $|\sigma\rangle$ will be restored. At the end of the sequence, the remaining phase difference is again converted to a population difference by a $(\pi/2)_x$-pulse.

The resulting phase at the end of a Hahn sequence can thus, in analogy to eq. 2.7, be calculated to:

$$\varphi(\tau) = \gamma \left(\int_0^{\tau/2} b_{\mathrm{eff}}(t)\ \mathrm{d}t - \int_{\tau/2}^{\tau} b_{\mathrm{eff}}(t)\ \mathrm{d}t \right). \tag{2.9}$$

Obviously, the total phase pickup after completion of the whole sequence will not be canceled by any form of time dependency in the magnetic field $b_{\mathrm{eff}}(t)$. To be more precise, one can imagine time dependent magnetic fields, where the effect of phase canceling is neglected due to alternating field strengths in the two arms of the Hahn echo (for example simply a sinusoidal magnetic field with frequency $f = \tau^{-1}$). Nonetheless, the phase pickup is zero for all constant or low frequency $f \ll \tau^{-1}$ detunings, as well as for fields with exceedingly high frequencies $f \gg \tau^{-1}$. This decouples the NV electron spin much more effectively from the environment as the previous FID sequence.

Indeed, when measuring the specific coherence decay constant termed T_2 or transverse relaxation time, much larger values are obtained ($T_2^* < T_2$) as can be seen from comparing the decay envelopes in figure 2.13a+b with the one obtained for an FID measurement in the last chapter. The reason is that we make the NV spin insensitive to some frequencies, comparable to the behavior of a (quantum-) lock-in amplifier.

Interestingly, a sweep of the free evolution time τ yields a much more rich behavior for low magnetic fields, visible by the loss and revival of coherence in graphs 2.13a+b. This kind of experiment is often referred to as electron spin echo envelope modulation (ESEEM). The reason for this is the $^{13}\mathrm{C}$ nuclear spin bath, or rather the Larmor precession of its nuclear spins. Whenever the total free evolution time τ matches a multiple of the inverse $^{13}\mathrm{C}$ Larmor precession (gyromagnetic ratio: $\gamma_{^{13}\mathrm{C}} = 10.705\ \mathrm{MHz\ T^{-1}}$), a random phase is acquired by the NV spin state. This leads to a periodic loss of coherence and a revival, whenever the free evolution time coincides with the $^{13}\mathrm{C}$ Larmor precession or a multiple of it.

---

[5] For the NV–center three level system this is less intuitive. Yet, this can easily be rationalized on a two level system: states $|+1/2\rangle$ that acquired a positive phase prior to a π-pulse are flipped to $|-1/2\rangle$ and have a negative Zeeman term and phase pickup subsequently.

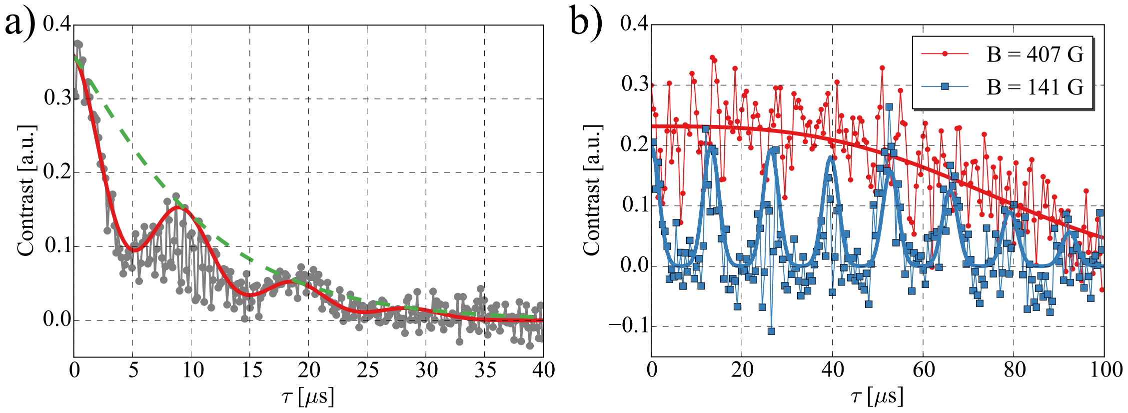

Figure 2.13.: Hahn Echo on single NV–centers. a) Hahn echo measurement on a single shallow implanted NV–center (5 keV). To reproduce the data, we have to take the $^{13}\mathrm{C}$ spin bath surrounding the NV–center into account. The envelope yields the $\mathrm{T}_2 = 10.7\mu\mathrm{s}$. b) Same measurement on a second NV–center with $\mathrm{T}_2 = (85.4 \pm 2.5\mu s)$. The shown data is measured at two different fields to point out that we can remove the apparent effect of the carbon spin bath on the decoherence, using higher fields.

The decay envelope of the measured coherence coupled to a carbon spin bath can be described by an exponential function $\exp(-(\tau/T_2)^\alpha)$, where α is typically between 2 and 3 [101]. The value of α hereby strongly depends on the actual bath configuration, i.e. the positions of the $^{13}\mathrm{C}$ in the diamond lattice and the resulting hyperfine couplings to the NV–center. In figure 2.13a the value is $\alpha = 1.14 \pm 0.06$, which suggests comparatively fast spin bath dynamics [101]. To model the full dephasing, we can use the formula [102]:

$$C(\tau) = A \exp\left(-\left(\frac{\tau}{T_2}\right)^\alpha\right) \sum_i \exp\left[-\left(\frac{\tau - 2i\tau_{^{13}\mathrm{C}}}{\tau_{\mathrm{width}}}\right)^2\right] \tag{2.10}$$

As illustrated in figure 2.13b, we can get rid of the carbon nuclear spin revivals in a Hahn measurement. By increasing the magnetic field strength, the Larmor precession frequency eventually gets too fast to cause any phase pickup during the measured τ values and only the decay envelope remains.

Dynamical Decoupling

To even further decouple the NV spin from its magnetic environment and prolong the transverse spin relaxation time one can apply more advanced dynamical decoupling schemes known from pulsed ESR and NMR spectroscopy. The idea is to insert more than one refocusing pulse, increasing the effect of phase cancellation and prolonging the

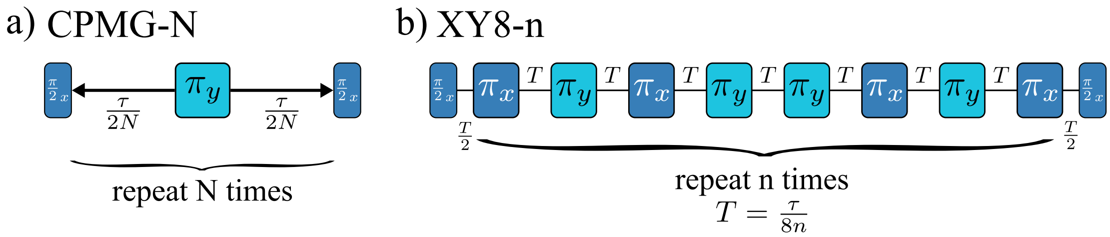

Figure 2.14.: Microwave pulse scheme for a) CPMG-N and b) XY8-n dynamical decoupling sequences. Indices at the pulses specify the direction of magnetic field in the Bloch sphere (dark blue along x, light blue along y). The total sequence length in both cases is τ.

time the NV–center spin is sensitive to magnetic fields. This idea was first formulated by Carr and Purcell shortly after Hahn's discovery of the spin echo in 1954 [103], where N π-pulses with equal spacing instead of just one are inserted in between the two $\pi/2$-pulses. This was subsequently refined by Meiboom and Gill, generating the π-pulses on a different axis than the $\pi/2$-pulses to compensate for pulse errors. The sequence named Carr-Purcell-Meiboom-Gill (CPMG) is shown in figure 2.14a. Its application preserves the spin state well along the direction of applied refocusing pulses and can substantially increase the T_2 time. Nonetheless it is still prone to imperfections in microwave pulses (power and frequency instabilities, finite pulse lengths, ...) and phase noise along different directions in the Bloch sphere.

The robustness and efficiency of the applied pulse scheme can be significantly increased by various concepts. One frequently used extension is shown in figure 2.14b, where a symmetric sequence of eight alternating pulses along x- and y-direction is used. This scheme is referred to as $XY8-n$ scheme, with n the number of times the symmetrical pulse sequence is applied which gives a total number of $N = 8n$ refocusing pulses. The alternating $\pi_{x,y}$-pulses very efficiently cancel out pulse errors and the symmetrical shape of the sequence decouples against phase noise in all possible directions. Accordingly, the $XY8-n$ sequence has been shown to surpass the CPMG sequence in performance in most cases [104].

There are a wide variety of sophisticated techniques to further decouple a spin qubit from its detrimental environment, like using more robust composite pulses [105] or tailoring the sequence specific to the environment via optimal control [106]. An exciting development over the last years was to use the long lived nuclear qubits in proximity to the NV electronic qubit, to store and preserve its quantum state [43, 107, 108]. These techniques are however not discussed here, since they will not be used in the framework of this thesis.

Spectral Filter Functions

As mentioned earlier, the sign of magnetic field sensitivity is switched by a $(\pi)_{x,y}$-pulse. In the time domain, the sensitivity function is thus alternating between $+1$ and -1. If we apply the Fourier transformation to this alternating square function, we arrive at the spectral filter functions for spin echo decoupling:

$$\begin{aligned} F_{\text{Hahn}}(\omega) &= \left| \frac{\sin^2 \frac{\omega\tau}{4}}{\frac{\omega}{4}} \right|^2 \\ F_{\text{XY8-N}}(\omega) &= 2 \left| \frac{\sin \frac{\omega\tau}{2}}{\frac{\omega}{2}} \frac{\sin^2 \frac{\omega\tau}{4N}}{\cos \frac{\omega\tau}{2N}} \right|^2 . \end{aligned} \tag{2.11}$$

Where F_{Hahn} is the function for a Hahn sequence and $F_{\text{XY8-N}}$ is the spectral filter function for a dynamical decoupling sequence with $8 \cdot N$ π-pulses. The effect of applying multiple decoupling pulses is thus to create a more narrow spectral filter, which in turn increases the resulting T_2 time as one decouples the NV–center electron spin from environmental magnetic field noise. See section 2.2.6 for further discussion.

2.2.6. Quantum Spectroscopy

Measurements on the various (dynamic) spin properties of a qubit can be utilized for magnetic field sensing. The ability to use a single isolated NV–center spin, essentially constituting an atomic sized sensor, in close proximity to the diamond surface enables magnetometry (and measurement of other properties) on nanoscale sample volumes. This poses one of the key outstanding characteristics of NV magnetometry, since most other magnetic field sensing techniques are often limited to large ensemble measurements and thus only achieve single spin sensitivity with great effort [16]. The presented pulsed schemes at the same time give great control over an extremely large frequency span of DC to AC magnetic fields, unprecedented by other techniques. In figure 2.15 the different filter functions are plotted with specific parameters to visualize this versatility of magnetic sensing.

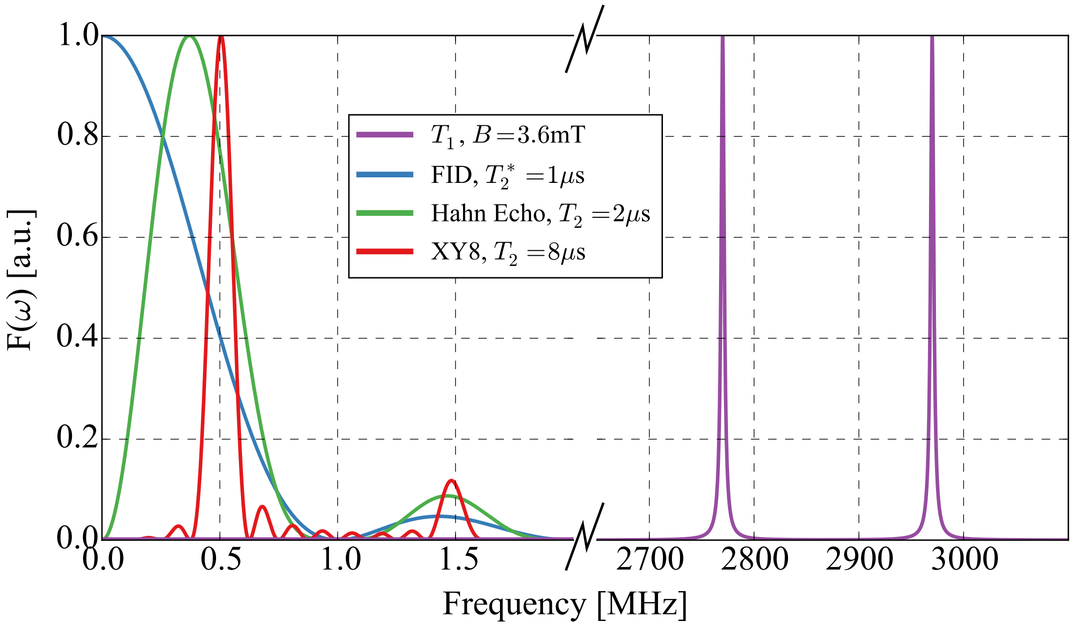

Figure 2.15.: Spectral filter functions for different measurement types. Specific values used for calculation are indicated in the legend.

DC Magnetometry

The precise measurement of Zeeman splittings either via pulsed ODMR or FID allows the determination of DC or low frequency magnetic fields by either monitoring transition frequencies or Fourier transformation of the FID signal. The filter function $F_{\mathrm{FID}}(\omega)$ (eq. 2.8) in figure 2.15, shows that indeed the FID sequence is most sensitive to DC magnetic fields and quickly drops to zero, while the upper frequency bound is defined by the chosen free evolution time τ. The sensitivity is hereby naturally limited by the linewidth $1/T_2^*$ for pulsed ODMR. In FID this limit likewise emerges as the inescapable loss of coherence. Furthermore, since a finite number of photons are detected, photon shot noise contributes to the detectable impact of magnetic field on the ODMR signal. The magnetic field sensitivity can thus be calculated to [37, 48]:

$$\eta_{dc} \simeq \frac{1}{\gamma C \sqrt{I_0 t_{\mathrm{sig}}}} \frac{1}{\sqrt{T_2^*}}, \tag{2.12}$$

with photon countrate I_0, length of detection window t_{sig} (around 300 ns) and ODMR contrast C (around 0.3). Sensitivity in this context expresses the minimum detectable field per square root of measurement time or the minimum magnetic field that gives a SNR of 1. In isotopically purified diamond samples T_2^* can reach up to ~ 100 μs [109] for artificial NV–centers less than 100 nm below the diamond surface or even 0.6 ms for deeper ones [36]. This leads to an achievable magnetic field sensitivity of around $\eta_{dc} \sim 40\ \mathrm{nT\ Hz^{-1/2}}$. This sensitivity for example could enable the detection of the Zeeman shift due to a single electron spin within a distance of 45 nm, or a single proton spin in a distance of 5 nm. This sensitivity unfortunately is out of reach for DC sensing experiments with currently used shallow NV–centers. Real sensitivities usually lie in the $\eta_{dc} \sim \mu\mathrm{T\ Hz^{-1/2}}$ range and are hampered by aforementioned spin noise from nitrogen and carbon spins and the significant increase of inhomogeneous broadening from close proximity to the diamond surface. Most notably however, the poor photon collection efficiency still has the highest negative impact on sensitivity [49]. Many experiments have been reported, advancing the field of DC NV mangetometry, for example detecting magnetic domain boundaries in ferromagnetic materials [110–112], imaging of single vortices in superconductors [113, 114] or current flow in graphene [115].

Decoherence Magnetometry

Another method for magnetic field sensing is monitoring detrimental effects caused by randomly fluctuating magnetic fields on the T_1, T_2^* or T_2 time [116, 117]. Here, the dephasing $\Gamma = \Gamma_{\mathrm{int}} + \Gamma_{\mathrm{ext}}$, comprised of internal dephasing from the diamond host material and additional external dephasing, e.g. from the material under investigation, is monitored.

As depicted in figure 2.15 for a small magnetic field, T_1 is sensitive to magnetic field noise at the NV–center transition frequencies $\omega = D \pm \gamma B$. This can be utilized for sensing by bringing the NV–center into close proximity of the material of interest, or vice versa, monitoring its T_1 time and subsequently deducing material parameters. Due to the large ZFS parameter $D = 2.87$ GHz, the fluctuations arising from these materials must be in the GHz region for small fields. This frequency window is usually too high to be influenced by Larmor precession of electron or let alone nuclear spins (~ 100 MHz or kHz respectively at $B = 100$ Gauss). Nonetheless, in molecular systems fast spin fluctuations can arise from spin-phonon interactions and rotational and translational diffusion. In this fashion, the impact of gadolinium and manganese ions, as well as iron clusters in ferritin molecules on T_1 in vicinity of the NV–center has been studied [118–120], which can even be performed in a scanning geometry [121, 122]. Additionally, spin baths of paramagnetic defects at the diamond surface have been studied using T_1-relaxometry [123, 124].

The sensitivity of decoherence techniques is actually comparable to the sensitivities achieved with Ramsey type sensing sequences [117, 125]. Thus, it has been shown that even the induced relaxation of a single (gadolinium) spin can be detected from a distance of 6 nm [126]. The NV-transition can be tuned to almost any frequency by varying the on-axis magnetic field. Most recently it has even been shown, that by tuning the transition frequencies close to the ground state level anticrossing (GSLAC), one can detect nuclear and electron spin precessions using T_1 relaxation. Due to increased cross-relaxation at level crossings with the external spin species, spectroscopy on small ensembles of nitrogen defects in the diamond lattice and even hydrogen nuclear spins external to the diamond lattice has been performed [125, 127]. Hereby the magnetic sensitivity reaches values close to techniques presented in the next subsection, yet a decisive limit is that the frequency resolution is governed by the transition linewidth $(1/T_2^*)$, which can be overcome by decoupling the NV spin from its environment using AC magnetometry schemes.

AC Magnetometry

Compared to DC sensing schemes the sensitivity can be significantly increased by using the decoupling techniques described in chapter 2.2.5, due to the potential to choose longer free evolution times which improves phase acquisition. This is achieved by the refocusing π-pulses, limiting the detection bandwidth to a sensitivity window at higher frequencies. Indeed, in figure 2.15 the depicted sensitivity function $F_{\mathrm{Hahn}}(\omega)$ (eq. 2.11) is completely insensitive towards low frequencies and has maximum sensitivity for the frequency set by the free evolution time $f = \tau^{-1}$.

The reason for the high performance of decoupling schemes on the NV–center in diamond is the noise spectrum $S_{\mathrm{bath}}(\omega)$ of the surrounding spin bath of carbon and/or nitrogen spins. The behavior of such a spin bath can be modeled by an Ornstein-Uhlenbeck process in the many body limit [128], essentially described by the two parameters mean magnetic field strength b_{bath}, which is the coupling of bath to NV–center and correlation time τ_c, the average bath spin flip-flop frequency which is determined by the average intrinsic bath coupling strength. The spin bath will create a random magnetic field with a zero mean value $\langle B \rangle = 0$ but a non vanishing root-mean-square value $\sqrt{\langle B^2 \rangle} > 0$. Using the autocorrelation function of the bath magnetic field, which can be approximated by an exponential decay multiplied with the Larmor frequency, a Fourier transform reveals a Lorentzian noise spectrum, which is centered around zero for low external magnetic fields:

$$S_{\mathrm{bath}}(\omega) = \frac{b_{\mathrm{bath}}^2}{\pi} \frac{1/\tau_c}{(1/\tau_c)^2 + \omega^2} \tag{2.13}$$

A shift of the sensitivity window towards higher frequencies thus decouples this noise well from the NV–center, which is reflected by the fact that $T_2 \gg T_2^*$. Advanced pulse schemes yield even narrower detection bandwidths and subsequently higher T_2 values, as, for example, is shown with the filter function of a $XY8-1$ sequence in figure 2.15. When detecting alternating magnetic fields this increase in the relevant transverse spin relaxation time leads therefore to an increased sensitivity of

$$\eta_{ac} \simeq \eta_{dc}\sqrt{\frac{T_2^*}{T_2}}. \tag{2.14}$$

Nowadays, pushing the limits of diamond and NV–center fabrication, T_2 times can reach almost second [36], which leads to sensitivities of $\eta_{ac} \sim 10\ \mathrm{nT\ Hz}^{-1/2}$ [48]. In contrast to the FID sequence, experiments with shallow NV–centers usually come closer to the quoted sensitivity.

Decoupling sequences can be tuned to frequencies of interest via variation of τ. The frequency is limited by the length of a π pulse at the lower end and T_2 at the upper end. This places the maximum sensitivity of decoupling schemes in the kHz to MHz region, which is also the region for Larmor frequencies of nuclear spins at moderate magnetic fields used for NV magnetometry (usually below 1000 Gauss). This has lead for example to hallmark experiments of detecting a very small ensemble of proton nuclear spins [39, 40] and even nuclear magnetic resonance from a single protein [44].

2.3. The NV–Center Hamiltonian

After describing the measurement protocols and experiments that harness the NV–center optical properties for magnetometry, the next section is dedicated to describing the according quantum mechanics. This will later be utilized for a better understanding of performed experiments. As pointed out in the previous chapter, a lot of the way of thinking is borrowed from single molecule spectroscopy and most importantly electron spin resonance and nuclear magnetic resonance.

2.3.1. NV–Center Spin Hamiltonian

The starting point for electronic properties is the Hamiltonian eq. 2.1.

The full Hamiltonian will only rarely be needed to describe a specific problem we are interested in. This equation would give the full electronic energy spectrum which we are mostly not interested in due to the applied cooling mechanism to the ground state as described in chapter 2.1.3. While in this thesis mostly the NV–center spin properties and their reaction to magnetic materials in the vicinity are of interest, we invoke something that is sometimes called the *spin Hamiltonian hypothesis* [97]. That means, we only regard terms containing the spin and include effects like motion of delocalized electrons or orbital effects by averaged factors [129], which can be justified by energy considerations. Most other relevant terms, like e.g. spin-orbit coupling ($\sim 10^{-2}$ eV) are orders of magnitude larger than all terms relevant for spin dynamics considered. Thus kinetic and Coulomb interaction terms are disregarded.

If we now focus solely on the ground state (polarization), the spin-orbit coupling is zero as well ($L = 0$) [85]. Taking this into account we can write eq. 2.1 as the NV–center's ground state spin Hamiltonian [129, 130]:

$$\begin{aligned} H_{\mathrm{NV}}^{\mathrm{spin}} &= H_{\mathrm{ZFS}} + H_{\mathrm{HF}} + H_{\mathrm{NQ}} + \underbrace{\boxed{H_{\mathrm{EZ}} + H_{\mathrm{NZ}} + H_{\mathrm{cpl}}}}_{\text{external magnetic interaction}} \;. \\ &= \boldsymbol{SDS} + \boldsymbol{SAI} + \boldsymbol{IPI} + \mu_B \boldsymbol{B}_0 \boldsymbol{g} \boldsymbol{S}/\hbar + \mu_N \boldsymbol{B}_0 \boldsymbol{g} \boldsymbol{I}/\hbar + H_{\mathrm{cpl}}. \end{aligned} \tag{2.15}$$

All bold written symbols are tensors of first or second rank, $\boldsymbol{S} = (S_x, S_y, S_z)$ is the electron spin operator and $\boldsymbol{I} = (I_x, I_y, I_z)$ the nuclear spin operator of the nitrogen nucleus.

Here, H_{ZFS} is the zero field splitting, due to spin-spin interaction from the two electrons in the highest occupied molecular orbital. If one chooses the coordinate system accordingly, the ZFS interaction can be expressed as $\boldsymbol{SDS} = DS_z^2 + E(S_x^2 - S_y^2)$ [131]. For the NV–center $D = 2.87$ GHz and E is very small compared to D. In perfect axial symmetry the second term is zero, however highly dependent on lattice distortions, i.e. crystal strain [132]. For all of this work we assume that strain is negligible and $E(S_x^2 - S_y^2) = 0$.

H_{HF} is the hyperfine interaction with the nitrogen nuclear spin, which is either a ^{14}N with nuclear spin $I = 1$ or a ^{15}N with nuclear spin $I = 1/2$. The hyperfine interaction can further be simplified to a fully diagonal form $\boldsymbol{SAI} = A_{\parallel} S_z I_z + A_{\perp}(S_x I_x + S_y I_y)$, if the quantization axis coincides with the external magnetic field direction. The hyperfine constants are $A_{\perp} \sim 2.7 - 3.6$ MHz, $A_{\parallel} = 3.1$ MHz for ^{15}N and $A_{\parallel} = 2.3$ MHz for ^{14}N [83].

The nuclear quadrupole term is described by H_{NQ} and only present for ^{14}N with $I > 1/2$. The nuclear quadrupole interaction is $P = 5.2$ MHz [133]. Since all measurements in this thesis will be performed exclusively on NV–centers with a ^{15}N nucleus, we can discard this term.

The term $H_{\mathrm{EZ}} = \mu_B \boldsymbol{B}_0 \boldsymbol{g} \boldsymbol{S}/\hbar$ with $\mu_B = e\hbar/2m_e \cong 28/\hbar$ GHz T^{-1} describes electron Zeeman interaction with an external magnetic field $\boldsymbol{B}_0$. Since orbital contributions to the $\boldsymbol{g}$-tensor can be neglected [68], this expression can be simplified to $\boldsymbol{g} = g \cdot \mathbb{1}$, with $g = 2.0023$. If the magnetic field is oriented along the NV–center principal axis $\boldsymbol{B}_0 = (0, 0, B_z)$ and static, the Zeeman interaction term further simplifies to $H_{\mathrm{EZ}} = \gamma B_z S_z$, with the electron gyromagnetic ratio $\gamma = g\mu_B/\hbar$.

Nuclear Zeeman interaction H_{NZ} can be disregarded most of the times since the nuclear magneton $\mu_N = e\hbar/2m_p$ is orders of magnitudes smaller than any other term, due to the high proton mass $m_p \approx m_e * 2000$ and the fact that we only use comparatively low magnetic fields.

The term H_{cpl} stands for coupling of the NV–center spin to magnetic elements in its environment, if present, and will be discussed in the following subsection.

In summary, we arrive at a very simple form of the NV–center spin Hamiltonian:

$$\boxed{H_{\mathrm{NV}} = D S_z^2 + A_{\|} S_z I_z + \gamma B_z S_z + H_{\mathrm{CPL}}}. \tag{2.16}$$

Here we used $H = H'/\hbar$, i.e. all units are in frequency instead of energy, which will be valid for most of the thesis. This Hamiltonian will be used to describe all phenomena within the framework of this thesis and is valid for most applications in NV magnetometry. Approximations made for its derivation only have to be reconsidered for special cases and one might have to fall back to the more general Hamiltonian 2.15. An important prerequisite is certainly that the external static magnetic field is well aligned with the NV–center axis.

2.3.2. Coupling to Magnetic Systems

Sensor capabilities require an influence by the environment. Various interactions can have a measurable effect on properties of the NV–center, e.g. strain, electric fields (Stark shift) or temperature among others, which are however out of scope of this thesis. For now, we focus on magnetic interactions of the NV–center electron spin with its environment, are described by additional terms H_{cpl} in the NV–center Hamiltonian 2.16.

Isolated spins in close proximity to the NV–center give rise to an additional dipole-dipole interaction term. Dipole-dipole interaction between two spins $\boldsymbol{S}_k$ and $\boldsymbol{S}_l$ with a connecting vector $\boldsymbol{r}_{kl} = r_{kl}\boldsymbol{e}_{kl}$ can be described when applying the point-dipole approximation via the correspondence principle of two magnetic dipoles as:

$$\begin{aligned} H_{\mathrm{dip}}^{kl} &= \omega_{dd}\left(3(\boldsymbol{S}^k\vec{e}_{kl})(\boldsymbol{S}^l\vec{e}_{kl}) - \boldsymbol{S}^k\boldsymbol{S}^l\right) \\ \text{with:}\quad \omega_{dd} &= -\frac{\mu_0}{4\pi}\frac{\gamma_k\gamma_l\hbar}{r_{kl}^3}. \end{aligned} \tag{2.17}$$

Introducing the lowering and raising operators $S_- = S_x - iS_y$ and $S_+ = S_x + iS_y$, the expression can be rewritten as [134]:

$$H_{\mathrm{dip}}^{kl} = \frac{\omega_{dd}}{2}\left(A+B+C+D+E+F\right) \tag{2.18}$$

$$\begin{aligned} A &= 2(3\cos^2(\Theta_{kl})-1)S_z^kS_z^l, \\ B &= (3\cos^2(\Theta_{kl})-1)(S_+^kS_-^l + S_-^kS_+^l), \\ C &= 3\cos(\Theta_{kl})\sin(\Theta_{kl})e^{i\phi}(S_z^kS_+^l + S_-^kS_z^l), &\qquad D &= C^\dagger, \\ E &= \frac{3}{2}\sin^2(\Theta_{kl})e^{i2\phi}S_+^kS_+^l, &\qquad F &= E^\dagger. \end{aligned}$$

In the above form, each term represents a different effect on the dipolar coupled spin system. A describes two classical interacting dipoles, which generate a magnetic field at the position of the other and thus simply shifts the energy of involved states. The B term allows spin flip-flops, i.e. energy transfer between two spins. These two terms commute with the Hamiltonian 2.16 and thus do not change its eigenstates. The terms C, D, E, F however introduce spin state mixing. Fortunately these terms are often very small compared to A and B and can therefore be neglected. This can be treated in a rigorous manner by the so called secular or high-field approximation. The principle idea of this approximation is that H_{dip}^{kl} is expressed in the eigenbasis of $H_{S^k} + H_{S^l}$, which is the Zeeman basis. Terms that connect non-degenerate eigenstates with eigenvalues $\gamma_k B_z m_k, \gamma_l B_z m_l$, may be dropped if they are much smaller than the energy difference between these states. Hence, this approximation applies if the Zeeman term is much larger than the dipolar coupling term $\omega_{dd} \ll |B_z(\gamma_k m_k - \gamma_l m_l)|$. This is frequently the case, given the fact that for two electron spins separated by 5 nm the dipolar coupling $J_{kl}^{\parallel} \sim 800$ kHz for parallel spin orientation, which is already surpassed by a magnetic field of $B_z \sim 2.8$ Gauss.

The resulting dipolar coupling Hamiltonian further depends on the difference in energy splitting of the participating spins. If this difference is small, i.e. if we are for example dealing with two spins of the same species, we are left with the dipolar coupling Hamiltonian:

$$\begin{aligned} H_{\mathrm{dip}}^{\mathrm{homo}} &= J_{kl}^{\perp}(S_{+}^{k}S_{-}^{l} + S_{-}^{k}S_{+}^{l}) + J_{kl}^{\|}S_{z}^{k}S_{z}^{l}, \\ J_{kl}^{\|} &= \frac{J_{kl}^{\perp}}{2} = \omega_{dd}(3\cos^{2}(\Theta_{kl}) - 1) \end{aligned} \tag{2.19}$$

However, if the difference in eigenenergy splittings of the two single spin Hamiltonians is much larger than the dipolar coupling constant, which is for example the case for coupling between a nuclear and electron spin, a further approximation can be made. In this case, the secular approximation applies as well for the B term and the spin flip-flop terms can be omitted, which simplifies the dipolar coupling to an Ising-like Hamiltonian

$$H_{\mathrm{dip}}^{\mathrm{hetero}} = J_{kl}^{\|}S_{z}^{k}S_{z}^{l} \tag{2.20}$$

As soon as two spins have a finite overlap of electron density probability, an additional coupling term arises. This is for example the case if two electron spins reside within the same orbital (which leads to the zero field splitting of the NV–center), or if two organic radicals come extremely close. Additionally this can arise between a nuclear and an electron spin. In diamond this occurs for example between the nitrogen nuclei or a ^{13}C located within a few lattice positions of the NV–center and its electrons. The combination of this contact and dipolar coupling is called hyperfine coupling.

Furthermore the spin dynamics can be strongly influenced by time dependent magnetic fields, which will be discussed in the next section.

2.3.3. Rotating Wave Approximation

Time dependent fields can serve as an external control parameter for spins. For this, microwave fields of appropriate frequency ω_{mw} are used. To elucidate this matter, we add an oscillating external magnetic field to equation 2.16. This field will couple as any magnetic field via Zeeman interaction to the NV–center and the resulting Hamiltonian reads:

$$H'_{\mathrm{NV}} = DS_{z}^{2} + A_{\|}S_{z}I_{z} + \gamma B_{z}S_{z} + \gamma B_{x}\sin(\omega_{\mathrm{mw}}t)S_{x}. \tag{2.21}$$

We can assume without loss of generality that the external oscillating field will be polarized along the x-direction with strength B_x, which is often much smaller than the external static field B_z. To solve this time-dependent Hamiltonian it is transported to the *rotating frame*, i.e. we transform the coordinate system to one that rotates with the frequency ω_{mw} of the applied time dependent magnetic field. This is equivalent to the application of a unitary transformation $U = \exp(-i\omega_{\mathrm{mw}} S_z t)$. For the Hamiltonian the following relation can be found by studying the time dependent Schroedinger equation [130]:

$$\begin{aligned} H_{\mathrm{NV}}^{\mathrm{MW}} &= U^\dagger H'_{\mathrm{NV}} U + i\frac{\mathrm{d}U^\dagger}{\mathrm{dt}} U \\ &= (D - \omega_{\mathrm{mw}}) S_z^2 + A_\| S_z I_z + \gamma B_z S_z + \\ \gamma B_x & e^{(i\omega_{\mathrm{mw}} S_z t)} \sin{(\omega_{\mathrm{mw}} t)} S_x e^{(-i\omega_{\mathrm{mw}} S_z t)} \\ &= \Delta S_z^2 + A_\| S_z I_z + \omega_0 S_z + \Omega_1 S_x + \Omega_1 e^{(i2\omega_{\mathrm{mw}} S_z t)} S_x e^{(-2i\omega_{\mathrm{mw}} S_z t)}. \end{aligned} \tag{2.22}$$

where we have used the identities $\omega_0 = \gamma B_z$, $\Omega_1 = \gamma B_x/2$, $\Delta = D - \omega_{\mathrm{mw}}$ and:

$$\cos{(\omega_{mw} t)} S_x + \sin{(\omega_{mw} t)} S_y = \frac{1}{2}\left(e^{(-i\omega_{\mathrm{mw}} S_z t)} S_x e^{(-i\omega_{\mathrm{mw}} S_z t)}\right).$$

The last term in eq. 2.22 can be neglected by the *rotating wave approximation*, which is very similar to the *secular approximation* used in the previous section. In principle the fast rotating term only causes a small frequency shift and can therefore be neglected. One can split the linear polarized microwave field in two oppositely rotating circular polarized parts, while the one that is counter-rotating to the rotating frame precession with double the frequency can be neglected. Hence, we arrive at a now time independent Hamiltonian of the NV–center in the rotating frame,

$$\boxed{H_{\mathrm{NV}}^{\mathrm{mw}} = \Delta S_z^2 + A_\| S_z I_z + \omega_0 S_z + \Omega_1 S_x}, \tag{2.23}$$

which allows us to describe the spin dynamics under microwave irradiation very conveniently. For a two level system, the dynamics can be descriptively visualized by a sphere (the so called Bloch sphere), which is what we will be doing in the next subchapter. The application of microwave fields that are in resonance with the unperturbed Hamiltonian H_{NV} will now correspond to a rotation around the respective axis. Non resonant microwave fields will change both the axis and the magnitude of this rotation, and will quickly (around $\Omega_1/\Delta > 10$) not have an effect on polarized states any more.

2.3.4. Numerical Simulation of Pulse Sequences

After describing the Hamiltonians that govern the NV–center spin dynamics for magnetic coupling, we need to be able to describe their evolution in time. Usually one uses the time dependent Schroedinger equation which describes the evolution of Hilbert states. For spins however it is much more suitable to use a density matrix approach, since their dynamics are almost always subject to magnetic field noise from the environment and thus mixed states have to be used. This on the other hand means that the scope of the Hamiltonian needs to be extended to include the environment. Hence, we invoke Liouville's theorem which leads to the so called von Neumann equation. This is the equivalent of the Schroedinger equation for the density matrix:

$$i\hbar\frac{\mathrm{d}\varrho_{\mathrm{tot}}}{\mathrm{dt}} = \left[H_{\mathrm{tot}}, \varrho_{\mathrm{tot}}\right]. \tag{2.24}$$

In this equation, the Hamiltonian H_{tot} and the density matrix ϱ_{tot} include both the system under investigation, in our case the NV–center, as well as the full environment, for example the carbon spin bath. Since we are not interested in the dynamics of the environment, we can partially trace over the environment states to circumvent their explicit calculation. This leads to the Lindblad master equation for open quantum systems:

$$i\hbar\frac{\mathrm{d}\varrho}{\mathrm{dt}} = [H, \varrho] + \sum_n \frac{1}{2}\left(A_n \varrho A_n^\dagger - \left\{A_n^\dagger A_n, \varrho\right\}\right). \tag{2.25}$$

Now effects of any environment are included through so called collapse operators A_n expressed in the eigenbasis of the closed system Hamiltonian H, i.e. for a spin system like the NV–center the operators will read $A_n = \sqrt{\Gamma_n} S_{x,y,z}$, or some linear combination thereof. Here Γ_n expresses the rate of decay. It is important to note that for the validity of the equation above the secular approximation must be valid (see section 2.3.2), the interaction between the environment and the bath, which is assumed to have a much larger dimension than the system itself, must be weak, and the decay time scale of the environment must be much faster than the system dynamics. If there is no interaction with the environment, $A_n = 0$ and the Lindblad equation reduces to the regular von Neumann equation 2.24.

Since it becomes increasingly difficult to analytically solve these differential equations with larger system dimensions, one often has to resort to numerical methods. In this thesis the QuTiP [135] package implemented in python is used for this task, which readily supplies methods and classes for creating density matrices and operators as well as a strong numerical backbone for solving differential equations (differential equations solver, exponential-series solver, quantum Monte Carlo solver). Additionally it provides methods for plotting quantum states on a Bloch sphere, which was frequently used in the last section. Conveniently, the implied time evolution solver dynamically switches between the von Neumann equation for closed systems and the Lindblad master equation depending whether or not the user supplies collapse operators.

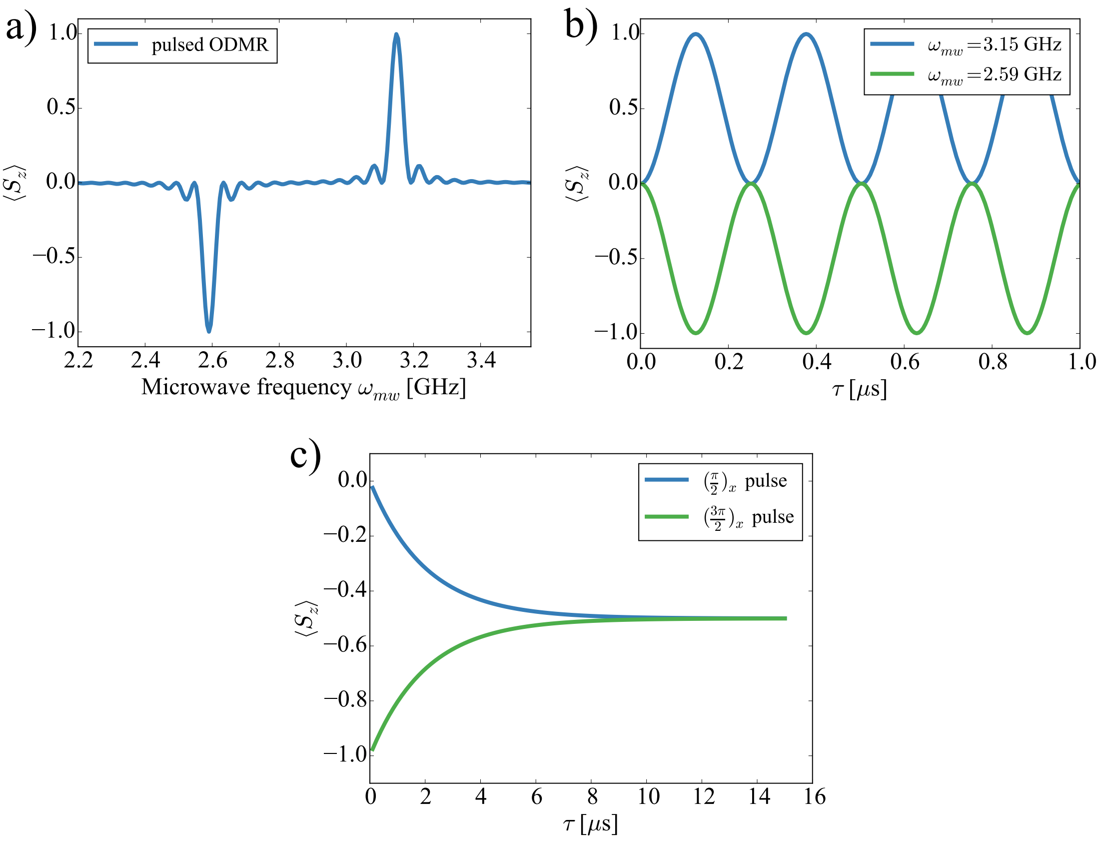

Figure 2.16.: Numerical simulations of pulse sequences. Zeeman splitting parameter is $\omega_0 = 280$ MHz, which corresponds to a magnetic field of 100 G and the microwave strength is set to $\Omega_1 = 25$ MHz. a) Simulation of a pulsed ODMR sequence on the NV–center Hamiltonian 2.23. b) Simulation of a Rabi sequence driving both transitions. A π_x–pulse has the length π/Ω_1. c) Simulation of a Hahn echo sequence with both a $(\frac{\pi}{2})_x$–pulse or a $(\frac{3\pi}{2})_x$–pulse at the end of the sequence. $T_2 = \pi\mu$s.

In graph 2.16 a few examples for the simulated outcome of various pulse sequences using this numerical package are shown. The initial state is always a pure state polarized to $|m_S = 0\rangle$, i.e.:

$$\varrho^0_{\mathrm{NV}} = \begin{pmatrix} 0 & 0 & 0 \\ 0 & 1 & 0 \\ 0 & 0 & 0 \end{pmatrix}, \tag{2.26}$$

which is the NV–center density matrix after the polarizing green laser pulse before the start of every measurement. To simulate the outcome of a measurement sequence, we evolve this density matrix under the Hamiltonian 2.16 if we let the system evolve freely, or the Hamiltonian 2.23 if microwave radiation is applied to the system for the respective evolution times. At the end of each measurement sequence with length t the result is the evolved density matrix $\varrho(t)$ and calculation of the expectation value

$$\langle S_z \rangle = Tr \left[\varrho(t) \left| 0 \right\rangle \left\langle 0 \right| \right] \tag{2.27}$$

gives the result of a fluorescence measurement with a green laser, i.e. a projection on the S_z-axis. This approach is illustrated by a simulation of $\langle S_z \rangle$ under a pulsed ODMR sequence in figure 2.16a, or a Rabi sequence in figure 2.16b.

To prevent numerical errors or excessive computational time in longer and complicated pulse sequences, one can make the approximation that microwave pulses of length τ are perfectly matched in frequency to the NV–center transitions. This implies that their effect can be modeled by unitary gates that act on the density matrix as $\varrho_\alpha = U_\alpha \varrho_0 U_\alpha^\dagger$ with rotating angle $\alpha = \Omega_1 \tau$, which has the important advantage that only two matrix multiplications have to be performed instead of multiple time evolution steps according to the Lindblad or von Neumann equation. In this way we can for example simulate a Hahn echo sequence, shown in figure 2.16c using unitary gates for $(\frac{\pi}{2})_x, \pi_x$ and $(\frac{3\pi}{2})_x$–pulses between the $|0\rangle$ and $|-1\rangle$ states:

$$U_{\pi/2} = \begin{pmatrix} 1 & 0 & 0 \\ 0 & \frac{1}{\sqrt{2}} & -\frac{1}{\sqrt{2}} \\ 0 & \frac{1}{\sqrt{2}} & \frac{1}{\sqrt{2}} \end{pmatrix}, U_\pi = \begin{pmatrix} 1 & 0 & 0 \\ 0 & 0 & -1 \\ 0 & 1 & 0 \end{pmatrix}, U_{3\pi/2} = \begin{pmatrix} 1 & 0 & 0 \\ 0 & -\frac{1}{\sqrt{2}} & -\frac{1}{\sqrt{2}} \\ 0 & \frac{1}{\sqrt{2}} & -\frac{1}{\sqrt{2}} \end{pmatrix}. \tag{2.28}$$

Additionally we have added a collapse operator $A = \sqrt{T_2^{-1}} S_x$ to the simulation which introduces decoherence from an external source.

2.4. Conclusion

In this chapter the NV–center in diamond was presented as an atomically sized sensor for magnetic fields, with sensitivities reaching single spin level. A detailed overview of the current understanding of its level structure and optical behavior was given. Consecutively, it was shown how to utilize this knowledge for the implementation of ODMR protocols, that enable it's spin properties. It was furthermore shown, how these spin properties in principle allow to deduce magnetic fields in the NV–center environment. Finally, the theoretical background needed to perform simulations of these properties was covered, which can be used for a better understanding of measurement results.

3. Experimental Setup & Techniques

The next chapter is concerned with the experimental instrument used throughout this thesis. All data shown within this thesis was acquired on this scanning-probe ODMR setup situated in a cryogenic and ultra high vacuum environment. Features and extensions that were important for the scientific progress made throughout this thesis are highlighted in the first two sections. The final section demonstrates the capabilities of the system by measuring the magnetic field from an atomically sharp tip in a scanning probe approach.

3.1. Experimental Setup

The experimental apparatus is a combined scanning probe and optical spectroscopy setup, specifically developed with the aim to perform high stability measurements with atomic resolution. This entails using high resolution non-contact atomic force microscopy based on electrical readout from tuning forks and a confocal microscope, that works close to the resolution limit set by diffraction in order to resolve single NV–centers. Combination of the above techniques is becoming more common, as for example described in ref. [99], but performing these experiments with molecular resolution sets technically challenging demands. A key point is for example, that the environment is mechanically stable on the sub-nm level over a timescale of hours also in terms of molecular diffusion and reactivity. This can only be guaranteed by placing the microscopy unit inside a cryostat that is cooled to liquid helium temperatures ($T \approx 4.2$ K) in an ultra high vacuum ($p \leq 10^{-9}$ mbar) environment.

A schematic overview of the instrument used for the work presented in this thesis is shown in figure 3.1. The development and technical characteristics of this setup have been described in detail previously [136, 137] and here a short overview, highlighting the important features, is given.

The setup can be divided into four major parts, which are the AFM unit (red), instruments to generate microwaves for spin manipulation (blue), the optical setup (black) for spin readout and stages for sample diamonds. All of these instruments are synchronized by multiple FPGAs, which both collect digitized measurement data and provide pulse timing by TTL pulses. The user can control measurements, collect data and perform in-situ analysis by a mostly self written python software, termed pi3diamond, which uses the Enthought Canopy (Version 2.1.1) package for visualization.

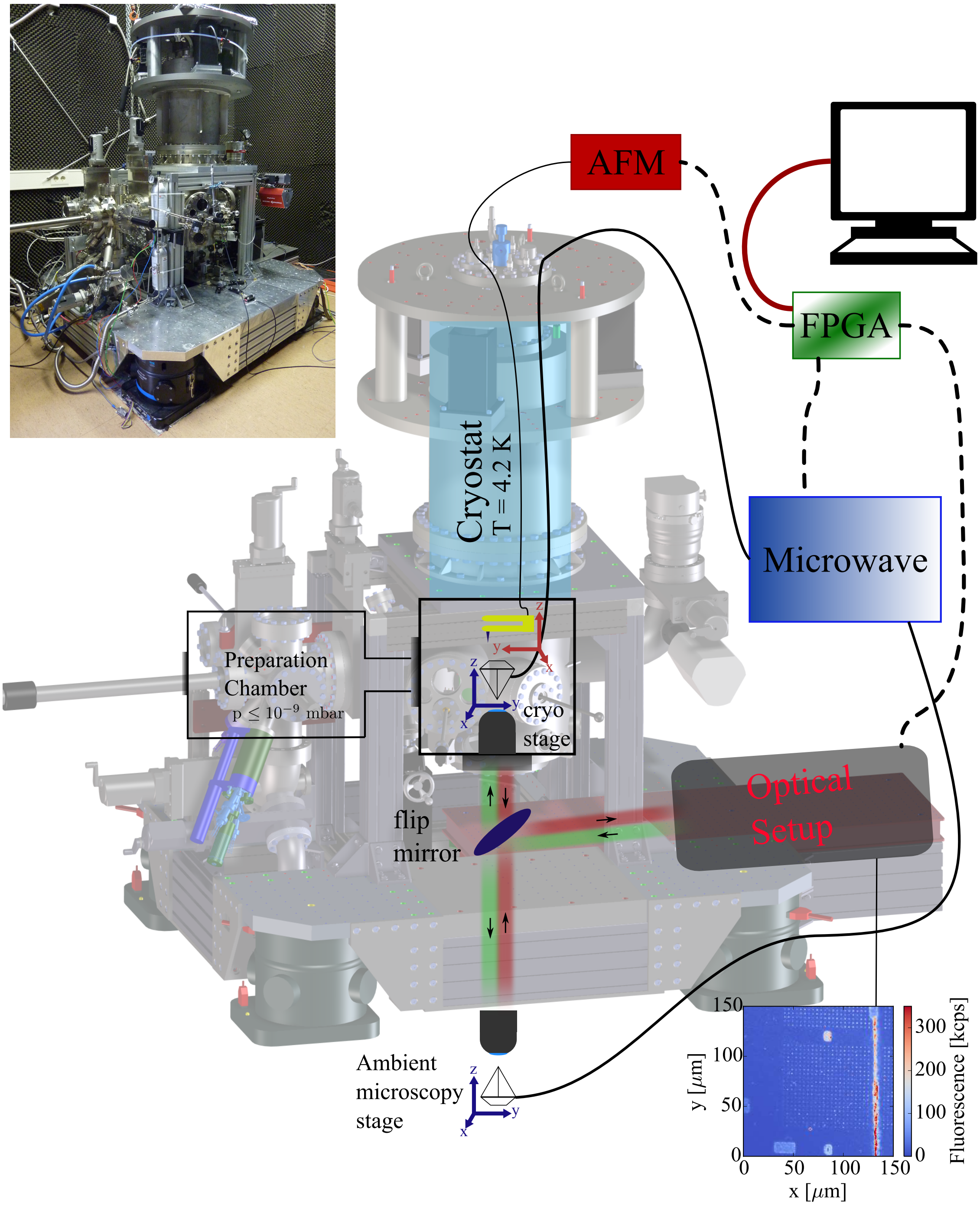

Figure 3.1.: Schematic of the experimental setup. Upper left: image of the experimental setup.

3.1.1. Atomic Force Microscope

The atomic force microscopy unit is mainly used as a precise positioning tool for target spins with respect to an NV–center under investigation. We use tuning forks in a qPlus design [138], on which tips can be glued and whose oscillations generate a current via the piezoelectric effect. These currents are usually in the pA regime and amplified by a home-built transimpedance amplifier (gain: 10^8 V/A) located inside the cryogenic measurement head. For scanning operation, the AFM control unit (Nanonis SPM-Controller, Specs Zürich) can perform both amplitude modulation (AM) or frequency modulation (FM) modes. It contains three independent feedback loops for amplitude, frequency and z-position of the tip, which are used for the respective scanning modes. The tip holder is located on an Attocube, ANPz51eXT/LT/UHV nanopositioner with 5 mm positioning range for z movement and a home-built xy piezo actuator stage with 3 mm positioning range, which allow coarse movement for in-situ tip exchange or sample approach by slip-stick motion. The fine scanning operation is performed by applying DC high voltage to a PZT piezo tube on which the tip holder is located. For combined AFM-ODMR operation, the Nanonis controller sends and receives commands via a LabView interface to the pi3diamond python software and gives pixel- and line-triggers to the FPGA for measurement synchronization.

3.1.2. Microwave Generation

For spin control, arbitrarily shaped high power (mW range) and high frequency (MHz to GHz range) electromagnetic fields need to be applied to the NV–center under investigation in the confocal spot. For this purpose, usually a gold wire of 50 µm diameter is wire bonded across a coplanar high-frequency waveguide microfabricated on a sapphire plate, on which diamond samples are located over a small aperture to provide optical access (see figure 3.3a). To provide sufficient power for spin manipulation, the wire has to be located within ≤ 200 µm to the NV–center. Pulsed high-frequency signals are generated in two different ways, depending on the application and the amount of signal control needed. For pulsed measurements on the NV–center, a LabBrick LSG-402 signal generator is connected to TTL controlled gates (Mini-Circuits ZASWA-2-50DR+). Pulses along x- or y-axes are generated by the usage of a $90°$ phase shifter (Mini-Circuits ZX10Q-2-34-S+). If other spins need to be addressed during the measurement sequence, such as in the protocol presented in section 4.2, a second high-frequency generator (Rhode & Schwarz SMIQ 3B) can be added with a power combiner to perform experiments with two frequencies. For measurements that require arbitrary shaped pulse forms, as for example the measurements in section 5.4.2, an arbitrary waveform generator (Tektronix AWG 5012B) is used. This allows generation of free configurable voltages with a 1.2 GS/s resolution. Because the bandwidth of the AWG is too low to address frequencies in the GHz regime, the frequency is mixed with a higher carrier modulation frequency in the IQ module of the SMIQ. After pulse synthesis, MW radiation is amplified by the TecDia TD-A06M20-25-F, that has a gain of $+44$ dB over a wide frequency range of $0.02 - 6.0$ GHz. A disadvantage of the setup is transmission through the cryogenic system, which introduces losses of up to -40 dB in certain frequency bands, leading to heating and spectral irregularities. The main contribution comes from impedance mismatches in sample connections.

3.1.3. Optical Setup

The optical setup is a standard NV magnetometry confocal microscope [29], that utilizes a dichroic beam splitter for 532 nm excitation and $650 - 750$ nm fluorescence readout by two avalanche photo-diodes in a Hanbury Brown and Twiss geometry for photon counting and autocorrelation measurements. The detection beam is thereby focused on a pinhole with a diameter of 100 µm, to filter out light originating outside the focal spot of the objective. To generate pulsed laser radiation from a frequency-doubled Nd:YAG laser, two acousto-optic modulators (Crystal Technologies, model 3350-192) are introduced in row into the beam path to ensure minimal photon leakage. The beam enters the measurement head in the cryostat through three viewports, which have minimal losses for the used wavelengths. To generate spatially resolved sample images, the laser beam is scanned outside the cryostat with a mirror on a tip/tilt piezo platform (PI S-330.8) prior to entering the high NA objective, situated at low temperature. Inside the cryostat the sample is placed on a home-built piezo actuator stage with a travel range of 5 mm in the xy-plane and 15 mm in z-direction to position regions of interest in the objective focus and in-situ sample transfer. For the purpose of characterizing a large number of NV–centers, we can additionally switch to a confocal scanner unit that is situated at ambient conditions with a flip mirror as indicated in figure 3.1. For this, a copy of the sample holder design [136] was made to facilitate fast sample exchange with the cryogenic setup and mounted on a closed loop piezo stage (Piezosystem Jena T-404-01D) with a 3D scanning range of 150 µm.

Optical collection efficiency is an important parameter for NV magnetometry, since the number of collected photons directly translates to magnetic field sensitivity (eq. 2.14). For this reason objectives with a high numerical aperture are required if high sensitivities

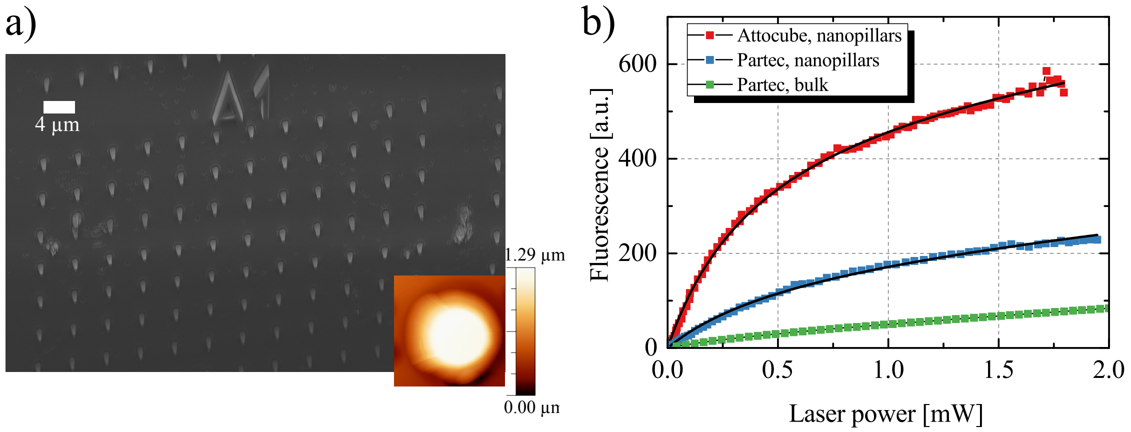

Figure 3.2.: Increasing NV–center fluorescence collection efficiency at low temperatures. a) SEM image of a nanofabricated diamond nanopillar membrane. Inset shows an ambient AFM scan over a single pillar. b) Comparison of bulk and nanopillar diamond samples and Partec or Attocube microscope objectives at low temperature on the same NV–center.

are to be achieved. This usually limits the working distance to sub-mm values and, at least for the setup used here, prevents placing the objective outside the cryogenic environment. Unfortunately, cooling has detrimental effects on collection efficiency in most of the commercially-available high NA objectives. This is due to the fact that they are not optimized for low temperature operation and mechanical shifts due to differences in thermal expansion coefficients cause sometimes irreversible degradation of their optical properties. For this reason, with the initially used Partec 50x0.82 objective it was difficult to resolve single NV–centers at low temperature, with saturation fluorescence countrates only reaching 30 kcps comparable to the background fluorescence. However, a significant improvement was achieved by using nano-engineered cylindrical diamond waveguides with an apex diameter of 400 nm and a base diameter of 700 nm [139], referred to as nanopillars, in which shallow NV–centers are implanted. A SEM and AFM image of such a sample is shown in figure 3.2a. This geometry and the high refractive index of diamond lead to a focusing effect of the red fluorescence and thus a significant increase of the number of collected photons. This is shown in figure 3.2b, where the fluorescence saturation of an NV–center in a bulk diamond is compared with an NV–center in a nanopillar. An increase in collected photons of almost an order of magnitude is achieved. Due to this, all measurements presented in this thesis are acquired using such diamond nanopillars. Another important improvement is gained by using an objective specifically engineered for usage at low temperatures and UHV (attocube LT-APO/VISIR/0.82). In this objective, only few lenses are used and thermal expansion is accounted for. This not only increases collected photons by a factor of 3 as shown in figure 3.2b, but also allows the objective to be thermally cycled multiple times.

3.1.4. Preparation Chamber

The setup geometry also entails a preparation stage in UHV environment attached to the main chamber. The design incorporates a linear magnetic transfer rod to a sample storage stage inside the main chamber, where samples and AFM tips can be transferred to the measurement head in-situ within a matter of minutes. This allows for a sample transfer from the ambient stage to the cryogenic stage within an hour, including the time to pump the transfer chamber from ambient pressure to UHV. Within the preparation chamber, there are capabilities to deposit atoms or molecules upon the diamond surface from a heated Knudsen cell evaporator, monitor their growth rates by a quartz crystal microbalance or anneal the samples at moderate temperatures ($\leq 200°$C). These capabilities can be used to perform epitaxial sample growth in-situ, or to clean the diamond surface.

3.2. Vector Magnetic Field

To perform magnetometry measurements at various field strengths on different NV–centers, one needs to control the orientation and magnitude of the magnetic field. Since NV–centers can be oriented in one of four possible crystal directions and field components perpendicular to the NV–center symmetry axis induce spin state mixing and quench fluorescence, one needs to be able to precisely align the magnetic field direction to the NV–center axis. A widely used approach is to mount a permanent magnet onto an xyz-positioner with a high enough range, which allows to align fields up to 0.7 T [140]. This geometry is used for magnetic field alignment at the ambient stage.

However, such a system is more difficult to realize within the cryogenic measurement head, as it would require another set of piezo actuators and the respective cabling. For this reason we implemented a home-built current controlled 3D electromagnet depicted in figure 3.3a.

The magnet consists of three coils that point towards the sample position and can each be addressed separately. In order to let each coil correspond to an axis in a Cartesian coordinate system, they are oriented roughly perpendicular, as far as the space inside the measurement head permits. For maximum field generation per least current, the coils consist of ~ 5000 loops of OFHC copper wire with a diameter of 0.1 mm, shielded by

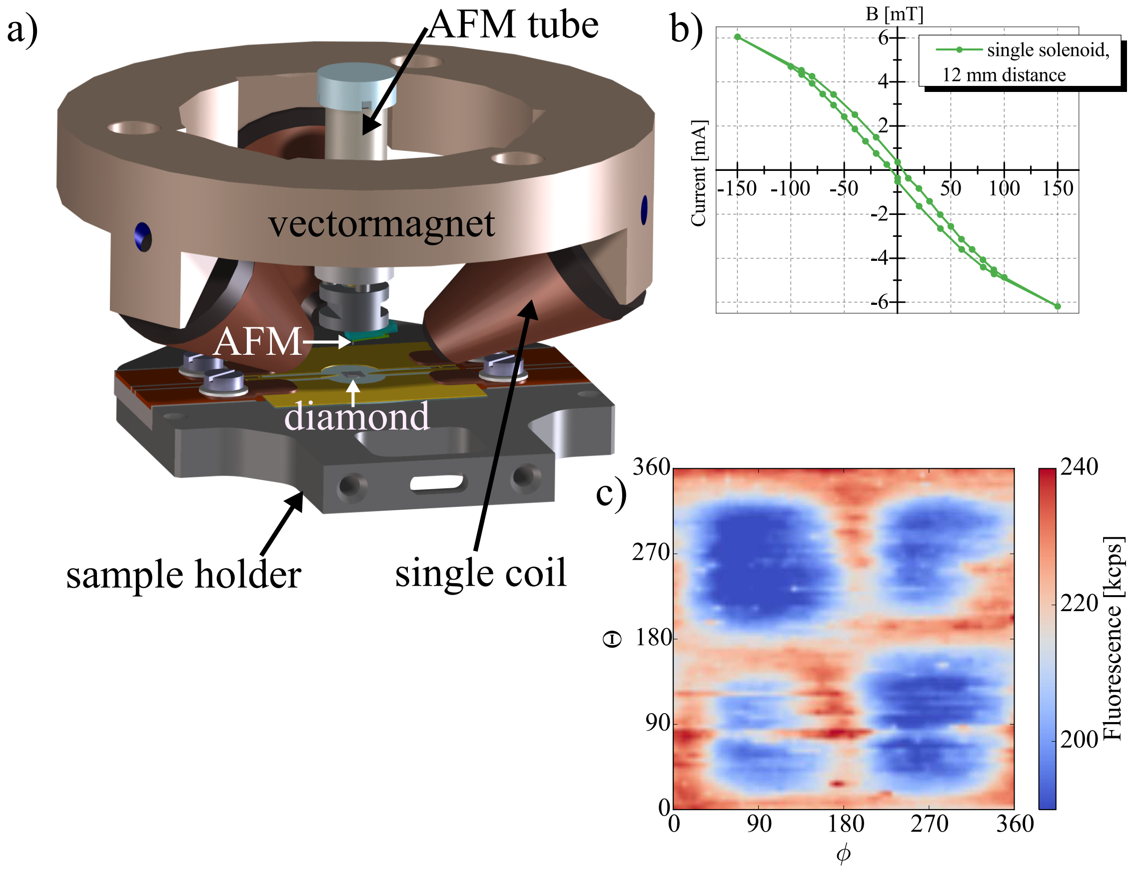

Figure 3.3.: Working principle of a 3D vector-magnet with a maximum field strength of 10 mT suitable for low temperature and UHV operation. a) Design sketch with AFM unit and diamond sample holder. b) Hysteresis of a single solenoid, measured at $T = 4.2$ K at a distance of 12 mm of the solenoid apex. c) Fluorescence magnetometry with a single NV–center inside the cryostat, which shows a clear directional dependency.

0.01 mm of polymer insulation, which results in a resistance of $\sim 3\ \Omega$ per coil at 4.2 K. This resistance allows to apply currents up to 200 mA on each coil without heating the measurement head significantly. In figure 3.3b, a hysteresis measurement of a single coil immersed in liquid helium is shown. A further increase of the magnetic field strength is gained by introducing a ferromagnetic core to the coils. For material consideration the decisive parameter is not permeability, but a high remanent magnetization, since most ferromagnetic materials saturate at the H-fields generated here. This makes soft iron an ideal choice and figure 3.3b shows that its remanent magnetization is barely reached by the applied currents. A further magnetic field amplification is generated by mounting the three coils on an iron holder. All material and geometric parameters, such as diameter of used wire or orientation of coils and holder, were successively optimized for maximum magnetic field output with finite element method simulations.

Indeed, the maximum magnetic field is around ~ 10 mT for arbitrary directions, as measured by alignment of the field with each of the possible NV directions in a (100) diamond. The alignment can be found by a fluorescence scan as shown in figure 3.3c. In this measurement, we conduct a full directional sweep of a $\boldsymbol{B}$-field vector of fixed total magnitude composed from all three coils, which can be expressed by the polar angle ϕ and azimuth angle θ in spherical coordinates. The fluorescence intensity depends on the magnetic field component perpendicular to the NV defect axis [141], where off axis fields of 10 mT reduce photoluminescence by 10%. The scan in figure 3.2c thus reveals, that the NV–center is likely to be oriented along $\theta = 0°, 180°, 360°$ (all equivalent). This orientation shows a splitting of 10 mT in pulsed ODMR spectroscopy. A much sharper fluorescence maximum and thus a better alignment can be achieved when increasing the magnetic field strength.

Increasing the magnetic field strength to values in the 100 mT region is important for many future experiments, for example nanoscale NMR. Improvements on the current design could entail to use a superconducting wire, which would allow for much higher current densities. This requires however a rewiring of the cryostat with superconducting leads.

3.3. Combined ODMR–AFM Operation

A simultaneous operation of scanning probe microscopy and ODMR readout of the NV–center spin state enables spatially encoded magnetic resonance measurements and thus exploits the full potential of the NV–center as an atomic sized magnetic field sensor. To this end the user faces the task of localizing the NV–center with an atomically sharp tip or vice versa. In the presented setup, this amounts to positioning the AFM tip into the focal spot of the fixed objective. In this section, we show the incremental procedure for co-localization and present an application as we determine the magnetic gradient from commercial magnetic force microscopy (MFM) tips.

3.3.1. Co-localization of Tip and NV–center

The stepwise alignment of an AFM tip apex and NV–center is depicted in figure 3.4.

After tip and sample are loaded, windows in the heat shield and on the vacuum chamber allow to image the inside of the measurement head using a CCD camera and telescope, a system that is also key for in situ sample and tip exchange. In the image shown in figure 3.4a, one can distinguish the confocal spot (green) and the position where the AFM tip is glued to the tuning fork (red). Thus the tip is positioned in the confocal spot by optical alignment.

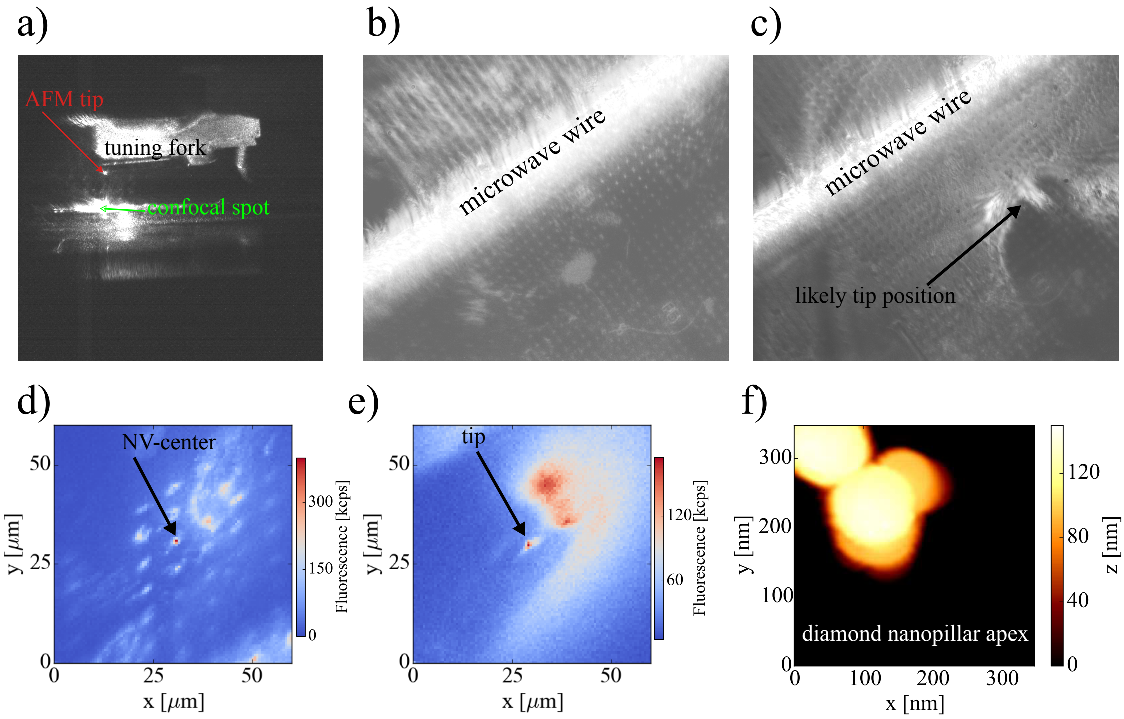

Figure 3.4.: Localization procedure of a single NV–center with an AFM tip. a) is a telescope image from the side, b)+c) are widefield images with side illumination, d)+e) are confocal images, f) is an AFM scan of the pillar containing the NV–center under investigation.

Since the above described procedure provides only a rough alignment, especially in the axis perpendicular to the image plane, we implemented a widefield setup that can be inserted into the optical path prior the first window of the vacuum chamber. Here, an image of the whole objective focal plane is acquired by a CCD camera, while the sample is illuminated with a high power white LED through the side-window. The resulting image of a nanopillar sample with far retracted tip can be seen in figure 3.4b. We can clearly distinguish the highly fluorescent gold wire and single diamond nanopillars, which are very beneficial for co-localization. Once the AFM tip is in contact with the sample, we can distinguish features from the tip in the image 3.4c. With most tips, however, it is difficult to clearly localize their exact positions and only a rough alignment is possible.

As a next step, we switch from the widefield illumination to the confocal setup and illuminate the sample through the objective with the laser. At this point an NV–center is selected from the confocal image (figure 3.3.1d), while the tip is retracted. Afterwards, we move the sample out of the focal plane and bring the tip in the previous focus position of the NV–center as shown in figure 3.3.1e. Most of the times the AFM tip and especially the adhesive epoxy with which it is glued to the tuning fork will be highly fluorescent. This allows to identify its position and to place it at the xy-position of the NV–center.

Finally, the sample is moved back in focus and an AFM scan of the diamond surface is conducted. Although the scan range of the AFM scanner unit is rather limited compared to the pillar dimensions, we can place the AFM on the apex of the nanopillar that contains the preselected NV–center. This is a crucial step and one can damage both the tip an diamond pillar structure if not careful.

3.3.2. Scanning Magnetic Samples

An application of combined ODMR and AFM operation is to measure nanoscale magnetic gradients. A high magnetic field gradient directly corresponds to spatial resolution in magnetic resonance imaging and is therefore an important step for future applications of MRI on single molecules. The strategy for NV magnetometry should be to generate the highest gradients at lowest total field strength possible, to minimize off-axis components that quench the NV–center properties during a scan. These characteristics are provided by AFM tips that have a thin coating of a ferromagnetic material [142]. Here we use a commercially available Bruker MESP silicon tip, which is coated with a thin layer of cobalt/chrome, typically used in magnetic force microscopy.

The measurement principle to characterize the magnetic field gradient from such a tip is shown in figure 3.5a. The magnetic tip is scanned on a grid over the NV–center, and in each pixel we perform a measurement to determine the magnetic field strength. After the alignment procedure described above, the tip is approached on the apex of the nanopillar, which provokes a fluorescence quench in contact, indicating that the magnetic tip is close to the NV–center with a high total magnetic field strength. Thus, we retract the tip from the surface by 40 nm, where quenching effects become negligible. A possible measurement to determine the magnetic field is shown in figure 3.5b. Here we performed a pulsed ODMR measurement in each pixel for a fixed frequency of 2.75 GHz. This produces an image of an isometric magnetic field line. The circular shape of this line fits to what is expected from a cone shaped magnetic tip [143].

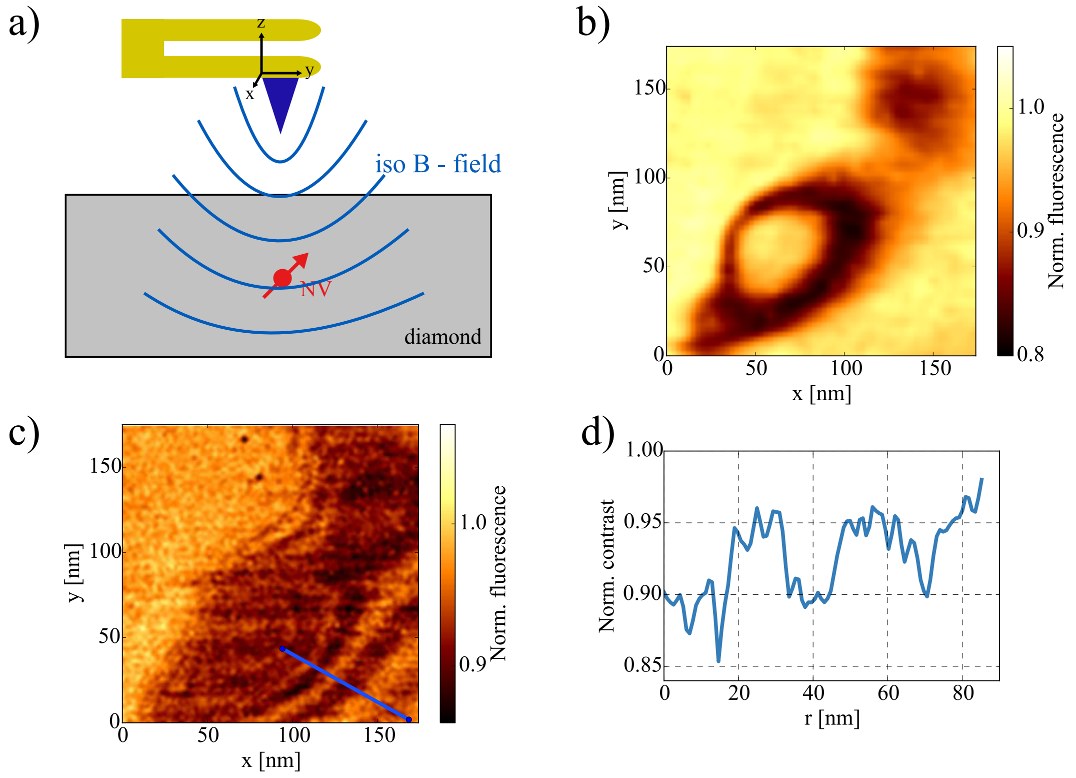

Figure 3.5.: Scanning a silicon cantilever coated with Co/Cr (Bruker MESP) at low temperature. a) Measurement principle for magnetic field gradient determination, b) pulsed ODMR scan, c) FID scan, d) line plot along the blue line indicated in c).

Another approach is to perform an FID measurement with a fixed free evolution period at each pixel position. This generates oscillations dependent on the detuning with respect to chosen frequency influenced by the tip magnetic field. The measurement outcome is shown in figure 3.5c. The oscillations are only visible in a certain region of the scan, since detunings become too high otherwise. A line plot of the data along the blue line in figure 3.5c reveals an oscillation period of 40 nm, which corresponds to a magnetic field gradient of 4.5 µT/nm given that the free evolution time used was $\tau = 200$ ns.

This demonstrates our capabilities to characterize magnetic fields generated from AFM tips and to use their gradients for scanning probe experiments. The magnetic field gradient measured from these commercial tips, however, is rather low. If we consider for example spatially resolving two single NV–centers, this gradient allows to spectrally resolve them if they have 8 nm separation and an ODMR linewidth of 1 MHz (compare figure 2.7). For higher spatial resolution, the magnetic gradient needs to be increased.

4. Detection of External Spin Systems

After describing the experimental setup and basics of NV–magnetometry, the present chapter describes how these methods can be applied to study magnetization dynamics of systems external to the diamond lattice. First, it is explained how to detect iron-containing ferritin protein nanomagnets. Initially we study ensembles comprised of many ferritin molecules and then demonstrate how to detect individual proteins with a magnetic moment of $\sim 300\ \mu_{\mathrm{B}}$. This demonstrates the capabilities of the experimental system, since the low temperature capability is essential for this experiment. These results have been published in refs. [136, 144].

In the second section, we present experiments that significantly increase the magnetic moment sensitivity and perform measurements on isolated single spins that are located on the diamond surface. The used method is very similar to the DEER technique from EPR spectroscopy and instead of passively detecting spin noise, we will actively manipulate target spins.

4.1. Magnetization Dynamics of Ferritin Molecules

Iron constitutes a very important element for many processes within our bodies, where it for example facilitates oxygen transport from the lungs to parts where it is needed. Because iron is toxic, since it is among other things able to generate free radicals, a mechanism for safe storage is needed, which is provided by a protein called ferritin.

Ferritin is a globular arrangement of 24 protein subunits that form a self-assembled nanocage. As the name suggests, the biological relevance of this protein cage is the intake, release and transport of iron in a non-toxic form within the bodies of many living organisms ranging from plants to mammals [145]. As depicted in figure 4.1, the protein subunits form a shell, that is ~ 12 nm in diameter and can be filled with up to ~ 4500 iron atoms for the considered case (horse spleen ferritin). Iron is stored in the form of hydrous ferric oxide with varying phosphate content and can be released through up to eight ion channels [146]. Since the ionic iron atoms possess a magnetic moment, ferritin can be investigated using magnetometry.

At lower temperatures (between 240 K [147] and 500 K [148]) the individual Fe^{3+} spins are coupled antiferromagnetically. This results in a reduced total magnetic moment of $\sim 300\ \mu_\mathrm{B}$ due to incomplete compensation of all spin magnetic moments caused by imperfections in the two spin sublattices. Hence a single ferritin molecule can be considered to have a single magnetic moment with uniaxial anisotropy. Due to the size of this magnetic domain, the barrier of anisotropy with energy E_a is comparable to the thermal energy even below 300 K, which results in frequent flips of the magnetic moment as is typical for molecular nanomagnets.

The magnetic moment randomly switches its orientation with a characteristic timescale $T_{1,f}$. This timescale is influenced by energy from the environment and thus depends on the temperature as described by the Neél-Arrhenius equation:

$$T_{1,f} = \tau_0 \cdot \exp\left(\frac{E_a}{k_B T}\right). \tag{4.1}$$

Here τ_0 is the inverse attempt frequency. In literature this value can be found to have a rather large spread of $10^{-13} - 10^{-9}$ s, measured with a range of techniques as for example Mössbauer spectroscopy [149], susceptibility measurements [150] or EPR [151]. We will choose a value of $2 \cdot 10^{-11}$, which does not have a huge influence on fits to experimental data. The anisotropy barrier energy E_a depends on volume, shape and strain of the particle and its measurement can thus give information about these quantities [149].

The switching behavior is visualized in the experimental sketch in figure 4.1. As the temperature increases, magnetic moment reversals will create random telegraph noise with a higher frequency $1/T_{1,f}$. Depending on how the measurement specific spectral filter function overlaps with the magnetic moment fluctuation spectrum, one will either measure a net magnetic moment if the fluctuations are much slower, or a constant averaged net magnetic moment as in a paramagnet if they are much faster than the measurement time. This is also referred to as superparamagnetism and the transition point in temperature between these two domains thus depends on the applied sensing technique. The spectral filter functions of NV magnetometry were discussed in detail in chapter 2.2 and depend on their specific measurement timescale. A key feature for NV magnetometry is the unique ability to change the spectral filter function via the employed measurement protocol. In the following we present how to utilize this to detect magnetic fluctuations from ferritin molecules over a wide temperature range.

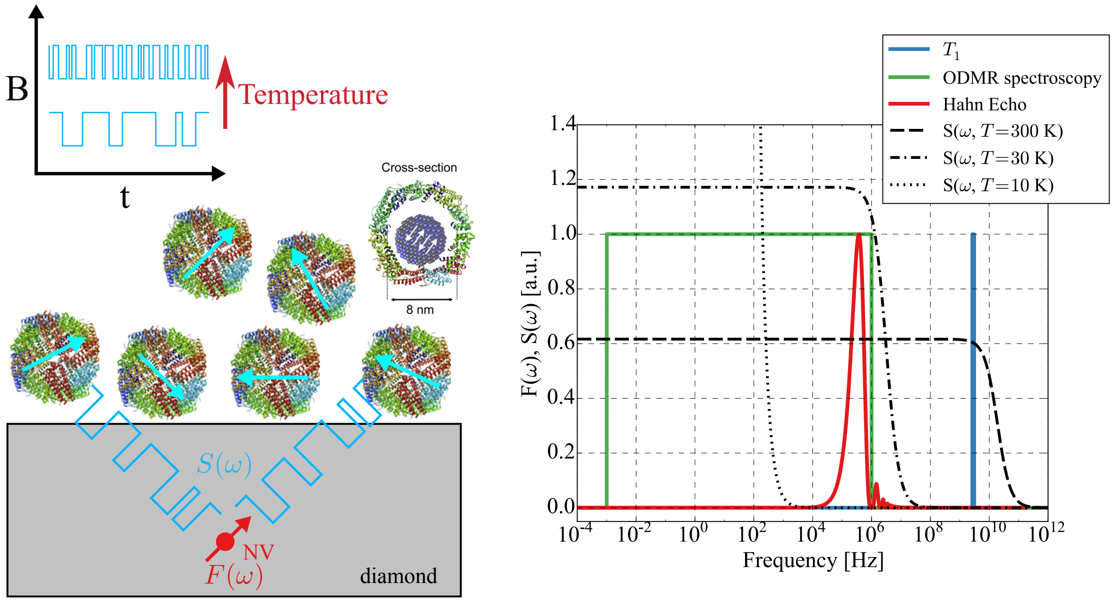

Figure 4.1.: Detection of magnetic noise from ferritin molecules. Left: sketch of the experiment. Ferritin molecules are deposited on the diamond surface and their random magnetic fluctuations are detected by coupling to the NV–center. Right: NV–center spectral filter functions for the used sensing protocol alongside the temperature-dependent magnetic noise spectrum of ferritin molecules, arbitrarily normalized.

The experimental sample geometry is sketched in figure 4.1. An NV–center containing diamond is covered with ferritin molecules, whose magnetic moments influence the NV–center spin properties. As the NV-ferritin coupling is dipolar in nature, only molecules in a limited range of about 15 nm will have a significant influence on the measurements, even if the diamond is covered with many layers of ferritin molecules. The NV–centers used here are located ~ 7 nm below the diamond surface (5 keV ^{15}N^{+} implantation) and thus only the first one or two ferritin-layers will be detected. Ferritin was dropcasted on the diamond surface from a solution of horse-spleen ferritin (Sigma-Aldrich). After a few minutes to allow for molecule adsorption, the diamond was rinsed with water and then dried under constant flow of argon gas. The surface coverage was then verified using ambient AFM.

In figure 2.15 it was already shown that the NV–center T_1, T_2 and T_2^* timescales, accessed by longitudinal relaxation, spin echo and pulsed ODMR spectroscopy measurements, are sensitive to a wide range of fluctuation frequencies. To find the additional relaxation from magnetic noise by closeby ferritin molecules, according to equation 2.4 we need to calculate the convolution of the NV–center filter functions $F(\omega)$ and the ferritin noise spectrum $S(\omega)$. The temperature dependence of the respective NV relaxation time T_i is thus:

$$T_i(T) = \left(\left(T_i^{\text{intrinsic}}\right)^{-1} + \left(\int_0^\infty S(\omega, T)F(\omega)\mathrm{d}\omega\right)^{-1}\right)^{-1}. \tag{4.2}$$

$T_i^{\text{intrinsic}}$ is the respective relaxation time without coupling to ferritin molecules.

The above mentioned filter functions and the ferritin noise spectrum at different temperatures are plotted in figure 4.1 to the right. For this the ferritin magnetic noise spectral density $S(\omega)$ can be calculated assuming an Ornstein-Uhlenbeck process as discussed in section 2.2.6 and in equation 2.13:

$$S(\omega) = \frac{\kappa^2}{\pi}\frac{T_{1,f}(T)}{1 + T_{1,f}(T)^2\omega^2}, \tag{4.3}$$

where κ is the dipolar coupling strength between the ferritin molecule and NV–center. As shown in figure 4.1, for lower temperatures the frequency cutoff of $S(\omega)$ moves to lower frequencies, while the spectral density simultaneously increases.

Filter functions for the various measurement protocols have been discussed in section 2.2. One assumption we make here is that the spectral filter function for pulsed ODMR spectroscopy, which is in principle proportional to T_2^*, is a rectangular function limited at the upper end by the π-pulse duration (500 ns) and by the total acquisition time at the lower end (1000 s).

Therefore, with decreasing temperature the ferritin noise spectrum is shifted through the various frequency windows of the respective measurement protocol which thus have distinct spectral overlaps in certain temperature regions. To measure this behavior we cool the diamond sample with the cryogenic setup (chapter 3) to $T \approx 5$ K and measure the NV–center spin properties while warming up the sample in a controlled fashion.

4.1.1. Investigation of Ferritin Ensembles

First, we probe many ferritin molecules simultaneously as it is sketched in figure 4.1 (left) by covering the diamond with many layers of ferritin. To further increase the signal pickup, experiments are conducted on densely implanted ensembles of NV–centers, with more than 100 NV–centers in the confocal measurement spot. Because ferritin molecules have different shapes from molecule to molecule, the spectral behavior has to be modified to account for this distribution of anisotropy barriers E_a. This is described by a log-normal distribution $p(E, \bar{E}_a\sigma_e)$ with the mean energy value of $\bar{E}_a = 29$ meV and a width of $\sigma_E = 0.321$ [152], which is shown in figure 4.2a.

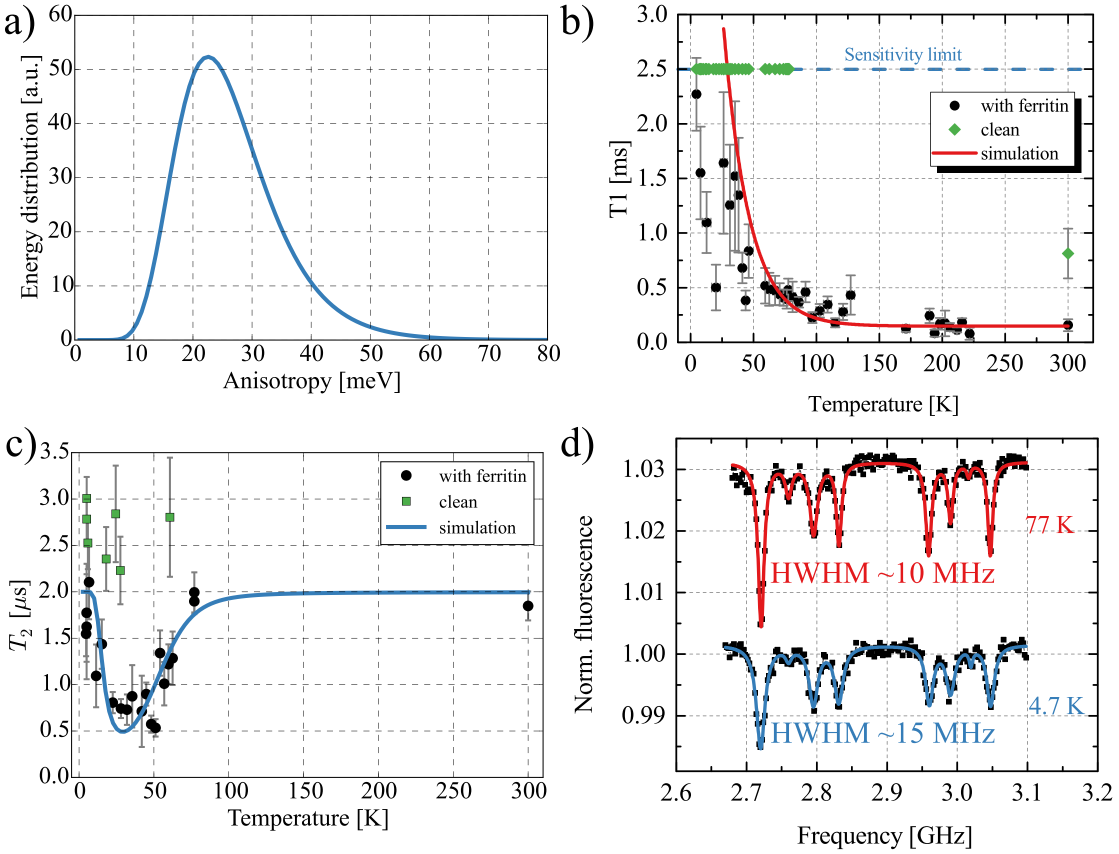

Figure 4.2.: Influence of dense ferritin molecules on an ensemble of NV–centers. a) Experimentally determined T_1 times for a freshly cleaned diamond and one coated with ferritin molecules alongside a simulation (red) with parameters $E_a = 15$ meV and $B = 786$ µT. The dashed line represents the maximum relaxation time measurable with used optical setup. b) Measurement of T_2 in the same samples. The red curve is a simulation using $E_a = 25$ meV and $B = 357$ µT. c) Comparison of ODMR spectra at 77 K and 4.7 K with linewidth of peaks indicated. d) Anisotropy energy distribution of ferritin molecules used for simulations.

In figure 4.2b, a comparison between longitudinal relaxation measurements on the same NV ensemble between the clean and ferritin coated surface is shown. For the case of a clean diamond surface the measured data shows that the ensemble T_1 increases significantly from its value of about 0.7 ms at ambient conditions to values above 2.5 ms at temperatures lower than 77 K. This was the maximum timescale detectable in our measurements due to photon leakage trough the single AOM optical setup. It has been reported in literature, that in fact the longitudinal relaxation time increases by a factor above 20 when cooling from 300 K to 4.2 K [98, 139]. The T_1-filter function at a magnetic field of ~ 5 mT used here is a Lorentzian at 2.7 GHz. As it can be seen in figure 4.1 for these high frequencies the spectral overlap is only significant at 300 K. Accordingly, T_1 drops by a factor of 5, when covering the diamond with ferritin, which has been previously observed by other groups [119, 120]. As the sample is cooled, the frequency cutoff shifts below the longitudinal relaxometry filter function and the ferritin induced relaxation vanishes. This behavior was reproduced by fitting equation 4.3 to the experimental data, depicted in red in figure 4.2b. For this a coupling strength to the NV–center of $\kappa = 22$ MHz and anisotropy barrier of $\bar{E}_a = 15$ meV were found.

In a similar fashion we investigate the influence of ferritin magnetization dynamics on the NV–center coherence time using a Hahn echo measurement. Now spin noise in the MHz region is probed and we therefore expect a different behavior. Indeed, for temperatures above 80 K, T_2 is barely affected by ferritin proteins on the diamond surface and overshadowed by the intrinsic relaxation. Yet, as the temperature is reduced further, the spectral density has a significant overlap with the Hahn echo filter function (figure 4.1) and a decrease in T_2 is observed, shown in figure 4.2c. Eventually, the frequency cutoff drops below the Hahn echo sensitivity for temperatures lower than 35 K and T_2 recovers towards the value it has for a clean surface (green data points in 4.2c). Again, this temperature dependency can be reproduced by equation 4.3, using values of $\bar{E}_a = 25$ meV and $\kappa = 10$ MHz. The discrepancy between the two parameter sets stems from the fact that for the two measurements two different samples were used, which changes ferritin composition. Nonetheless, E_a and κ lie in the range of values reported in literature [153].

Additional insight is gained when comparing the linewidth of pulsed ODMR spectra from the NV–center ensemble at different temperatures in figure 4.2d. Since the pulsed ODMR filter function is influenced by even lower frequencies, at temperatures above ~ 50 K the spin dynamics are as fast, that they effectively average out during a pulsed ODMR measurement. For this reason, the ODMR linewidth is not affected by ferritin spin noise above these temperatures, an effect often referred to as motional narrowing. However, when comparing the ODMR spectra at 77 K and 4.7 K in figure 4.2d, an increase in linewidth from ~ 10 MHz to ~ 15 MHz is observed. At these low temperatures, ferritin spin dynamics are completely blocked and each individual molecule induces a different magnetic field at the NV–center position. Thus, the spectrum is a sum of all these individual magnetic field contributions and the linewidth of 15 MHz corresponds to an induced magnetic field variation of 0.5 mT. This result fits to what was determined from T_1 and T_2 measurements and also to what can be expected from a dipolar coupling to a magnetic moment of 300 μT in 7 nm distance to the NV–center.

4.1.2. Sensing Few Proteins

Apart from the ability to access a wide frequency range using different spectroscopy protocols, we have the possibility to use single NV–centers instead of ensembles, which can couple to only few ferritin molecules. To achieve single ferritin spectroscopy, we reduce the surface coverage of ferritin molecules to a sub-monolayer, which is accomplished by lowering the molecule concentration in the dropcasted solution. AFM investigations on the prepared diamond sample confirm this, since we are able to resolve single ferritin molecules, shown in figure 4.3a. Additionally a different diamond with lower NV–center density is used, shown with confocal microscopy in figure 4.3a. The sample contains individually addressable NV–centers that couple to only a very low number of ferritin molecules. To monitor the coupling, we study the same 35 NV–centers before and after deposition at ambient conditions and find a reduction in T_1 for around 50% of them. These NV–centers are suspected to couple to ferritin molecules and are selected for further investigations at low temperature.

Temperature dependent Hahn echo spectroscopy on these NV–centers was conducted and a representative T_2 vs. temperature curve is shown in figure 4.3b. In contrast to the ensemble measurements, we now encounter several distinct minima in the coherence time. The occurrence of this effect correlates with the reduction in T_1 at ambient conditions and can not be observed for the NV–centers that do not show the ferritin induced T_1 reduction.

These minima can be interpreted as contributions from single ferritin molecules. In figure 4.3c, the influence of single couplings on the NV–center coherence time is modeled. For this we use the spectral noise density $S(\omega)$ from a single ferritin molecule in equation 4.3 instead of the ensemble distribution. Applying this model to the measurement data, we find that these features can be well described. For example, the spectrum shown in figure 4.3b can be reproduced by a coupling to two molecules with $E_a = 45$ meV, $\kappa * \gamma = 54$ µT (dip at 47 K) and $E_a = 60$ meV and $\kappa * \gamma = 36$ µT (dip at 62 K). Hence the low surface coverage enables coupling to only a few ferritin molecules, and we can determine the anisotropy barriers of single molecules using temperature dependent spin echo spectroscopy.

This is also confirmed by pulsed ODMR spectroscopy. We compare ODMR spectra at 77 K and 4 K and find that most spectra are unaffected in lineshape (figure 4.3d). However, for roughly 20% of the monitored NV–centers, significant broadening at low temperatures occurs (figure 4.3e). This can be explained by the difference in anisotropy barriers of individual ferritin proteins. For anisotropy barriers $E_a > 15$ meV, ferritin

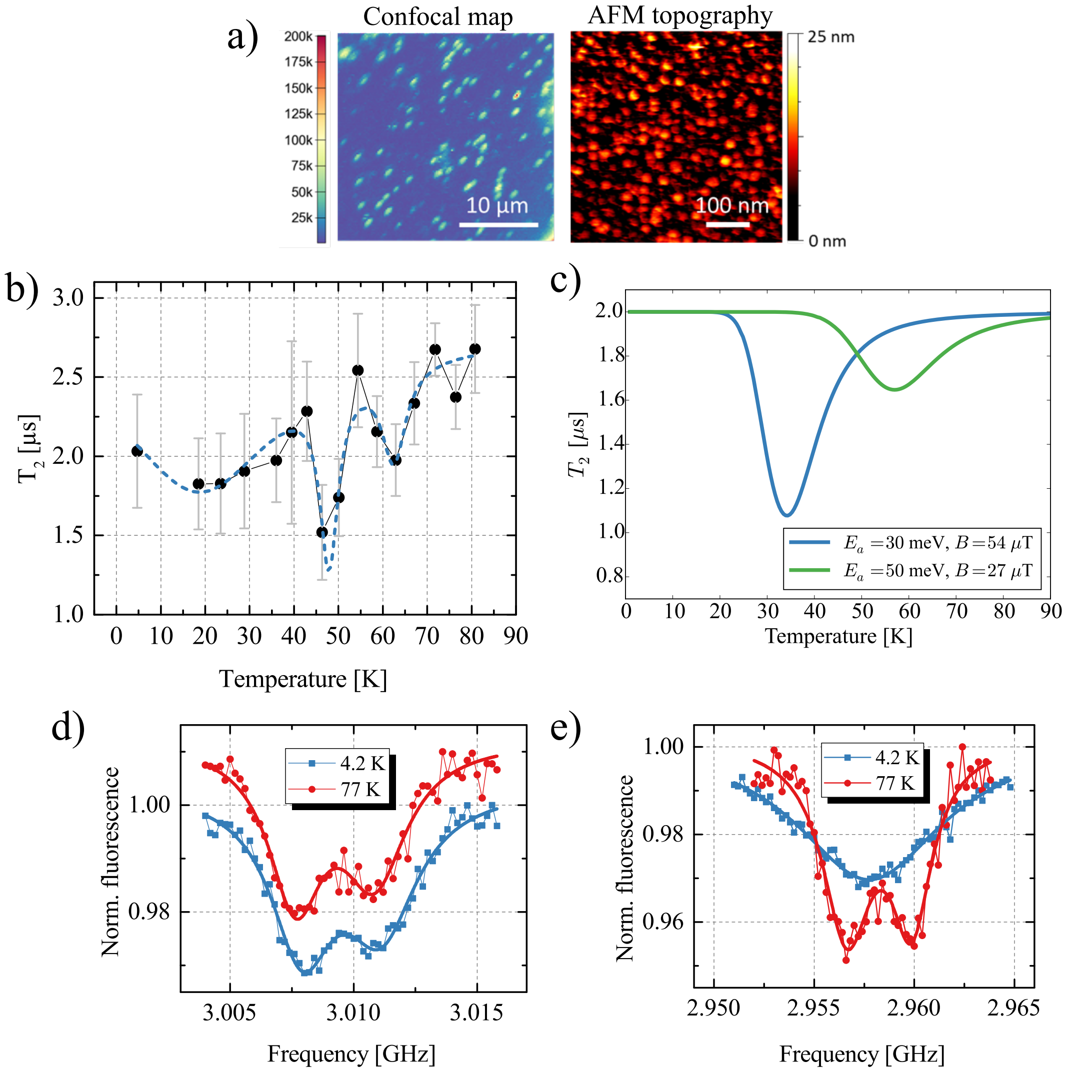

Figure 4.3.: Influence of isolated ferritin molecules on single of NV–centers. a) Fluorescence map of diamond, bright spots are single NV–centers. AFM topography of the sample surface in the same area, revealing single ferritin molecules. b) Representative T_2 measurement of a single NV exhibiting distinct drops in coherence. c) Simulation of decoherence behavior of coupling to a single ferritin molecule. d)+e) ODMR spectra of different NV–centers at different temperatures. Roughly $1/5$ of all investigated NV–centers showed low temperature broadening of the spectra.

spin dynamics are fully blocked at 4.2 Kelvin and thus the spectrum is randomly shifted according to the orientation of magnetic moment in the coupled ferritin nucleus. This shift is much lower here than for the ensemble broadening (~ 5 MHz). This stems from the fact that a deeper NV–center implantation was used and is fully consistent with the coupling strength determined from spin echo spectroscopy. If the anisotropy barrier is lower than 15 meV, however, spin dynamics are not blocked at 4.2 K and the ODMR lineshape is significantly broadened. This behavior can be reproduced with the introduced model and is also consistent with the expected spread of anisotropy barriers in horse-spleen ferritin.

4.1.3. Summary

In conclusion, we demonstrated the ability to sense magnetic noise in a wide frequency range form GHz frequencies to down the sub-Hz regime using different ODMR protocols, which outperforms most other measurement techniques. The presented results for anisotropy barriers are consistent with what was measured with a range of different techniques, like ESR or Mössbauer spectroscopy. Importantly, we also established how to detect the magnetic signal from only very few of these molecules, which opens up the way for investigations of individual proteins. This was enabled through the low temperature capabilities and high stability of the experimental setup. However, it is difficult to estimate the number of spins from the shown experiments or to control the external magnetic moment because we passively detect magnetic noise. Due to its very high sensitivity, NV magnetometry has the capability to sense systems with much smaller magnetic moments, such as single spins. To achieve this, an extension to the measurement technique, like for example a combination of ODMR and scanning probe microscopy or more sophisticated measurement protocols can be helpful. For this purpose we introduce a modification of the presented measurement protocols, which can be applied to sense single electronic spins on the diamond surface in the next section.

4.2. Increasing the Sensitivity: Surface Dangling Bonds

Engineering a system that is comprised of only a few spins with some level of control is one goal of modern physics. Such a coupled quantum system could be used for applications in modern quantum physics, like quantum information processing, quantum computing or quantum sensing. The demonstrated large bandwidth of NV magnetometry allows to detect Larmor frequencies of nuclear spins in the kHz regime (see also section 2.2.6). It can be beneficial however to detect electron spins instead, because they possess a magnetic moment that is a factor $m_p/m_e \sim 2000$ higher. This for example results in a larger coupling distance to the NV–center compared to nuclear spins and facilitates the active manipulation using microwaves, for which an order of magnitude less power density is required compared to nuclear spins. However, Larmor frequencies of electronic spins are often too high $(100-1000$ MHz) to fall within the frequency bandwidth of spin echo spectroscopy. In the following it is described how we can significantly extend the sensitivity compared to the detection of a magnetic moment with $\sim 300\ \mu_B$ as presented in the last section, to essentially detecting few electronic spins external to the diamond. To this end, active manipulation of these external spins is utilized, a technique similar to the well established double electron electron resonance (DEER) in EPR. In this section, spins from adsorbed radicals or dangling bonds, regularly found on an oxygen terminated diamond (100) surface are investigated. This is illustrated in figure 4.4a.

4.2.1. NV-DEER Spectroscopy

DEER schemes were introduced in EPR to detect couplings between electronic spins [154]. For the previously introduced Hahn echo spectroscopy, a π-pulse was inserted into the FID sequence to refocus the phase acquired from magnetic sources which results in a significantly enhanced coherence time. The DEER sequence extends this concept, separating specifically chosen dipolar interactions from all other couplings. The way this is achieved is to selectively allow phase accumulation from dipolar coupled spins by addressing them with an additional microwave channel, tuned to coherently manipulate them. Double resonance techniques are nowadays widely applied in pulsed EPR, most prominently to study distance dependent couplings in proteins for biological processes. Such an EPR measurement will be shown in chapter 5.2.

NV-DEER spectroscopy is realized by properly timing an additional π-pulse that acts on the external spins within the NV spin echo sequence. This pulse sequence is depicted in figure 4.4b. The π-pulse on the external spins reverses their S_z-component, which also inverts the sign of phase picked up by the NV–center from coupling to this spin. If this pulse is concurrent with the NV π-pulse as in figure 4.4b the phase sensitivity of the NV–center is reverted simultaneously, illustrated by the regions shaded in red. The result is that phase accumulation is permitted *exclusively* for the addressed spins, while other couplings are still canceled out by the effect of the spin echo sequence. The accumulated phase from the addressed spins will then result in a measurable change of the NV–center spin state. In principle, this is similar to the passive detection schemes used in the last section, however we now specifically tailor the magnetic field from external magnetic moments to generate noise at precisely the frequency the sequence is sensitive to. In this sense, NV-DEER can also be understood as a (quantum) lock-in technique. From now on we use the term DEER for the sequence applied on the NV–center, unless it is stated otherwise.

The DEER sequence allows to map the spectrum of the external spins onto the observation value S_z of the NV–center when the frequency of the π-pulse in the external spin channel is swept. Whenever a transition in the external spin system occurs, a decrease in NV fluorescence is induced. In contrast, for EPR DEER spectroscopy one monitors spin echo of one spin species as a magnetic response in a microwave cavity, while manipulating another spin species.

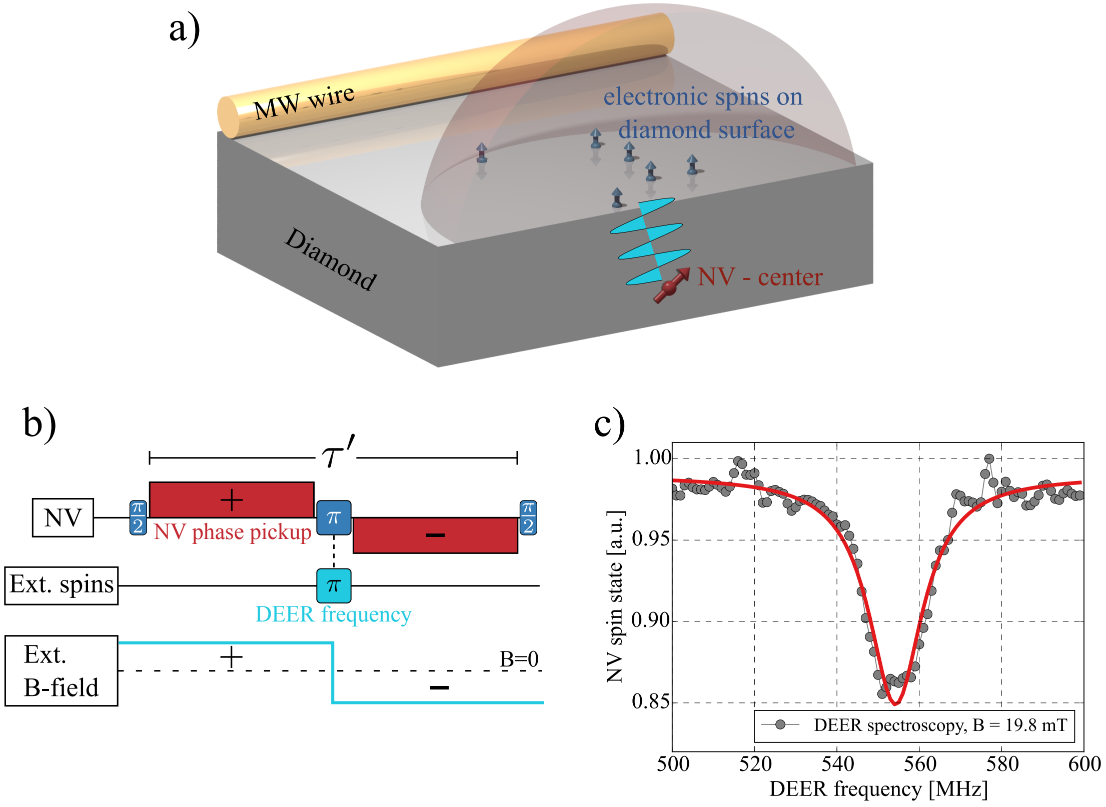

Figure 4.4.: Principles of DEER spectroscopy. a) The NV–center in diamond is influenced by electronic spins in a certain sensing region (red sphere). b) DEER spectroscopy sequence. An additional microwave channel flips external spins. Red depicts the sign of phase picked up by the NV–center. c) DEER spectroscopy measurement where the frequency of the ext. spin channel is swept on a system as it is depicted in a).

Not every external spin system can be detected using this technique. One important limitation to DEER is that the external spin does not randomly change its orientation during the measurement sequence. This means that its longitudinal relaxation time is larger than the measurement time $\tau' < T_1$. This prevents for example the detection of strongly coupled spin baths and requires sample spins to be somewhat separated, such that the bath-influence on T_1 is not dominant. DEER spectroscopy was successfully employed to detect spins within the diamond lattice, mainly nitrogen defects [155] or other NV–centers [156] where this condition is often naturally met. Obviously, it is desirable to detect couplings to spins external to the diamond lattice as well. Here it has to be noted, however, that the limit to the maximum accessible distance is set by the NV–center coherence time T_2. Since during the free evolution period τ', dipolar couplings with frequency ω_{dd} are imprinted as a phase on the NV–center coherent state, the total evolution time must be at least comparable to this timescale. In other words only couplings that fulfill the condition $1/\tau' > \omega_{dd}$ are visible. This topic will be addressed in chapter 5.4.1 in more detail. A limiting factor is, that as soon as NV–centers come in close proximity to the diamond surface (≤ 5 nm) their coherence time decreases significantly. This results in a trade-off between proximity to external spins/diamond surface and the sensing radius.

The result of such a DEER spectroscopy measurement using shallow NV–centers within ~ 7 nm to the diamond surface on a freshly acid boiled diamond at ambient conditions is shown in figure 4.4c. A single Lorentzian dip is visible at a frequency that matches the transition expected for a $S = 1/2$ free electron system with a g-factor of 2. Interestingly, this signal can be observed on roughly 25% of shallow NV–centers on an acid cleaned diamond. Up to date, the origin of such a signal is not fully understood. It has been shown, that another acid-cleaning cycle or coating the surface with polymers can remove these spins or change their positions [1, 41] and that the signal originates from the diamond surface [157, 158]. One possible origin is that the spin signal stems from electrons in dangling bonds in the top two carbon atom layers. In the remainder of this section we demonstrate how DEER spectroscopy can be used to coherently manipulate these spins and extract information about their environment.

Acquiring a DEER spectrum as in figure 4.4c is the starting point for further investigations. For the acquisition of this spectrum the length of the π-pulse on the surface spins has to be guessed. After the frequency of a resonance is determined, the length can be calibrated by recording Rabi oscillations of the external surface spins. For this purpose, the excitation frequency on the external spin channel is fixed and the length of the applied microwave pulse τ is swept. The sequence is depicted in figure 4.5. Depending on

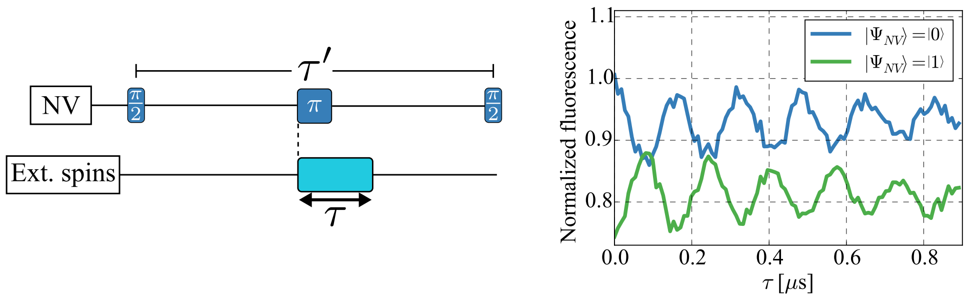

Figure 4.5.: DEER Rabi measurement. Driving the surface electron spin with varying time as depicted in the scheme (left) reveals Rabi oscillations (right), which are imprinted on the NV–center spin state via dipolar coupling.

whether the NV is prepared in the $m_S = 1$ or $m_S = 0$ state one observes complementary oscillations, shown in blue and green. A decrease of contrast is visible after several oscillations on a µs timescale for the investigated surface electron spin system. This length suggests the ability to coherently control the spin system within the measurement timescale and is an indication of the relatively weak interaction strength of the addressed spin with its environment.

It is important to note that the simultaneous application of microwave radiation, as it is depicted in all schematic sequences here and in the following sections, is not possible. Due to the large frequency difference of the two microwave channels, the external spin channel electromagnetic radiation acts as an almost constant magnetic field on the NV spin. This significantly disturbs our ability to address NV spin transitions, while the external spins are manipulated. For this reason the pulses on different spin channels are actually applied sequentially, with a separation of around 12 ns to account for pulse rise times.

Another important parameter that has to be chosen without prior information for initial measurements is the total evolution time of DEER sequences, τ'. After π-pulse and frequency are calibrated, we can investigate how the measurement result is influenced by this parameter. Because the total evolution time has repercussions on how much phase is imprinted on the NV sensor spin, it strongly affects the DEER measurement contrast. This is shown in figure 4.6 for two different electron spin configurations on the diamond surface.

Here the measurement contrast shown in blue is without the application of a π-pulse on the external spins (i.e. a Hahn echo measurement), while the green curve shows measurement data for the sequence with active external spin manipulation as it is depicted

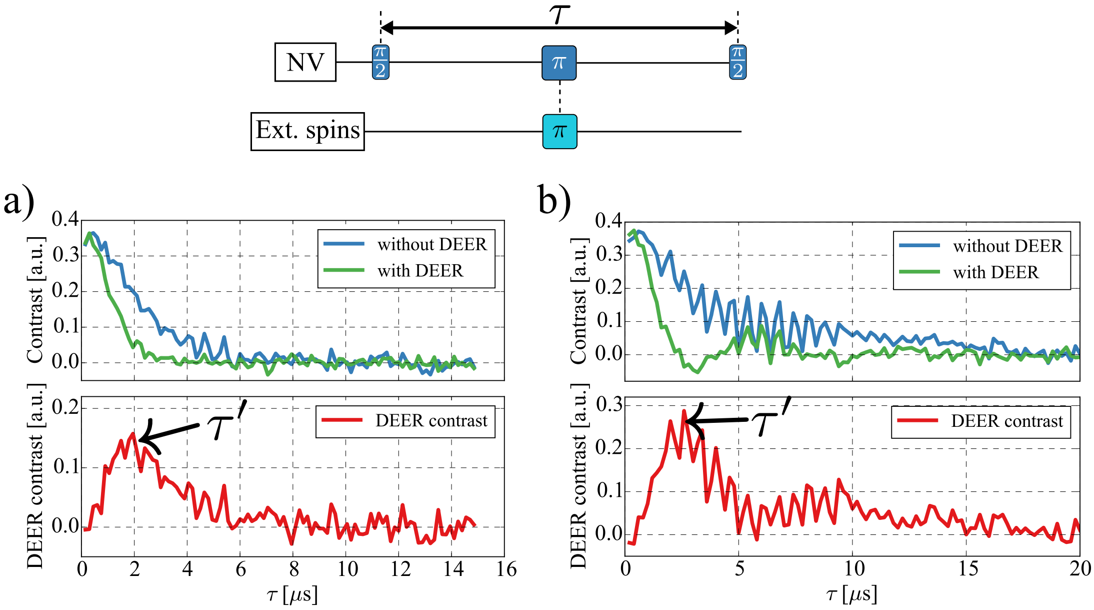

Figure 4.6.: DEER evolution measurement. a) and b) show measurements on two different NV–centers that couple to different surface spin configurations. The oscillation in b) is a sign for a distinct coupling to a single spin. All subsequent measurements are usually performed at the point of maximum contrast marked with an arrow for both cases.

in figure 4.6. Subtraction of these two measurements yields the DEER measurement contrast, shown in red below each measurement. For the surface spin system investigated in figure 4.6a, after the initial increase of DEER contrast due to more and more phase accumulation on the NV–center, the curve exhibits a monotonic decay. For one, is caused by NV–center decoherence that is also apparent in the Hahn echo measurement. However, a pure decay can be seen as an averaged contribution from many couplings (or decoherence) and is an indication for the investigation of a spin bath rather than single spins. In contrast, the measurement in figure 4.3b shows a distinct oscillation that is convoluted on the decay when the external spin channel is applied. This strongly suggests a distinct coupling which usually only stems from a single or very few spins. This topic will be further elucidated in chapter 5.4.1. Usually for any further measurements, the point of maximum DEER contrast is chosen, which is indicated in both measurements by a black arrow.

Hence, to acquire a DEER spectrum, first an initial guess for τ' is made, which is usually around the NV coherence time T_2, as well as for the π-pulse. After the point of external resonance is found in this spectrum, these values are calibrated and a spectrum is recorded once more.

The above measurements present a way to map the spin state of an external electron spin system on the readable NV–center spin population, while at the same time they provide coherent control, as long as the environment is not a strongly coupled spin bath. In principle, this extends the field of electron spin resonance from bulk samples to nanoscale sample volumes and demonstrates how the NV–center can be used to investigate samples located in close proximity to the surface above the NV sensor spin.

4.2.2. NV-DEER Correlation Spectroscopy

The NV–center coherence time T_2 can be a significant limitation to accessible couplings and timescales, as for example seen at the DEER evolution measurement in figure 4.6. Using the above introduced measurement schemes, it is not possible to access spin dynamics exceeding the NV–center coherence time, which could be for example oscillations of nuclear spin couplings imposed on the external electron spin or coupling to distant other spins. To overcome this limit, an alternative scheme can be implemented. The basic idea behind this is to measure the correlation between two separate DEER measurements, a concept that is very similar to Ramsey interferometry. In principle, this idea was already introduced for NV magnetometry without proximal electron spins for the purpose to probe long-lived evolutions of the ^{13}C spin bath [159]. Most recently such concepts were also used to successfully demonstrate high resolution spectroscopy on nuclear spins [43, 96].

The measurement sequence for acquiring the correlation of coupled electron spins is shown in figure 4.7, which was introduced by Shushkov et al. [158] to gain insight into couplings of the above described dangling bonds to other nuclear spins on the diamond surface. It consists of two consecutive DEER measurements with a variable time delay in between. During the first DEER measurement, the NV acquires a phase ϕ_1 from coupling to the surface electron spins. It should be noted that the second $\pi/2$-pulse is applied along a different axis, in order to conserve NV population according to this phase pickup during the free evolution period τ. A second DEER measurement then probes the surface spins again and results in a phase pickup ϕ_2. One can show, that the outcome of the final NV–center population readout is $\propto \sin(\phi_1)\sin(\phi_2)$ and thus effectively provides a measure for the external spin evolution during τ [158]. The most important advantage of this method is, that as the phase ϕ_1 is stored as population on the NV during the evolution period τ, the accessible measurement time is now limited by the NV T_1, which is usually orders of magnitude longer than its T_2.

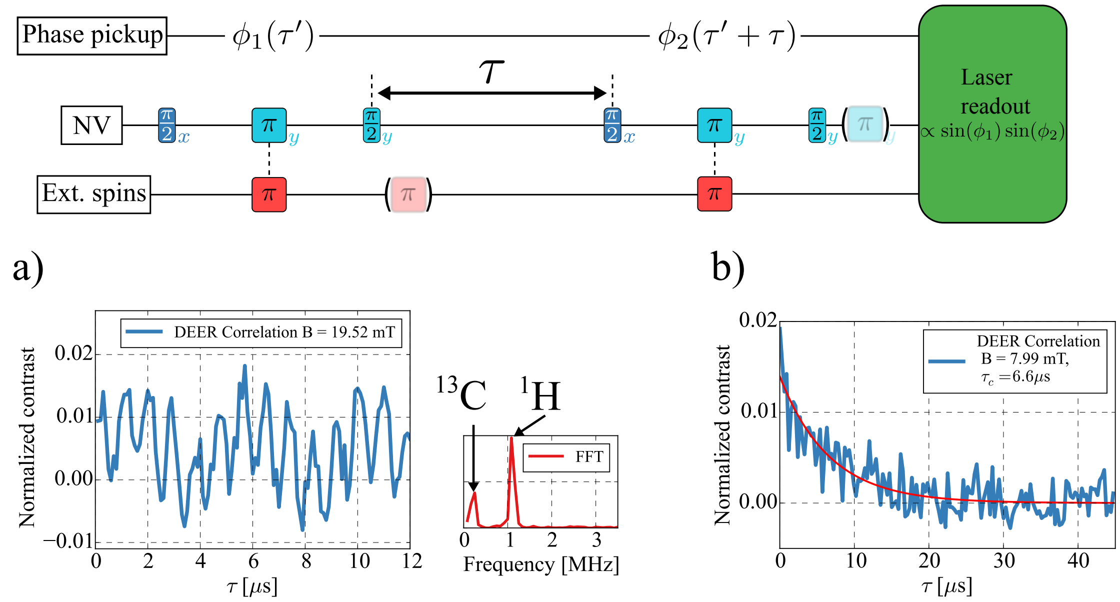

Figure 4.7.: Principle of DEER correlation spectroscopy. Two separate DEER measurements with pulses along x- and y-axes to correlate phase pickup are conducted. a) DEER correlation spectroscopy on a surface spin with long correlation time. FFT of the acquired signal to the right reveals carbon and hydrogen Larmor frequencies. b) DEER correlation spectroscopy on a different surface spin, where correlation (T_1) is much shorter.

In figure 4.7 we show two examples of possible measurement outcomes on different surface electron spin environments. For this we generate contrast by intercalating a π-pulse either on the external spin at the beginning of the free evolution period or on the NV at the end of the second DEER measurement as indicated in the pulse scheme. The measurement in figure 4.7a shows a persistent correlation amplitude, which is modulated by two frequency components as a FFT of the measurement data reveals. With the given magnetic field, these two frequencies match the Larmor precessions of nuclear ^{1}H and ^{13}C respectively. While the correlation amplitude provides a measure for the external spin T_1 time, the modulation of the signal is most likely caused by nuclear spins in the vicinity of the NV–center [159]. To determine the exact origin of the nuclear spin signal, further investigations would be necessary, like XY8-spectroscopy or correlation spectroscopy without addressing the external spins. The measured T_1 is rather high for spins that can be found on the diamond surface. In most cases, the acquired signal is similar to what is shown in figure 4.7b, where an exponential decay on a timescale of

6.6 µs is observed. This can be explained by a high surface spin density, which limits their lifetime by mutual spin flip-flops. This is also supported by the fact that only rarely a distinct coupling to a single spin can be observed in an evolution measurement as in figure 4.6b, a behavior that has proven to be consistent over many diamond samples and investigated sensors.

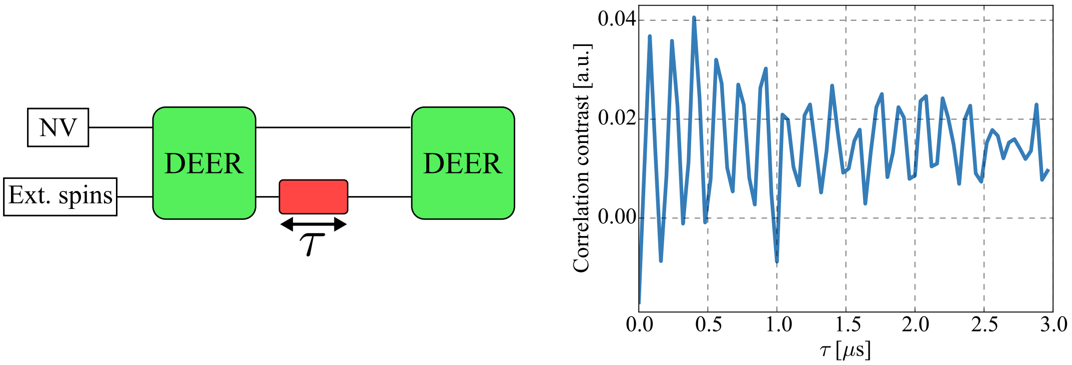

Figure 4.8.: DEER correlation Rabi measurement on surface dangling bonds. The measurement reproduces the outcome of a DEER Rabi measurement.

Coherent control and readout can be maintained on the surface spins when using the correlation readout scheme. To this end one can insert an arbitrary control sequence during the free evolution period between DEER measurements. When we insert a pulse of variable length on the surface spins, the result is a coherent Rabi oscillation, shown in figure 4.8. Hereby it is not crucial for the measurement outcome at which point in time the microwave in the external spin channel is applied. Furthermore the measurement yields precisely the same result as for the DEER Rabi measurement in figure 4.5 conducted on the spin [158].

Therefore, this control allows to insert more complex sequences in a DEER correlation measurement and to evaluate their outcome without the time limitation imposed by the NV–center decoherence time. As an example, we can perform a Hahn echo measurement on the external spin. The measurement sequence is depicted in figure 4.9a, while the result is shown in blue in the lower graph. As this scheme essentially maps the phase coherence of the external spins to a difference between ϕ_1 and ϕ_2, which is converted to a NV population difference, the measurement contrast decays with the coherence time of the surface spin state. The exponential decay constant of 0.39 µs is within the typical range found for many investigated surface spins. In fact, the coherence time never exceeded 1 µs for any surface spins that were investigated.

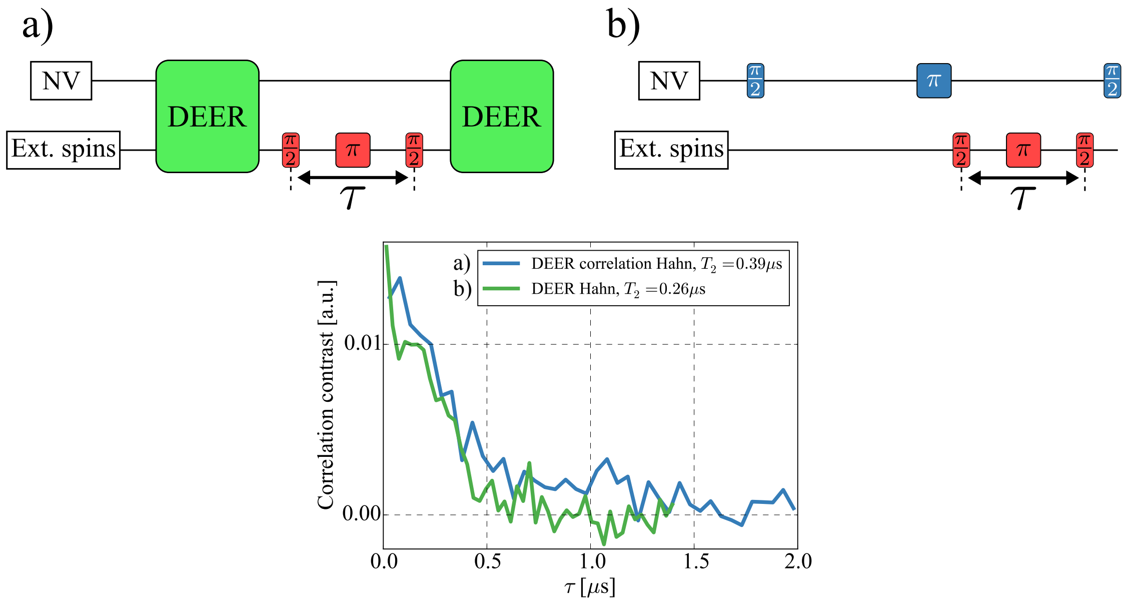

Figure 4.9.: DEER correlation Hahn measurement on surface dangling bonds. a) Measurement sequence for DEER correlation Hahn. b) Alternative measurement sequence to map external spin coherence on the NV–center spin state. Comparing both measurement shows similar results as expected.

We furthermore can compare the measured coherence decay to a more straightforward measurement where we directly insert the Hahn echo measurement within one half of the NV decoupling sequence, which should yield the same result. This scheme is depicted in figure 4.9b and the measurement outcome of 0.26 µs in green in the lower graph. While the measurements seem to be comparable at a first glance, in this case the value from the correlation measurements seems to be slightly higher than for a DEER Hahn measurement. This might be caused by pulse length instabilities, that have a larger effect in a DEER Hahn sequence, while they cancel out due to the comparison of two DEER measurements in a DEER correlation Hahn sequence. However, this comparison was not drawn for other NV–centers and thus no quantitative statement can be made.

4.2.3. Summary

In summary, the above measurements confirm that DEER correlation spectroscopy has the ability to significantly extend the measurement timescale which is available for investigations of dipolar coupled electron spins in NV magnetometry. It has to be stated that while this method allows to study spin dynamics on timescales limited by the NV–center longitudinal relaxation, it does not extend the coupling range of the NV–center.

Here the limit is the free evolution time of a single DEER sequence, which is constrained by the NV–center's coherence time. In the case of the investigated dangling bond spins, it is actually not necessary to use correlation spectroscopy most of the time because the external spin dynamics are fast. Nonetheless, this scheme can be useful when other spin systems are investigated.

Apart from proof of concept measurements, dark surface dangling bond spins have not yet been used in real applications for quantum sensing or quantum computation. One reason is the short coherence time, most likely due to other electron spins or radicals on the diamond surface. Another aspect is the inability to control or reproduce the coupling of a single NV–center to these spins. Positions of the surface spins are random and can change, for example, through a surface treatment with acid. Additionally, the stability of these spins is mostly poor. In fact, from all investigated surface dangling bond spins, none could be investigated for more than a couple of hours after which the signal changed substantially or vanished completely. Therefore, to produce a more reliable and reproducible coupling to external spins, it is necessary to find a method which allows the deliberate positioning of coupled spins close to single NV–centers.

As shown in the next chapter, spin-bearing molecules are promising candidates for such systems.

5. Nanoscale ESR on Spin Labeled Peptides

Our understanding of biological systems and processes often relies on the spatial information and conformation of relevant biomolecules, such as peptides and proteins. To acquire the loci of ultimately all atoms within a given complex is a task that can only be tackled by few techniques. Methods routinely used in this field are, for example, high resolution NMR [160] and X-ray crystallography [161], which can reach Å level of precision. Even with recent advances in these techniques [162–164], however, such measurements can only be achieved with great effort and have severe restrictions on sample properties, such as monocrystalline from or the need for a relatively large quantity of the identical molecule isomer. Nevertheless, often it is not even necessary to map the position of every atom within a molecule to accurately describe its behavior. ESR is, in this respect, a tool which can capture length-scales within relevant molecules with relative ease [165]. With this technique, the measured quantities are often spatial positions of so-called spin labels, supplying net electron spin. Their dipolar interaction with surrounding spin labels is exploited to acquire spatial and/or dynamic information on a wide variety of molecules, given an appropriate spin label attachment procedure.

Using different techniques or sensors can significantly improve the sensitivity of ESR, as for example ultra-sensitive mechanical detection [14], ultra-miniaturization of microwave resonators [166] or coupling to a superconducting micro-resonator [167]. In this chapter the use of NV magnetometry for achieving sensitivity close to the ultimate limit of ESR, a single electronic spin or molecule, on biologically relevant samples external to the diamond crystal is demonstrated. Moreover we describe how to measure the coupling in between these few molecules. The key to this approach is the DEER scheme introduced in the previous chapter.

In the present chapter we use peptides of a few nm length-scales on which spin labels can be attached to specific sites via site directed spin labeling (SDSL), and thus show distinct dipolar coupling. In the first two sections a model peptide system is presented and it is elucidated how intact structure and spin labeling process on these peptides can be confirmed using established methods. In the second section a distance distribution between these spin labels is acquired using standard EPR measurements. In the third section theory and experimental data of ESR on nanoscale samples containing very few spins in a stable environment using NV-magnetometry is reported. Finally, it is presented in the fourth section how we can gain access to the intra-peptide dipolar coupling of less than three of these molecules, using a novel resonance scheme. This paves the way towards structure determination on a single peptide level via NV magnetometry and can be interpreted as a first demonstration of quantum information protocols in spin networks comprised of biological building blocks.

The results presented in this chapter have been partly published in ref. [168].

5.1. Peptide

A synthetic, proline(P)-rich peptide is chosen as a model system, whose proline chain length can be tailored to almost any length and contains two cysteine (C) amino-acids at specific positions in the backbone. More specifically, we used the peptide H-AP$_{10}$CP$_{10}$CP$_{10}$-NH$_2$ (A: alanine), in the following referred to as P$_{10}$, and the shorter peptide H-AP$_5$CP$_5$CP$_5$-NH$_2$, in the following referred to as P$_5$, for ESR measurements. On the sidegroups of cysteines, spin labels can be attached via SDSL. This site specific labeling process serves as a key to deduce length scales of the underlying peptide via measurement of the coupling between the spin labels. Polyprolines are an often-used system for validating distance measurements via dipolar-coupling methods in ESR due to the relatively high stiffness of the proline-backbone [169, 170]. In particular the peptide under investigation here is actively used as a "molecular ruler" as well as for *in-vivo* ESR investigations of cell membranes [171].

5.1.1. Spin Labeling of Peptides

In the following approach we use the very common nitroxide spin label compound methanethiosulfonate (MTSSL) [172] as a (diamond-) external spin system, owing to the relative ease of SDSL on polyprolines and straightforward spectral interpretation [173]. Furthermore, a similar nitroxide compound has previously been studied in a single molecular fashion using NV-magnetometry [2].

As MTSSL is an amine oxide compound, its electronic $\sigma = 1/2$ spin stems from an oxygen radical with a gyromagnetic ratio of $g^{\mathrm{sl}}_{xx} = 2.008, g^{\mathrm{sl}}_{yy} = 2.006, g^{\mathrm{sl}}_{zz} = 2.002$. This electronic spin exhibits hyperfine coupling A^{sl} to a near-neighbor $^{14}\mathrm{N}$ nitrogen nucleus

$I_N = 1$ with hyperfine coupling constants of $A^{\mathrm{sl}}_{xx} \sim A^{\mathrm{sl}}_{yy} \sim 14$ MHz, $A^{\mathrm{sl}}_{zz} = 103.6$ MHz [174, 175]. The z-axis is along the N-O bond.

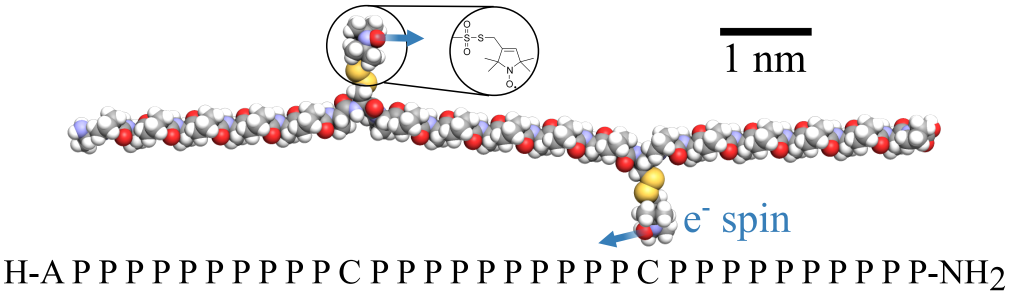

Figure 5.1.: Sketch of peptide NP$_{10}$N in a polyproline II helix with MTSSL spin labels attached to the cysteines.

To attach these electronic spins to peptides P$_{10}$ and P$_5$, a thiol specific reaction forms a covalent sulfur-sulfur bond between the MTSSL spin label end group and the thiol group of cysteine amino acids as shown in figure 5.1. For this purpose, P$_{10}$ was dissolved in 0.1 M Tris buffer (pH 7.8) with the addition of 30 mM tris(2-carboxyethyl)phosphine at a concentration of 1 mg/ml. The MTSSL spin label was also dissolved in dimethylsulfoxid (0.1 mg/µl). Subsequently the peptide (114 nmol) was incubated with MTSSL (5 µmol) at 4 °C overnight to induce the described thiol specific reaction. Afterwards, surplus MTSSL was removed from the sample solution by a polyacrylamide desalting column, which was equilibrated with 0.1 M Tris buffer (pH 7.8) before the sample was applied to the column. The fractions which contain peptides were concentrated by a Pierce protein concentrator to get rid of free spin label. The spin-labeled peptide was finally dialyzed in ZelluTrans Mini Dialyzer against water to remove the buffer. The resulting disulfide bond showed a minimum number of flexible connections between the nitroxide label and the cysteine side group. MTSSL labeled peptide P$_{10}$ will be referred to as NP$_{10}$N in the following, MTSSL labeled P$_5$ as NP$_5$N.

5.1.2. Mass Spectroscopy

To confirm the intact structure of peptide H-AP$_{10}$CP$_{10}$CP$_{10}$-NH$_2$ as shown in figure 5.1, matrix-assisted laser desorption/ionization time-of-flight (MALDI-ToF) mass spectroscopy measurements were performed to precisely determine its molecular mass. For this technique, commonly used for biological analysis, the sample molecules are embedded into a matrix of strongly light absorbing specimen. Subsequently, strong laser pulses are applied, leading to desorption of the investigated molecules. Sample molecules are then frequently ionized through generated heat in the matrix molecules and can subsequently be analyzed in a time of flight mass spectrometer. All measurements were performed on a commercial available Shimadzu AXIMA Resonance spectrometer.

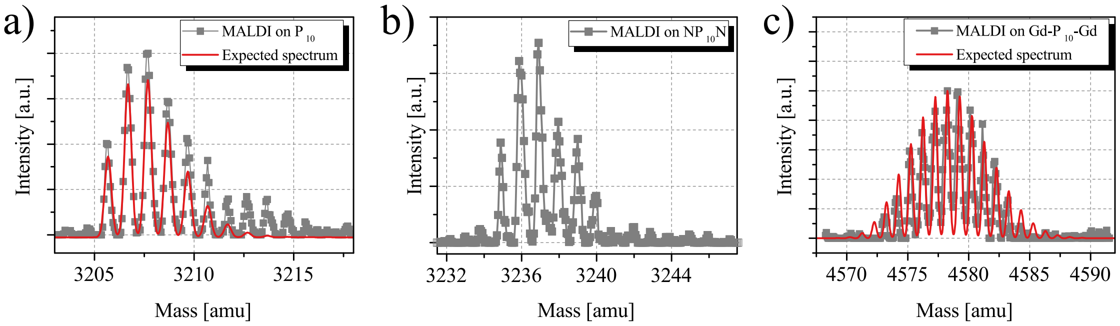

Figure 5.2.: Matrix assisted laser desorption ionization of spin labeled peptides. a) Mass spectrum of bare P_{10} peptide. b) Mass spectrum of MTSSL labeled peptide $NP_{10}N$. The spin labels are detached during the ionization process. c) Mass spectrum of Gd-DOTA labeled peptide $GdP_{10}Gd$.

To prepare the matrix, a mixture of 2,3-dihydroxybenzoic acid in tetrahydrofuran and sample peptides in water is deposited on a metallic plate. In this case the sample peptides are P_{10}, $NP_{10}N$ and $GdP_{10}Gd$, a version of P_{10} that was labeled with a different spin label, Gd-DOTA (mass formula: $C_{16}H_{25}GdN_4O_8$), for comparative reasons. The resulting mass spectra are shown in figure 5.2. The bare polyproline spectrum in figure 5.2a fits very well with the simulated mass spectrum shown in red [171]. It has to be noted that this is not necessarily the case for all samples used. In fact, samples stored several weeks in solution, even at temperatures below zero degree Celsius, only reveal fragments in mass spectroscopy, showing the need to characterize the sample prior to measurements.

Mass spectrometry on $NP_{10}N$ shows complete fragmentation of the parent molecule. In figure 5.2b the acquired spectrum is shown, which lies far below the expected 3576 amu for a doubly MTSSL labeled P_{10}. Instead, the high laser power used in MALDI experiments detaches MTSSL from peptides. The experiment was repeated several times and consistently a higher mass than the original P_{10} was found. A detrimental behavior of laser illumination on the MTSSL spin label will also be reported in section 5.3.

In contrast, the spectrum of $GdP_{10}Gd$ in figure 5.2c matches the expected result. Here the spin label tether is actually a thioether group formed by the spin label and the cysteine thiol group during attachment [171]. This prevents possible rupture of the spin label chain under laser illumination in contrast with the previous measurement.

Hence, to fully verify the successful attachment of MTSSL spin labels on the cysteine groups in P_{10}, additional investigations have to be conducted. For this purpose, non invasive EPR measurements on the prepared samples are described within the next section.

5.2. EPR Measurements on Peptides

To characterize spin properties of attached spin labels, cw and pulsed EPR measurements are performed. For EPR measurements the sample solution is introduced into a microwave cavity, tuned to a specific frequency, and a static magnetic field is swept until magnetic resonance occurs. This is a well established technique to e.g. deduce information about dynamics in biological samples or to determine distances between spin labels by identifying a distinct dipolar coupling from the average dipolar background as is illustrated in the following.

A straightforward way to characterize successful SDSL via EPR is to perform cw measurements on liquid solutions. To this end microwave radiation is applied continuously to the cavity containing the sample and absorption occurs at resonance, depending on the applied constant magnetic field B_0. The absorption leads to a detuning of the cavity and reflection of microwave radiation occurs. Detection of this reflected radiation leads to characteristic cw EPR spectra and is proportional to the first derivative of microwave absorption, which typically has a Gaussian shape (see also chapter 2.2.1). The reason for this is that the magnetic field is actually modulated around the current measurement setpoint to acquire the signal, which increases SNR significantly. The linewidth of acquired spectra depends on inhomogeneous broadening effects, which can for example be influenced by movement of spins on the measurement timescale. A spectral analysis can therefore give information about e.g. concentration (peak intensity), spin dynamics or molecular tumbling. This can be utilized to verify a successful spin label attachment to the larger peptides via monitoring rotational averaging of spins, i.e. rotation speed of the MTSSL electronic spin frame of reference within the measurement time. All cw EPR experiments were performed at the X-band frequency (~ 9 GHz) on a MiniScope5000 (Freiberg Instruments).

In figure 5.3a a measurement of free MTSSL spin label in $\mathrm{D_2O}$ solution is shown. Three peaks of similar height can be distinguished, characteristic of the hyperfine interaction with the associated nitrogen nucleus of the MTSSL molecule. Actually the measured hyperfine splitting is composed of the isotropic averaging value $g^{\mathrm{sl}}_{\mathrm{iso}} = 2.005$, $A^{\mathrm{sl}}_{\mathrm{iso}} = 1.62$ mT [174] of all three directions of hyperfine and gyromagnetic ratio contributions $g^{\mathrm{sl}}_{xx} \cdot A^{\mathrm{sl}}_{xx}$, $g^{\mathrm{sl}}_{yy} \cdot A^{\mathrm{sl}}_{yy}$, $g^{\mathrm{sl}}_{zz} \cdot A^{\mathrm{sl}}_{zz}$ as indicated in the graph. This follows from

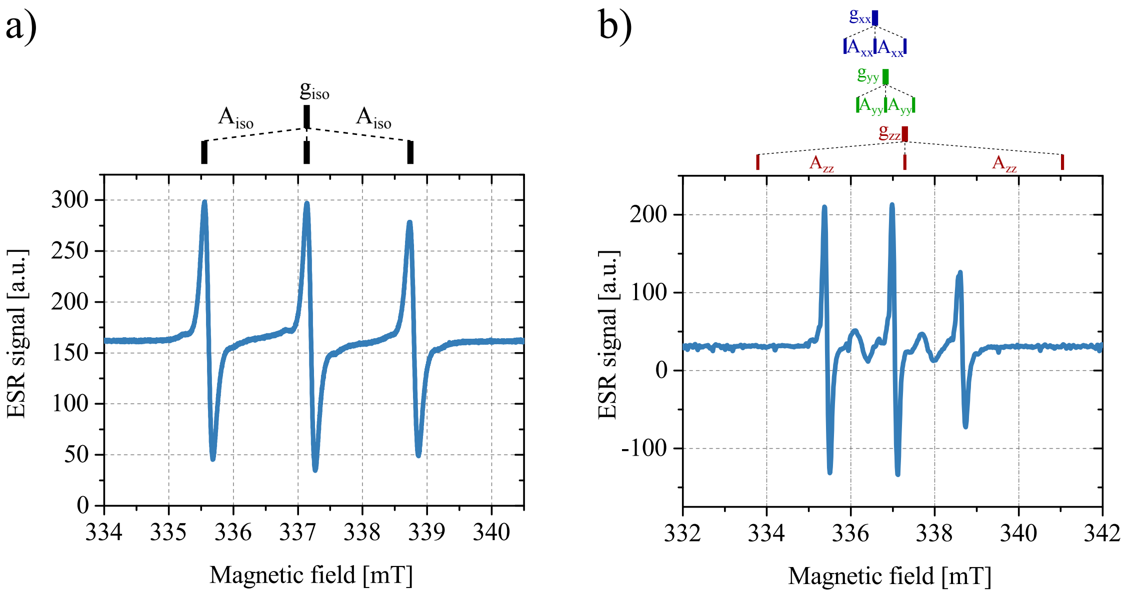

Figure 5.3.: cw ESR on MSSTL spins labels at ambient temperature in solution. a) cw ESR spectrum of 1 mM MTSSL spin label in deuterated water. Splitting is described by fully averaged isotropic values. b) cw ESR spectrum of $\sim$ 100 µM NP$_{10}$N. Successful labeling process is confirmed by signal reduction of the third hyperfine peak in comparison to a), caused by the decrease of rotational averaging of the three directional spectral contributions shown above the spectrum.

the fast rotational motion of MTSSL in water, which is in the ~ 10 ps range [176], fully averaging these contributions.

On attaching MTSSL to a much larger molecular group, the spin label molecules are more confined in space and thus a reduction in rotational and diffusional motions occurs. A second measurement is performed on the sample solution after spin labeling, which contains mostly NP$_{10}$N, shown in figure 5.3b. Here a clear reduction of the rightmost peak can be observed. In this case, the attachment of MTSSL to the peptide leads to a significant decrease of rotational motion, increasing the averaging timescale into the ns range. In turn, complete directional averaging of hyperfine and gyromagnetic ratio components, as was the case for unlabeled MTSSL, starts to break down and individual spectral contributions become apparent. If rotational averaging would decrease even further to around 1 µs (for example by incorporation the MTSSL into a solid crystal), eventually the spectrum would show the unaveraged convolution of all three hyperfine splittings as they are indicated in figure 5.3b [176]. The small contributions in between the three larger peaks here can be attributed to a small quantity of coupled MTSSL molecules, which is a side product of the incubation process.

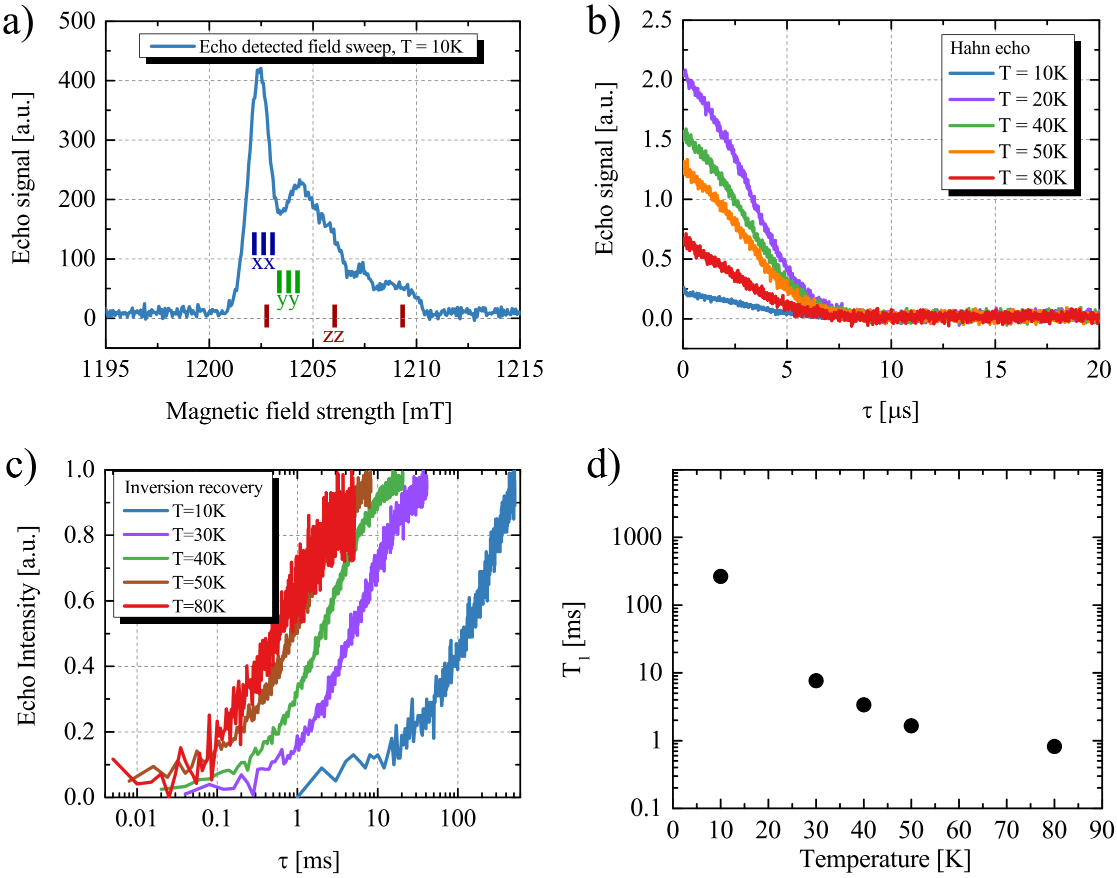

Figure 5.4.: Pulsed ESR on MTSSL labeled $NP_{10}N$ peptides at low temperatures in D_2O/gylcerol (4:1) solution. a) Echo detected field sweep at $T = 10$ K and Q-band frequency. The different hyperfine components are indicated in the graph. b) Hahn echo measurements over a temperature range, yielding the coherence time T_2 of the measured spin species. Transverse relaxation time is unaffected in the shown temperature range. c) Saturation recovery measurements, that yield the longitudinal relaxation time T_1. d) Plot of single exponential fits to the measurement data of c).

To gain access to the spin dynamic properties of MTSSL spins and determine their dipolar coupling, it is necessary to switch to pulsed EPR schemes, which suppress interactions that decrease resolution and hinder the measurement of aforementioned quantities in cw ESR. Instead of monitoring microwave absorption, as is done in a cw experiment, pulsed EPR relies on the detection of spin echoes that occur analog to what was described in chapter 2.2. Furthermore, since at room temperature the coherence time is very low for MTSSL spin labels, it is necessary to perform these experiments at lower temperatures. It is interesting to note that in contrast to NV magnetometry, EPR lacks a repolarizing mechanism and relies solely on statistical polarization described by the Maxwell-Boltzmann-statistics. For this reason the timescale on which an single measurement can be repeated is the longitudinal relaxation time T_1, after which the spins have gone back to thermal equilibrium and a measurement can be restarted. Hence it is actually favorable not to go to the lowest temperature possible, but work in an intermediate range where an acceptable time per measurement can be achieved. For MTSSL this temperature is around 50 K [177].

Pulsed EPR measurements were carried out on an ElexSys E580 spectrometer (Bruker Biospin) equipped with a CF935 helium gas flow system (Oxford Instruments) an EN5107D2 probe head (Bruker Biospin), and a 10 W microwave power solid state amplifier (HBH Microwave GmbH). The length of the π-pulse was 24 ns.

For pulsed EPR at cryogenic temperatures, 20% (vol) glycerol was added to the spin labeled samples in water to prevent crystallization of the solution, yielding samples with a concentration of ~ 100 µM. To acquire a spectrum at low temperature, an echo-detected field sweep (EDFS) is conducted, i.e. the spin echo is monitored depending on the magnitude of the magnetic field. As can be seen in figure 5.4a, the spectrum looks broader compared to the cw case. This is due to the fact that at low temperatures motional averaging effects can be neglected and that the pulsed EPR spectrometer used works at the Q-band frequency (34 GHz). This further splits the directional contributions as indicated in the graph due to the higher magnetic field used. The reason why these lines are not sharply resolved, as one might intuitively expect, is that now the small excitation pulse width results in a large spin excitation frequency band of the order $1/t_\pi \approx 50$ MHz, limiting resolution.

Subsequently spin properties of MTSSL labeled $\mathrm{NP_{10}N}$ peptides can be characterized. Hahn echo measurements with variable time delay have been carried out at various temperature depicted in figure 5.4b and fitted with single exponential decays. As can be seen the coherence time is unaffected in the measured temperature range and adapts values around $T_2 = (4.0 \pm 0.5)$ µs. This behavior is expected as the coherence time of nitroxides is dominated by proton spin flip-flops at temperatures below ~ 50 K and at the low concentrations used [178]. Additionally saturation recovery measurements were conducted (figure 5.4c) to determine $\mathrm{NP_{10}N}$ longitudinal relaxation times at various temperatures. As can be seen in figure 5.4d, T_1 strongly increases at lower temperatures. This is a behavior typical for organic radicals, as the longitudinal relaxation time is mostly governed by isotropic rotational and translational motion at room temperature [179], which is strongly suppressed at lower temperatures.

Probing distances between electron spins can be achieved by the DEER scheme as described in chapter 4.2 for NV magnetometry. In EPR, this and other closely-related measurement schemes, have often been used to measure couplings in solid state systems [180] and, more prominently, biological systems, such as spin labeled peptides similar to the ones used here [181]. In a regular EPR spectrometer, the four-pulse DEER scheme depicted in figure 5.5b is frequently used [182]. Essentially this scheme varies dipolar interaction by active manipulation of spin pairs, just as it was adapted in chapter 4.2 for measuring dipolar couplings to the NV–center. However, due to the highly sensitive microwave diodes used for detection of spin echoes in pulsed EPR spectrometers, the detection window needs to be appropriately separated from the high intensity microwave pulses used for spin manipulation. This leads to a significant detector dead-time after microwave was introduced to the cavity (~ 100 ns), which imposes limits on what timescales are accessible with a regular DEER sequence. Echo refocusing by the addition of a fourth pulse on the observer spins extends the timescale on which the pump pulse can be shifted within the sequence. This timescale directly corresponds to accessible distance, as it can be back-calculated from the known dipolar coupling behavior (equation 2.17). For nitroxides, these timescales are typically between $t_1 \approx 200$ ns and $t_2 \approx 6$ µs for deuterated samples, which corresponds to distances in the range of $2 - 8$ nm.

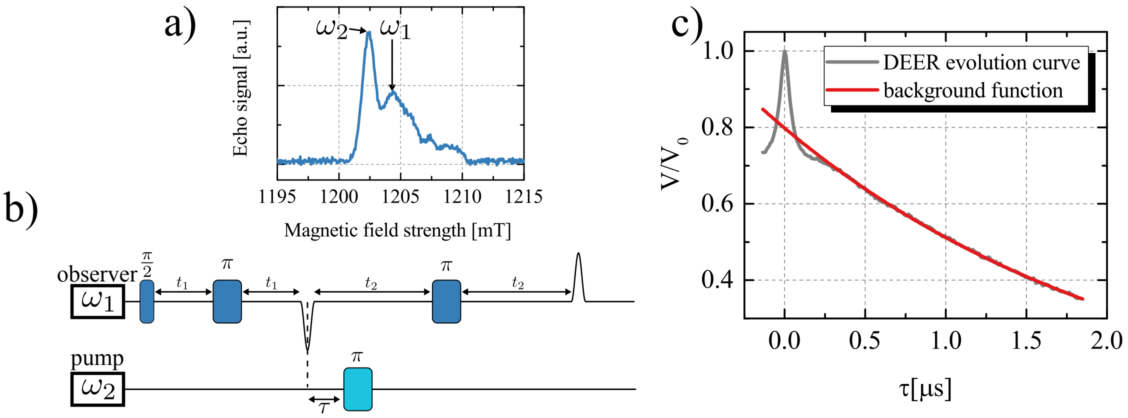

Figure 5.5.: Measurement principle of a four pulse DEER scheme. a) Pump frequency ω_2 and observer frequency ω_1 are chosen at high intensity points in the spectrum. b) Pulse scheme for a four pulse DEER measurement. c) Measurement outcome of a four pulse DEER measurement on a sample of 1 µM NP$_5$N in D$_2$O:glycerol (1:4) at $T = 20$ K. Indicated is the curve used for subtraction of the dipolar bath interaction. V$_0$ is the maximum signal.

Accordingly, four pulse DEER measurements on samples of NP_5N and $NP_{10}N$ are performed to measure the chain length of prolines between the spin labels. The pump frequency corresponds to the maximum of the MTSSL spectrum and the observer frequency is placed 75 MHz higher, as depicted in figure 5.5a, while typical pulse lengths of 32 ns for π-pulse (observer) and 12 ns for π-pulse (pump) are used. The result of such a DEER Measurement is shown in figure 5.5c. It is the superposition of an oscillation that stems from the distinct intra-peptide coupling of MTSSL pairs and a large exponential background that is caused by averaged inter-peptide dipolar coupling of the surrounding spin bath. For further analysis this background is subtracted from the dipolar evolution.

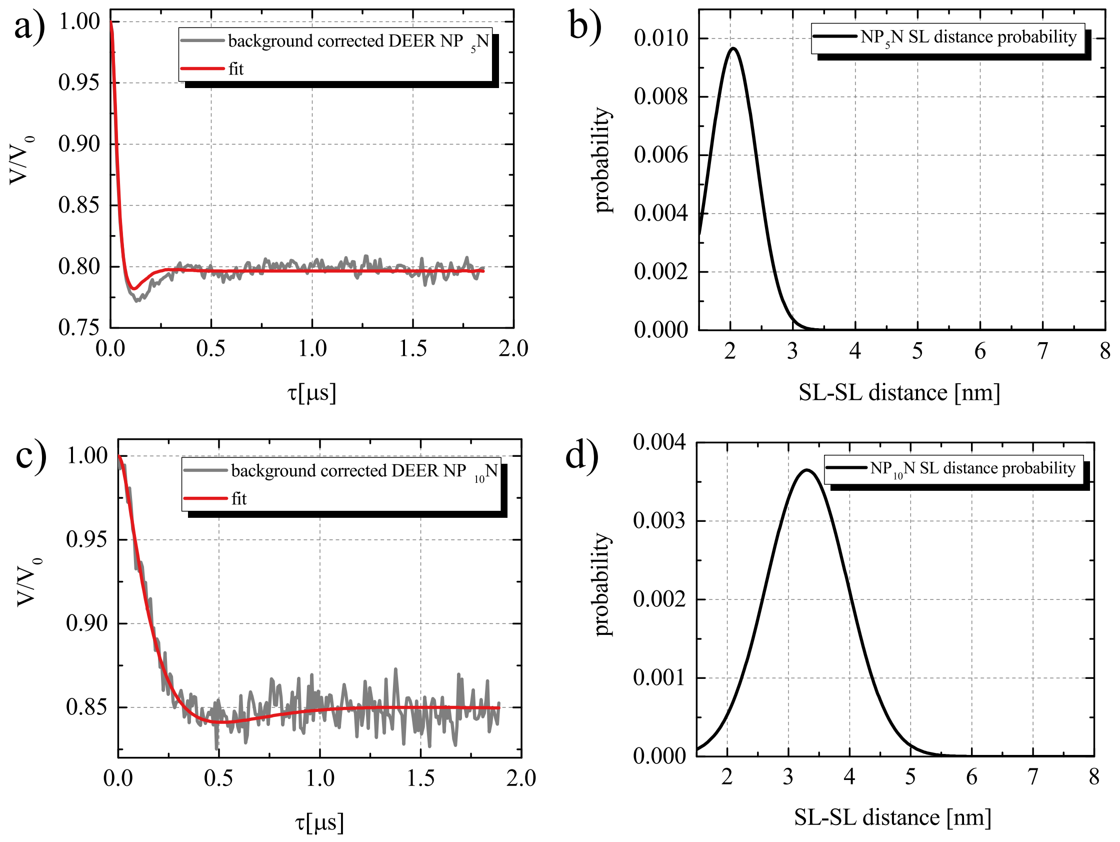

Figure 5.6.: Background corrected ESR DEER measurements and distance probability distributions of two differently spaced peptides. a) Background corrected DEER evolution of ~ 150 µM NP_5N in D_2O:glycerol (1:4) at $T = 20$ K (original data shown in fig. 5.5c) with fit. b) Calculated distance distribution probability from a). c)+d) same as a)+b), however on ~ 50 µM $NP_{10}N$ peptide sample. A shift of the distance distribution probability towards higher values is observed.

Background corrected DEER measurements of the two peptide samples are shown in figure 5.6a for NP_5N and figure 5.6c for $NP_{10}N$. To calculate the inter-spin distances from the experimental data, a Tikhonov regularization is used. For this, the simulated dipolar evolution function is fitted to the experimental data using the second derivative of the dipolar evolution as Tikhonov matrix [183]. This is conveniently achieved by using the DeerAnalysis2015 software [184].

The resulting distance distributions for NP$_{10}$N is centered around 3.3 nm, depicted in figure 5.6d. This corresponds well to what had previously been published for this peptide using gadolinium based spin labels [171]. The broad distance distribution is caused here by the fact, that these measurements average over billions of molecules and accordingly many resulting geometric conformations. It is important to note that in this case it is actually the relative flexibility of the spin label tether that causes variance in the distance distribution rather than the actual protein conformation itself. Under the assumption that a polyproline helix II will be formed, the distance between the two cysteine moieties should be around 3.1 nm, as determined by molecular dynamics simulations [169]. Accordingly, the distance distribution for NP$_5$N is centered around the lower value of 2.0 nm, as there are fewer prolines separating the two spin labels, matching simulation results. The fact that this measurement has lower noise than for the longer peptide is partly caused by higher peptide concentration, which gives a better SNR.

5.3. Nanoscale ESR

As the previous two sections demonstrated how to characterize SDSL peptides with means of nowadays standard biochemistry-techniques, the following section is dedicated to novel measurements of similar fashion using NV magnetometry. Here a decisive difference is, that NV magnetometry, instead of measuring an average over $> 10^9$ sample molecules, enables access to nanoscale sample volumes.

5.3.1. Sample Preparation

To prepare samples for a measurement which enables the determination of the dipolar coupling between MTSSL labels on a peptide and the NV-center, the two entities need to be brought into close vicinity. The maximum distance is hereby set by the coherence time of the NV-center, as described in chapter 4.2. Hence, an electronic grade diamond was used, thinned down to a thickness of 30 $\mu\mathrm{m}$, in which nitrogen ions at an energy of $5\ \mathrm{keV}$ were implanted, yielding a mean implantation depth of $7\ \mathrm{nm}$ below the diamond surface [66]. The implantation dosage is chosen in a way that allows to distinguish single NV–centers by standard confocal microscopy. Subsequently, diamond nanopillars are etched into the implanted membrane to increase optical collection efficiency [139] for later use in the cryogenic system. The diamond is then treated in a three-acid (1:1:1 H_2SO_4:HNO_3:$HClO_4$) mixture for several hours at elevated temperatures ($\sim 100°$C), to clean and oxygen-terminate the diamond surface. Afterwards the diamond is covered with $\sim 3\ \mu\mathrm{L}$ of solution that was characterized via mass spectrometry and ESR as described in the last two sections. As it turns out, previous characterization proved to be vital for a successful detection of MTSSL signal with NV magnetometry. Several attempts at detecting nitroxide spins on the diamond surface had been made, but were never successful unless the preparation procedure was monitored after each step.

After the solution is deposited, the diamond is situated in a nitrogen-rich atmosphere for around 1 hour, until all water has evaporated from its surface. This yields a surface coverage of peptide crystallites with a layer thickness of $\geq 200\ \mathrm{nm}$. The surface coverage on the edge of diamond nanopillars was verified using ambient AFM. For this a large force was applied to the Si-cantilever to remove peptides from the diamond surface in a certain area such that a subsequent measurement of the step height between the diamond surface and the peptide layer could be performed.

An optical image of a prepared sample is shown in figure 5.7 (upper left). It is apparent that the peptides do not adsorb uniformly on the diamond surface, a behavior which is known as the coffee-ring effect [185]. Here, the fact that the diamond membrane surface is nano-structured is beneficial as peptides adsorb stronger around these structures and the microwave wire, since the capillary flow in these areas is reduced. This ensures a close proximity of NV-center implanted pillars and the sample peptides.

Hence, we are expecting to study a system as depicted in the sketch of figure 5.7. A single NV–center, on average 7 nm below the diamond surface, couples to M MTSSL spin labels with different dipolar coupling strengths $\boldsymbol{F}^k$. Each MTSSL spin k is furthermore coupled to one partner MTSSL spin l located on the same peptide via the inter-peptide dipolar coupling strength $\boldsymbol{J}^{kl}$.

5.3.2. NV-DEER Spectroscopy on MTSSL Spin Labels

Numerical simulations

To be able to interpret the experimental results, we consider the possible outcome. Adding the MTSSL Hamiltonians to the basic NV Hamiltonian derived in equation 2.16 of chapter 2.3.1 we expect to study the following total Hamiltonian H for the system described above:

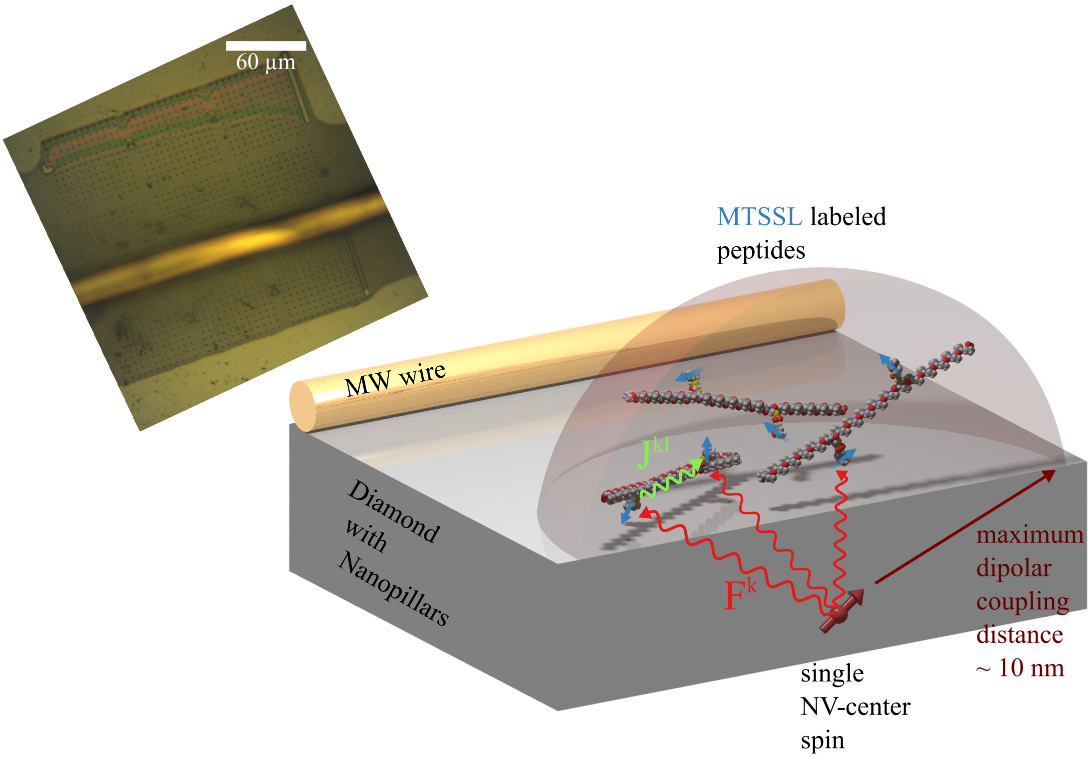

Figure 5.7.: Sketch of the experiment alongside an optical microscopy image of a prepared sample (upper left corner). Spin labeled peptides are deposited from solution on a diamond membrane with nanofabricated photonic waveguides containing NV–centers.

$$\begin{aligned}
H = H_{\mathrm{NV}} + \sum_{k}^{M} H_{\mathrm{sl}}^{k} + \sum_{k,l} H_{\mathrm{cpl}}^{kl} \\
H_{\mathrm{NV}} =& DS_z^2 + \gamma B S_z + A_{\parallel} S_z I_z + \gamma_{\mathrm{NV}} B_1 \cos\left(\delta_1 t\right) S_x \\
H_{\mathrm{sl}}^{k} =& \sum_{k} \gamma_{\mathrm{sl}} B \sigma_z^k + \boldsymbol{\sigma}^k \cdot \mathbf{A}(\theta) \cdot \boldsymbol{I}_N + \sum_{k}^{M} \gamma_{\mathrm{SL}} B_2 \cos\left(\delta_2 t\right) \sigma_x^k \\
H_{\mathrm{cpl}} =& \sum_{k} \boldsymbol{S}^k \cdot \mathbf{F}^k \cdot \boldsymbol{\sigma}^k + \sum_{kl} \boldsymbol{\sigma}^k \cdot \mathbf{J}^{kl} \cdot \boldsymbol{\sigma}^l
\end{aligned} \tag{5.1}$$

here the summation indices k, l run over all M spin labels. The spin operator of MTSSL electronic spins is denoted by $\boldsymbol{\sigma}^k = (\sigma_x^k, \sigma_y^k, \sigma_z^k), \sigma^k = 1/2$, and its ^{14}N nuclear spin with spin operator $\boldsymbol{I}_N = (I_x^N, I_y^N, I_z^N), I_N = 1$ is coupled by the earlier described hyperfine interaction $\mathbf{A}(\theta)$. As depicted in figure 5.7, the NV–center couples to MTSSL spin labels via dipolar coupling $\mathbf{F}^k$ and furthermore the MTSSL labels are coupled by dipolar coupling $\mathbf{J}^{kl}$. This coupling is assumed only to be significant for pairs of MTSSL spins on the same peptide, while couplings to all other more distant spins are described by decoherence effects, which is only valid for a low concentration of spin labels. Microwave control fields are denoted by a magnetic field strengths B_1, B_2 and frequency δ_1, δ_2 respectively.

As mentioned in chapter 2.3.1, the hyperfine interaction is only of diagonal form, if the quantization axis coincides with the direction of the static magnetic field. Here, this direction is defined by the NV–center symmetry axis and this must not be the case for spin labels as exemplary depicted in figure 5.8a. Hence, hyperfine interaction of each spin label is dependent on orientation, defined by the angle θ of the spin label and the NV–center principal frames of reference. To express the MTSSL hyperfine interaction tensor in the NV frame of reference we therefore need to apply a unitary transformation $\mathbf{A}(\theta) = \mathbf{R}(\theta) \cdot \mathbf{A} \cdot \mathbf{R}(\theta)^\dagger$ to its diagonal form. Thereby the matrix $\mathbf{R}(\theta)$ represents a rotation around the x-axis, which can be chosen arbitrarily due to rotational symmetry. This will typically give an interaction tensor with non-zero off-diagonal elements. Using the rotating wave approximation as introduced in chapter 2.3.3, however, will neglect all terms that contain S_x or S_y, as long as the electron Zeeman term is much larger than any of the hyperfine constants.

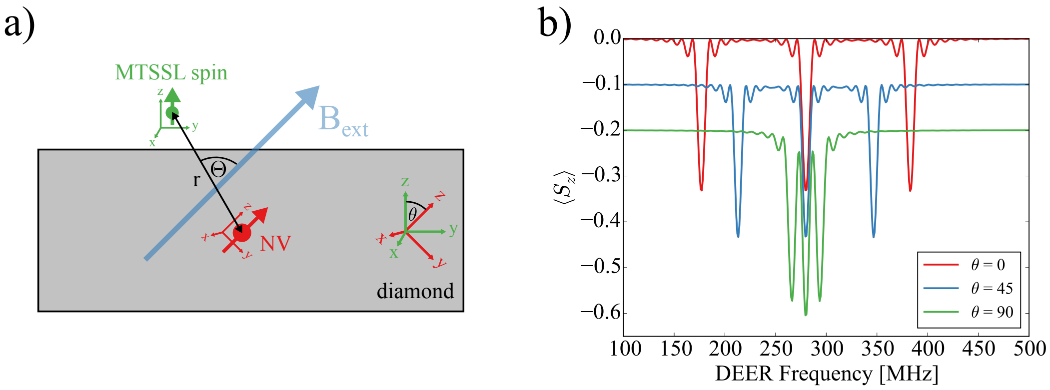

Figure 5.8.: Orientation dependence of NV-DEER Spectroscopy on a single MTSSL spin label. a) Geometry of DEER experiment on MTSSL spin label. Θ is the angle that governs dipolar coupling strength, θ the angle that modifies apparent MTSSL hyperfine interaction. b) Simulated outcome of a DEER sequence. Used simulation parameters: $\gamma B = 280$ MHz , $\Omega_{\mathrm{NV}} = \Omega_{\mathrm{sl}} = 10$ MHz, $\omega_{dd} = 200$ kHz, $\tau = \pi/\omega_{dd}$.

Additionally, dipolar couplings can be simplified according to the discussions in chapter 2.3.2. Using the secular approximation, the dipolar coupling between spin labels can be brought to the form of equation 2.19, as Larmor frequencies of MTSSL spin labels are comparable. In the case of couplings between the NV-center and MTSSL spins the secular approximation becomes even more trivial, due to the fact that the difference in Larmor frequencies is one order of magnitude owing to the NV-centers' zero field splitting at intermediate fields of $B = 10$ mT. This will bring the NV–MTSSL dipolar coupling to the Ising like form of equation 2.20.

Summing up, the Hamiltonian of the system under investigation can be written as:

$$
\begin{aligned}
H = {} & \Delta_{\mathrm{NV}} S_z^2 + \gamma B S_z + \sum_{k}^{M} \left[\Delta_{\mathrm{sl}} \sigma_z^k + A_{zz}(\theta) \sigma_z I_z + A_{zy}(\theta) \sigma_z I_y \right] \\
& + \underbrace{\sum_{k}^{M} F^k S_z \sigma_z + \sum_{k,l} \left[J_{kl}^{\perp} \left(\sigma_+^k \sigma_-^l + \sigma_-^k \sigma_+^l \right) + J_{kl}^{\parallel} \sigma_z^k \sigma_z^l \right]}_{\text{dipolar coupling}} \\
& + \underbrace{\Omega_{\mathrm{NV}} S_x + \sum_{k}^{M} \Omega_{\mathrm{sl}} \sigma_x^k}_{\text{external control}}
\end{aligned}
\tag{5.2}
$$

where we used the MTSSL detuning $\Delta_{\mathrm{sl}} = \gamma_{\mathrm{sl}} B - \delta_1$ and the angle dependent hyperfine constants $A_{zy}(\theta) = (A_{xx} - A_{zz}) \cos(\theta) \sin(\theta)$ and $A_{zz}(\theta) = A_{xx} \sin^2(\theta) + A_{zz} \cos^2(\theta)$. The control terms are only present in the Hamiltonian when we apply the respective microwave pulse with driving strengths Ω_{NV} or Ω_{sl}.

We can use the above Hamiltonian to investigate the outcome of a DEER spectroscopy measurement on a single MTSSL spin label using the numerical methods presented in chapter 2.3.4. Numerical simulations of a DEER sequence (chapter 4.2) are shown in figure 5.8b in dependence on the angle θ between MTSSL and NV–center. The spectrum is split in three equidistant peaks of the same magnitude, which stems from the fact, that MTSSL spins are unpolarized. Depending on the angle to the NV–center, each apparent hyperfine splitting between A_{zz} and A_{xx} can be realized. It needs to be pointed out that the peak-positions can be modified significantly if the secular approximation used for the derivation of hyperfine interaction breaks down. For the intermediate fields used here, these effects might already become apparent. For further treatment of this behavior the reader is pointed towards the supplementary material in reference [2].

Ambient DEER spectroscopy

Prior to any attempt of external spin detection, around ~ 50 NV–centers have been pre-characterized on the freshly cleaned diamond membrane at ambient conditions. Each individual NV–center has been screened for a coupling to electron spins using DEER spectroscopy protocols. Most of the times no indication of external spins was found on a freshly cleaned diamond substrate. Only in about $\sim 10\%$ of the cases a signal similar to what has been presented in chapter 4.2 was found, i.e. a hyperfine-less free electron spin, that most likely stems from a surface dangling bond.

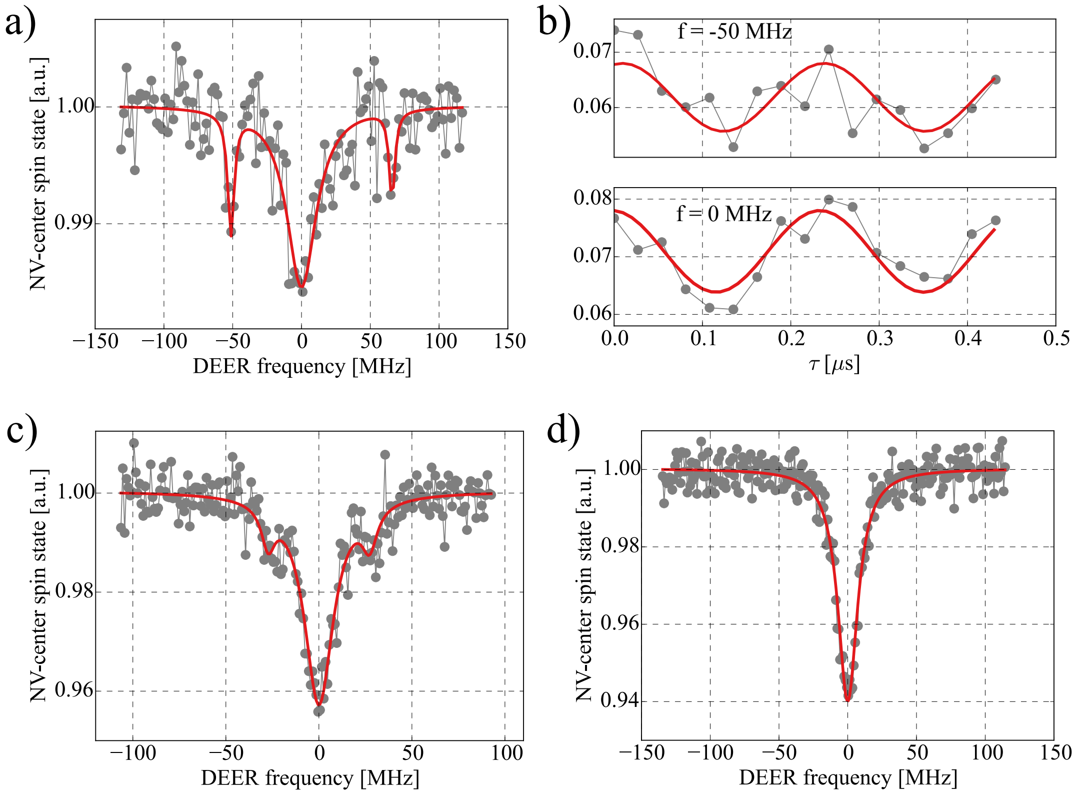

Figure 5.9.: Ambient DEER Spectroscopy on NV–centers with deposited NP$_{10}$N. a) and c) are spectra that exhibit side-peaks due to hyperfine interaction, b) is a DEER Rabi measurement on the central and left side-peak of a). d) Frequently encountered spectrum showing no hyperfine interaction, nonetheless attributed to the nitroxide electron spins.

Upon coating the diamond with fully spin labeled peptides, nearly *every* NV–center subsequently showed an external electron spin signal. Importantly, in this approach the peptides also serve as a natural spacer between the electronic spins, effectively preventing the formation of a strongly coupled fast fluctuating spin bath. Such a bath would suppress the MTSSL longitudinal relaxation time to a point where it has negligible phase imprint on the NV–center, rendering DEER spectroscopy impossible. In figure 5.9a+c+d, spectra acquired at ambient conditions are shown. Although most likely > 50 spins are present within the detection volume, spectra 5.9a+c strikingly show distinct hyperfine side-peaks. This behavior can be attributed to motional narrowing, exactly like in regular ESR spectroscopy. Although the peptides are not in solution any more, motional narrowing can still be significant. As shown in figure 5.9b, each of these hyperfine lines shows Rabi oscillations, confirming coherent control over these external electron spins. However, most of the precharacterized NV–sensors actually show the appearance of a strong peak at the free electron spin transition without any hyperfine side-peaks as shown in figure 5.9d.

Unfortunately, we observe a bleaching of the MTSSL spin label contrast on an hour timescale, rendering more elaborate experiments impossible. MTSSL signal bleaching occurs for all of the investigated NV–centers at ambient conditions. Photo-bleaching, i.e. chemical reactions and the accompanying structural and electronic changes induced by supplying energy in the form of photons, is actually a well-known problem in optical excitation of organic molecules. Since typically around $1\ \mathrm{mW}$ of laser power is focused on a diffraction limited spot to saturate the NV-center fluorescence, the spin labels within dipolar coupling range also experience a power density of usually $10^9\ \mathrm{W \cdot cm^{-3}}$, which can often lead to a redistribution of electrons and a subsequent change or loss of the electronic spin properties of the molecule. To prevent bleaching, lowering the temperature of the system under investigation is of great benefit [186] as well as stripping the environment of air to prevent reactions. Therefore it seems obvious, that NV-magnetometry on organic radicals should be performed at cryogenic and UHV conditions. Consequently, measurements at ambient conditions are kept as short as possible and are only used to verify the presence of MTSSL spin signal.

5.3.3. Temperature Dependent Spin Dynamics

Taking the previous findings into account, after brief measurements in the ambient stage, samples are quickly transferred to the cryogenic and ultra high vacuum environment of the setup. Indeed, at these conditions we observe no photobleaching over several weeks for the MTSSL signal, therefore providing excellent stability and reproducibility.

Notably, a uniform broadening of DEER spectroscopy lines can be observed at liquid helium temperature $T = 4.2$ K. To investigate this, the same NV–centers, as for example the ones shown in figure 5.9, are revisited at low temperature. As is depicted in figures 5.10a+b, spectra that exhibit hyperfine side-peaks at ambient conditions now show a single broad peak with a three to fourfold increase in linewidth, as shown in figure 5.10b. However, in a few cases spectra are observed that rather need to be described by a central peak at the $g = 2.0$ transition and two broad hyperfine side-peaks,

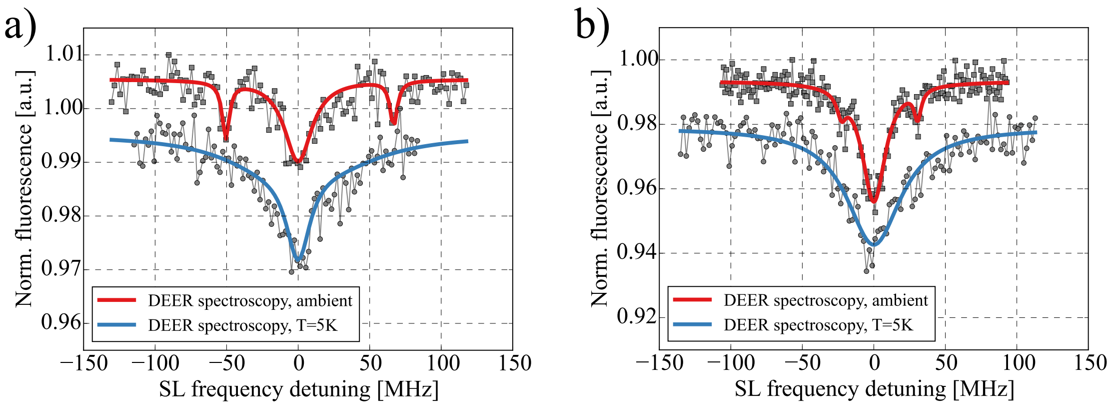

Figure 5.10.: Differences in DEER spectroscopy at ambient and low temperatures. Both graphs show spectra recorded at room temperature (red) with a clear hyperfine splitting. At low temperature (blue) spectra are broadened.

very similar to EDFS spectroscopy of the peptide sample at low temperatures in solution (figure 5.4a).

This behavior can thus be rationalized by remarking that at low temperature many frozen MTSSL labels are probed in a characteristic measurement time (NV–center $T_2 \sim$ µs) much shorter than any spin motion. As we essentially suppress all rotational and diffusive motions by cooling to liquid helium temperature, spectra can be reproduced by a summation over many spins at random angles and coupling strengths to the NV–center. However, we now have to take decoherence and spin flip-flop effects on MTSSL spins into account, owing to the dense concentration of spin labeled peptides. As pointed out in chapter 2.3.2, dipolar coupling between electronic spins leads to both these effects. These S_z (transversal relaxation) and S_+S_- (longitudinal relaxation) spin operators are included in the numerical simulation as decoherence operators, with their strength depending on the MTSSL concentration. Using the Hamiltonian from eq. 5.2, simulations of DEER spectra with decoherence effects are shown in figure 5.11 for different numbers and T_1 times of spin labels.

Assuming that every peptide is doubly spin labeled and densely packed, a rough estimation for the average distance between spin labels is 3 nm, as determined for intra-peptide coupling in EPR. Hence, T_1 due to dipolar coupling in a fully spin labeled peptide sample should be around ~ 1 µs. This already leads to a significant line-broadening in DEER spectroscopy on a single MTSSL spin label (figure 5.11, blue curve). As one adds more MTSSL labels to the simulation it turns out that already ~ 20 spins at random angles and positions lead to indistinguishability of individual hyperfine contributions to

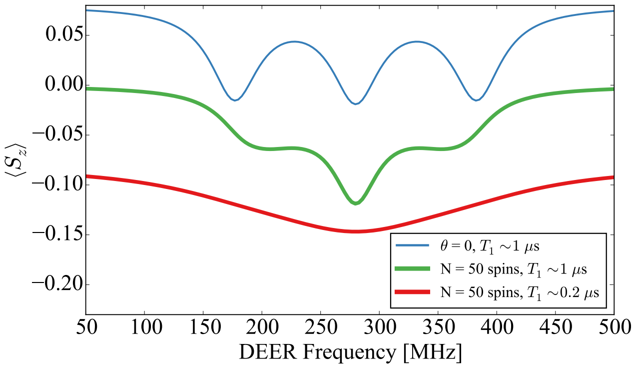

Figure 5.11.: Effect of decoherence in a single MTSSL spin label at $\Theta = 0$ (blue curve). Green curve shows the DEER spectrum with coupling to 50 MTSSL spins oriented randomly on the diamond surface, motional narrowing is not taken into account here.

the spectrum (figure 5.11, green curve). Furthermore, as T_1 is lowered, for example by a parallel stacking of peptides [187] and a resulting higher coupling strength, the spectrum evolves to a single broad peak. Experimentally the latter case is observed much more frequently on densely packed peptide samples, which suggests that the average coupling is higher than the intra-peptide spin-spin distance. This is not surprising, because the polyprolines used have a elongated cylindrical form with a diameter of 1 nm [187]. However, the linewidth is smaller than suggested by simulation, which hints towards other effects not included here. Interestingly, a line-broadening can also be caused by T_2-type decoherence, where coherence timescales an order of magnitude lower than T_1 have a comparable spectral impact. As transversal relaxation on target spins does not have an effect on the DEER spectroscopy measurement itself, however the ineffectiveness of spin flips ($T_2^{-1} \sim \Omega_{\mathrm{sl}}$) causes the line-broadening effect.

An investigation of Zeeman splitting often helps to identify the source of an observed spin signal by assigning gyromagnetic ratios. In figure 5.12a, DEER spectroscopy measurements at different magnetic field strengths are conducted which reveal the gyromagnetic ratio if the magnetic field is known. Here the magnetic field strength is expressed as a predefined current setting in the vector magnet, that has been aligned with one of the four possible NV–center directions and subsequently linearly increased as indicated in the legend of figure 5.12a. The acquired spectra exhibit a slightly different broadening and contrast for different magnetic field strengths. This is due to the transmission function in the applied RF-band, which was independently monitored and actually varies by a few dB in the cryogenic setup. Since the π-pulse was not

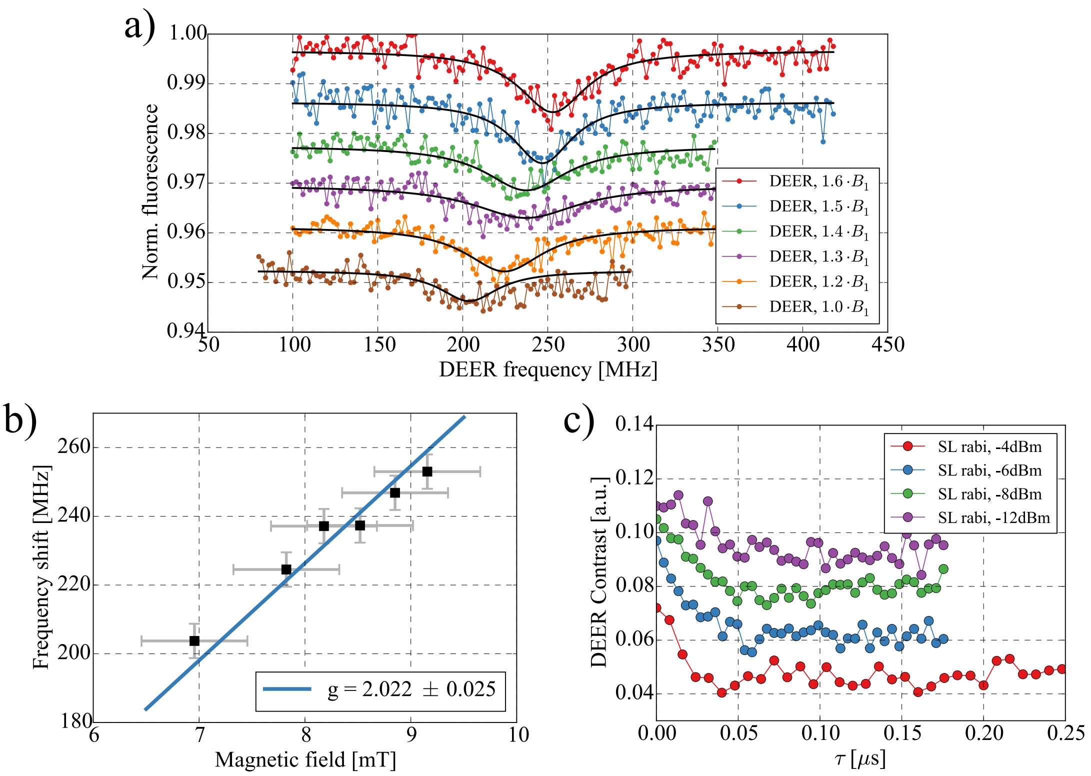

Figure 5.12.: Behavior of the MTSSL electronic spin in densely packed samples. a) Shift of transition frequencies depending on the external magnetic field strength. b) Calculation of g–factor from a). c) DEER Rabi measurement on the central peak. Less than a full oscillation can be achieved except for highest powers (red curve).

adjusted specifically for each frequency, this results in fluctuating efficiency of external spin excitation and thus a variation in line-broadening and intensity.

The magnetic field can be back-calculated from the measured NV spin transitions which allows for g-factor determination as illustrated in figure 5.12b. Due to the fact that the magnetic fields used are rather low, the error in this calculation is high. Namely, uncertainty in the estimated strain parameter E has a larger weight in the magnetic field calculation, since it can only be determined via resonant excitation. Magnetic fields can usually be aligned with the NV–center axis at the ground state level anticrossing (GSLAC, ~ 100 mT) or excited state level anticrossing (ESLAC, ~ 50 mT), where off-axis fields have highest impact [141]. As this is currently not possible in the cryogenic setup, a large error in total magnetic field strength emerges. Hence, the determined g-factor of 2.02 matches the expected value of 2.002 within the error margin, yet this uncertainty is the reason why more specific statements can not be made.

To further elucidate experimentally how dipolar coupling plays a role in these densely packed samples, observation of DEER Rabi oscillations as introduced in chapter 4.2 have been conducted. In figure 5.12c, Rabi oscillation measurements of the MTSSL spin labels imprinted on the NV–coherence are shown in dependency of applied microwave power Ω_{sl}. Indeed, not even a full oscillation period can be driven and rather a pure decay to the mixed state is observed. Only at higher RF-powers half a period becomes apparent (figure 5.12c, red curve). This confirms high MTSSL-MTSSL coupling on the order of $\gg 10$ MHz and confirms the assumed dense packing of spin labels.

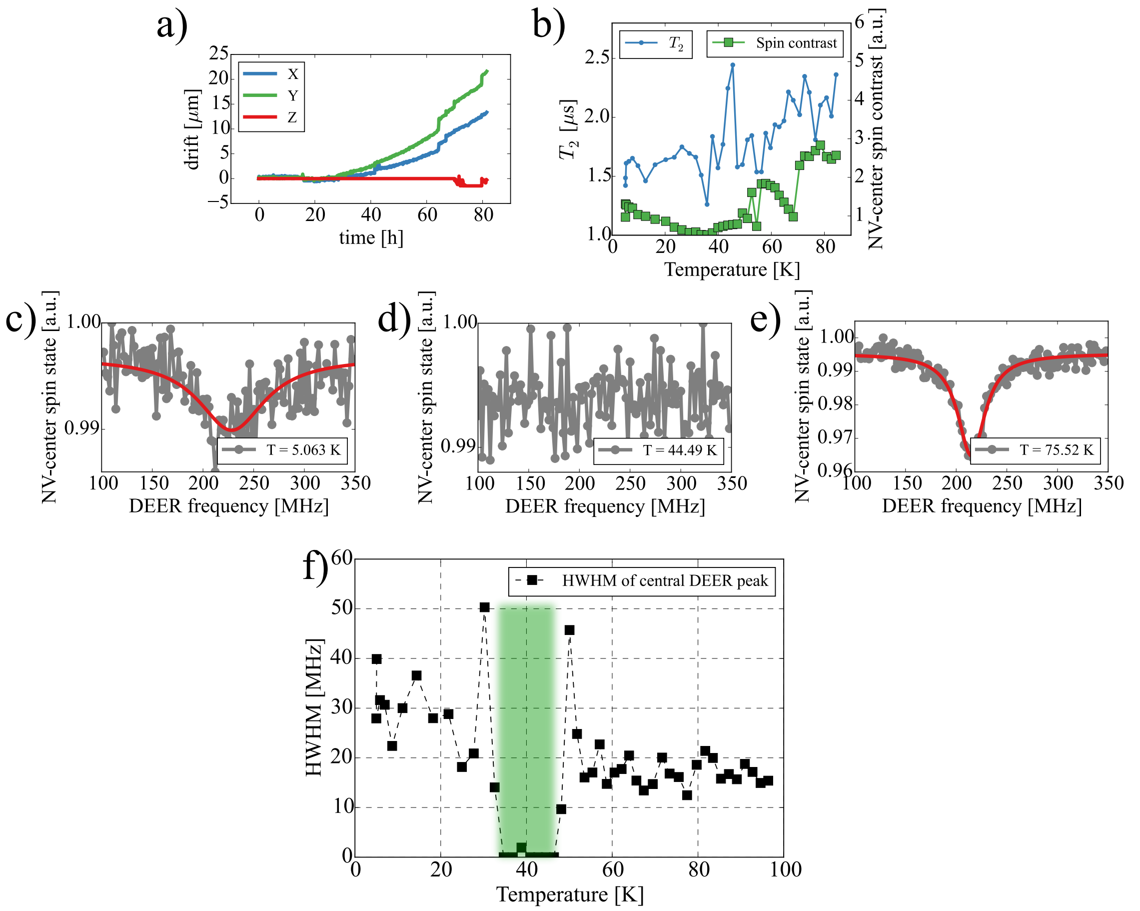

Figure 5.13.: Temperature dependent DEER spectroscopy on a dense MTSSL spin label sample. a) Tracked drift of the NV–center. b) Temperature-dependent spin properties of the NV–center. c)-e) DEER spectra at different temperatures. f) Temperature dependent HWHM in DEER spectroscopy. Within the marked area the DEER signal completely vanishes.

The above elaborations, especially comparing low and ambient temperature spectroscopy, raise the question when a transition between the frozen spin dynamics and the motional narrowed spectra occurs. For this reason we investigated the temperature dependency of the DEER spectrum of a few NV–centers. This was done by slowly warming up the cryogenic measurement head towards ambient temperatures as cooling agents (liquid helium) are not resupplied. This approach results in an almost linear increase in temperature of the sample, with a heating rate of 1 K/h. During this time one can constantly track the confocal position of single NV–centers shown in figure 5.13a, where drift during such a heating cycle with respect to the original NV position is illustrated. To exclude any artifacts caused by thermal changes, ODMR transition, coherence and fluorescence countrate are monitored after each DEER measurement. These properties are shown in figure 5.13b. We observe a slight increase in spin contrast, which is caused by an increase in countrate as the objective collection efficiency improves towards higher temperatures. Additionally a minor trend of increasing coherence time occurs, which is however not reproducible in other NV–centers.

Strikingly, monitoring the external MTSSL electron spin signal over temperature reveals a non-intuitive behavior as DEER contrast is completely lost within a range of $\sim 30-50$ K, presented in figure 5.13f, with exemplary spectra at various temperatures of interest in figures 5.13c+d+e. After this loss of electron spin signal, the DEER peak quickly reappears with a higher contrast and a narrower linewidth. We observe this behavior for each NV–center investigated on the sample, albeit slight variations in the temperature span in which DEER contrast vanishes completely occur.

Naively, one would expect a gradual transition from broad to narrow linewidth as the temperature is increased and rotational and diffusional motions start to become comparable to the NV–center evolution time ($\sim 1-10$ µs). If the molecular rotational timescale matches the free evolution duration τ set in DEER spectroscopy it might be possible that the effect of a π-pulse on the spin label is neglected, similar to NMR detection schemes in NV magnetometry. However, this should become apparent in a simultaneous drop in NV–center T_2, which we do not observe. A loss of contrast could also occur, if P_{10} peptides would undergo a conformational change and MTSSL-MTSSL distances become as short as ~ 1 nm. Assuming a change of a polyproline II helix (shown in figure 5.1) to a polyproline I helix, distance of spin labels could change from 3.1 nm to 1.9 nm [187]. Additionally, packing densities of peptides in crystalline form can have lattices constants as low as 0.6 nm between neighboring molecules. Such a behavior should then also occur in regular EPR spectroscopy measurements on diamond dropcasted peptide solutions. Efforts to reproduce this sample geometry in regular EPR spectroscopy were unsuccessful. In liquid solutions this behavior does not occur as confirmed by the temperature dependent measurements in section 5.2.

5.4. Probing Dipolar Coupling Between Spins on the Nanoscale

To fully harness nanoscale sensing capabilities of the NV–center spin sensor, it is desirable to perform spectroscopy on only few spins. For one, this opens up new possibilities for structural determination or reactions that happen on a single molecular level. Secondly, a lower spin density, which e.g. increases relaxation times, opens up pathways for a coherent coupling among those spin labels.

5.4.1. Coupling to Few Spins

To couple only to few spins, it is necessary to decrease the concentration of spin labels in the detection volume of the NV–center spin. This can be achieved, for example, by a (sub-)monolayer coverage of the diamond surface with a certain spin species, where bonding to the diamond surface limits surface coverage. Such techniques were already successfully incorporated for NV–NMR or decoherence magnetometry [44, 126]. Since the peptide spacer provides naturally dispersed electron spins, a suitable approach in our case is diamagnetic dilution of the peptide stock solution. This means that fully spin labeled peptides NP$_{10}$N are intermixed with unlabeled peptides of the same type P$_{10}$ in solution and dropcasted on the diamond surface analogous to the previous approach. On account of this there will be fewer spins within the detection volume, which statistically allows for single peptide detection, given the right concentration and characterization of a sufficient number of NV spin sensors.

For such a sample preparation, we used a peptide stock solution in a ratio of 1:10 of labeled to unlabeled peptides and verified the external spin signal at ambient conditions. Then, the sample is quickly brought to UHV and cooled down. Now, many NV–centers exhibit a DEER spectrum that has a central peak at the free electron transition and two shoulders (figure 5.14a), as was only sometimes observed on the undiluted sample. Moreover, a screening of around 40 NV–centers reveals two cases where distinct side peaks are observable as shown in figure 5.14b. This points towards coupling to only few spin labels, where the four side peaks are probably caused by pairs of nitroxide spin labels at different angles and positions with respect to the NV–center axis. Thus, we perform an in-depth analysis of the external spin couplings on the NV–center on which the spectrum shown in figure 5.14b is recorded for the remainder of this chapter.

In the first instance, DEER Rabi measurements on the external electron spins are performed, which are shown in figure 5.14c. Indeed, many oscillation periods can be

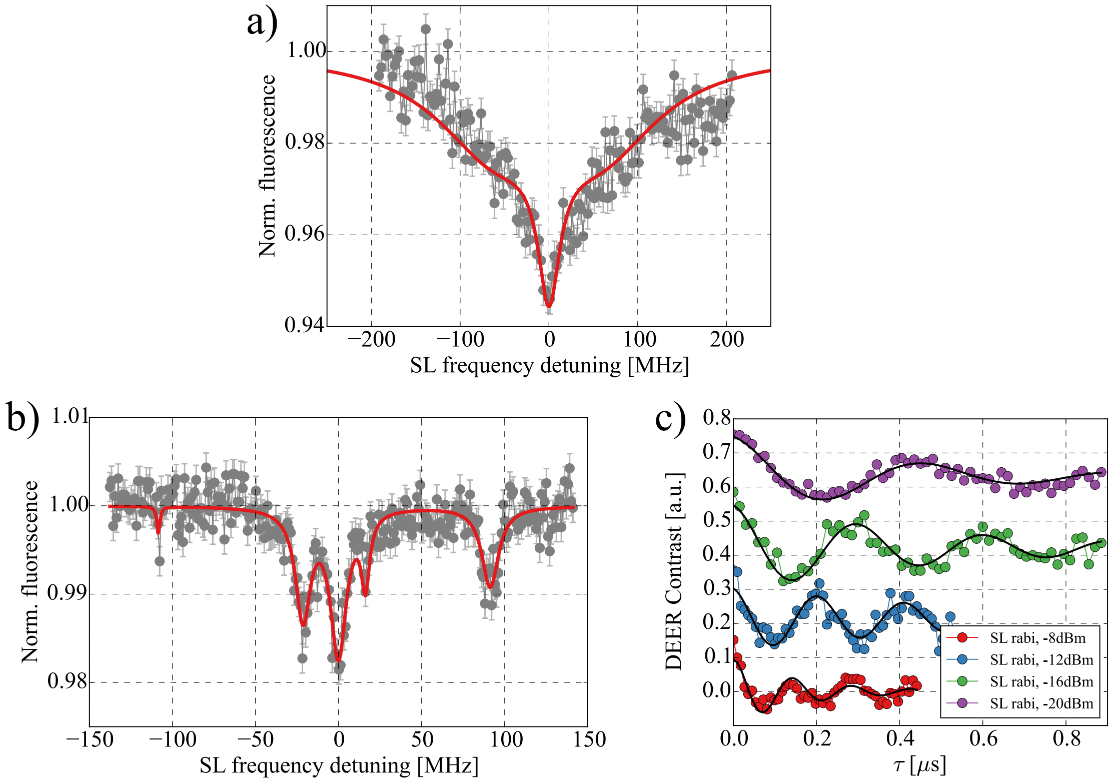

Figure 5.14.: DEER spectroscopy on diamagnetically diluted sample. a) More often than not, spectra with clear shoulders are encountered. b) For some NV–centers spectra that exhibit narrow hyperfine lines can be found. c) DEER Rabi oscillation measurements at different microwave powers on the central transition peak of spectrum b).

observed, in contrast to the pure decay in previous dense spin samples. The shown measurement was carried out exciting external spins on the central peak with zero detuning (frequency that corresponds to $\gamma_{\mathrm{sl}}B$), however any peak shows the same behavior.

For the acquisition of the spectrum in figure 5.14b, a slight modification to the regular DEER spectroscopy sequence introduced in chapter 4.2 was used. It has been shown that instead of using a coherent superposition $|\sigma\rangle$ between states $|0\rangle$ and $|\pm1\rangle$ (see also equation 2.2), using a double quantum superposition $|\Psi_{\mathrm{dq}}\rangle$ between states $|1\rangle$ and $|-1\rangle$ can greatly enhance sensitivity [188]. After a measurement sequence the NV–center spin state will read:

$$|\Psi_{\mathrm{dq}}\rangle = \frac{1}{\sqrt{2}}\left(e^{-i\phi(t)}\,|-1\rangle + e^{i\phi(t)}\,|1\rangle\right)$$

i.e., both substates will have picked up a phase through Zeeman interaction, yet of opposite sign. Therefore a measurable phase difference is generated twice as fast. Thus

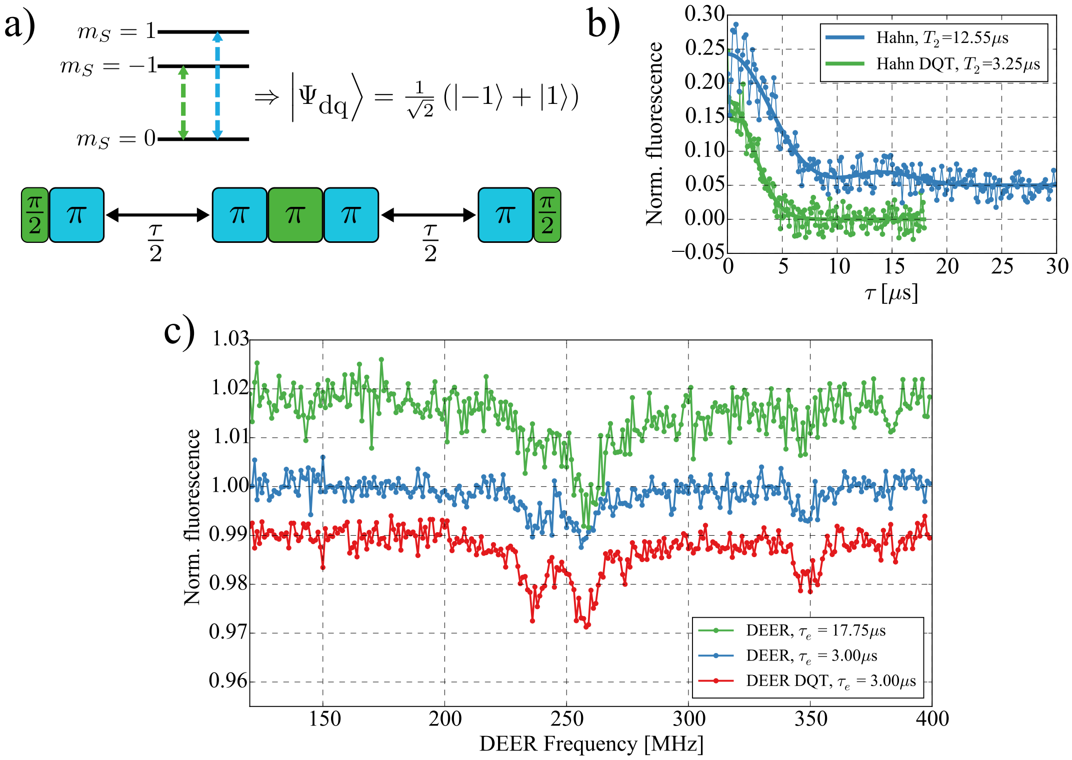

Figure 5.15.: Sensitivity comparison of regular and double quantum magnetometry DEER. a) Measurement sequence for Hahn echo on double quantum state $|\Psi_{\mathrm{dq}}\rangle$ shown above the sequence. b) Comparison of coherence time with a regular Hahn echo (blue) and a double quantum Hahn echo (green). c) Contrast enhancement via DQT-DEER spectroscopy. Total signal acquisition time was identical for all three measurements (4 hours).

the DEER sequence can be modified to operate on the double quantum transition (DQT) in the NV–center spin subspace, which leads to an enhanced sensitivity.

However, this double quantum transition can not be addressed directly, since a direct crossover from $|0\rangle$ is only possible via a two photon process due to spin momentum conservation. A suitable solution is to create $|\Psi_{\mathrm{dq}}\rangle$ using both $|0\rangle \rightarrow |-1\rangle$ and $|0\rangle \rightarrow |1\rangle$ transitions. This can either be done simultaneously by appropriate frequency mixing, or the sequential sequence depicted for a Hahn echo measurement in figure 5.15a [189]. A combination of a $\pi/2$-pulse on one transition and a π-pulse on the other creates $|\Psi_{\mathrm{dq}}\rangle$ and a triple alternating π-pulse train swaps population between $|1\rangle$ and $|-1\rangle$.

A drawback of this sensitivity enhancement is obviously that noise from the environment will have a stronger influence on spin coherence as well. Accordingly, a Hahn echo measurement using the double quantum state $|\Psi_{\mathrm{dq}}\rangle$ reveals a decrease in coherence (figure 5.15b, green curve) by a factor of 4 in comparison to a regular Hahn sequence (figure 5.15b, blue curve), which was fitted using equation 2.10. The loss in coherence time can often greatly exceed the gain in sensitivity, due to the properties of the ^{13}C spin bath [189], which has to be taken into account when considering the suitability of this approach.

A comparison of a DEER sequence using this double quantum Hahn echo is finally shown in 5.15c on the previously introduced spectrum of diluted MTSSL spin labels. For better comparability, the total acquisition time of each acquired spectrum was set to four hours, while fluorescence countrate stayed constant. Truly, a comparison of regular spectroscopy (blue) and the DQT spectrum (red), where NV–center phase evolution times are matched, shows a twofold increase in DEER contrast, endorsing the sensitivity increase through DQT magnetometry. Different relative peak intensities are visible when acquiring a spectrum with a larger phase evolution time, which is only possible for regular spectroscopy. This is however unsurprising, since peak intensities depend on MTSSL to NV coupling strength.

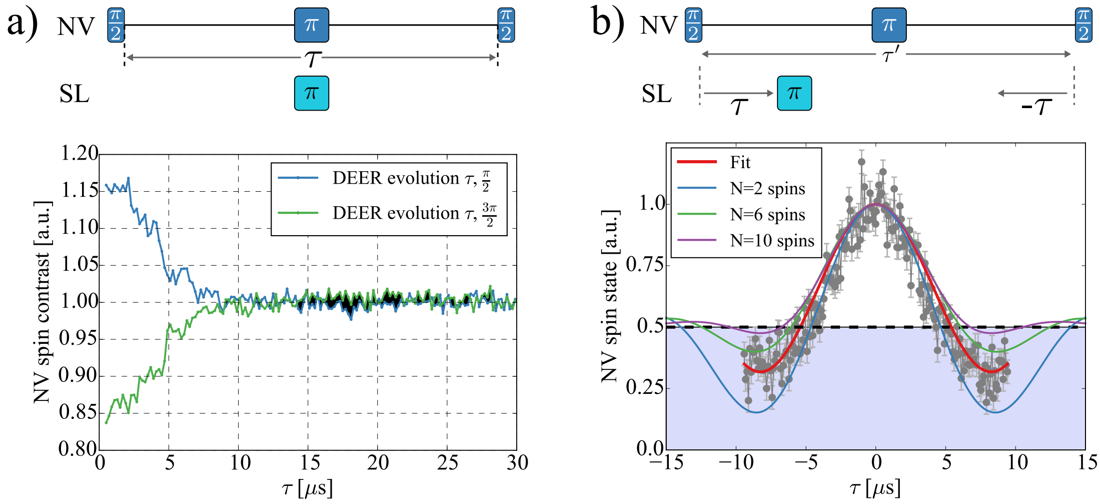

Figure 5.16.: Measuring couplings to only few spin labels. a) Sweeping the total free evolution time of a DEER measurement. Spin state inversion (black shaded area) is a sign for coherent spin coupling in the few spin limit. b) Fixing total free evolution time τ' removes environmental influences on the measurement outcome. Blue shaded area represents spin state inversion.

To address the question of how many spins are located within the detection volume one needs to acquire more information. Spectrum 5.14b allows no quantitative conclusion, as hyperfine peaks from different spin labels might not be well-separated spectrally and thus impossible to resolve. However, one can gain more information by studying how the NV spin state phase pickup is influenced due to dipolar interactions in the free evolution periods of a DEER sequence. This can be achieved by keeping the external spin manipulation pulse at a fixed transition and varying the free evolution duration τ as depicted in figure 5.16a, or keeping the free evolution duration τ' constant and shifting the external spin flip therein as depicted in figure 5.16b.

The expected outcome of such measurements can be calculated using a unitary evolution on the system Hamiltonian eq. 5.2. According to equation 2.27, fluorescence response of the NV can be computed as:

$$\begin{aligned} C_{\mathrm{NV}}(\tau) &\propto \mathrm{Tr}\left[\varrho(\tau)\left|0\right\rangle\left\langle 0\right|\right] = \mathrm{Tr}\left[V_{\mathrm{seq}}\varrho_0 V_{\mathrm{seq}}^{\dagger}\left|0\right\rangle\left\langle 0\right|\right] \\ \varrho_0 &= \varrho_{\mathrm{NV}}^{\pi/2} \bigotimes^{M} \mathbb{1}_{\mathrm{MTSSL}} \\ &= \begin{pmatrix} 0 & 0 & 0 \\ 0 & \frac{1}{2} & \frac{1}{2} \\ 0 & \frac{1}{2} & \frac{1}{2} \end{pmatrix} \bigotimes^{M} \begin{pmatrix} \frac{1}{2} & 0 \\ 0 & \frac{1}{2} \end{pmatrix}. \end{aligned} \tag{5.3}$$

The initial density matrix ϱ_0 is composed of the pure coherent NV state after laser illumination and $\pi/2$-pulse and the fully mixed states for M unpolarized MTSSL spin labels. For sake of simplicity, we can trace out the nuclear ^{14}N Hilbert subspace of MTSSL due to the fact that we drive them on the central transition common for all external spins and do not induce any nuclear spin state transitions. The evolution operators V_{seq} for each sequence can be expressed using unitary gates from eq. 2.28:

$$\begin{aligned} V_{\mathrm{tau}} &= U_{\pi/2}^{\mathrm{NV}} U\left(\tau\right) U_{\pi}^{\mathrm{SL}} U_{\pi}^{\mathrm{NV}} U\left(\tau\right), \\ V_{\mathrm{rf}} &= U_{\pi/2}^{\mathrm{NV}} U\left(\tau'\right) U_{\pi}^{\mathrm{NV}} U\left(\tau' - \tau\right) U_{\pi}^{\mathrm{SL}} U\left(\tau\right), \end{aligned} \tag{5.4}$$

where V_{tau} and V_{rf} stand for the sequences depicted in figures 5.16a and 5.16b, respectively. The time evolution operator is thus:

$$U\left(\tau\right) = \exp(-iH\tau) = \prod_{k}^{M} \exp\left(-i\Delta_{\mathrm{sl}}\sigma_z^k\tau\right) \exp\left(-iF^k S_z \sigma_z^k \tau\right) \tag{5.5}$$

The second equality holds, since all terms in the Hamiltonian eq. 5.2 acting solely on S_z are canceled out after the full sequence due to the time-symmetric NV π-pulse.

The same argument holds for the dipolar coupling term between external spin labels, because they are in a mixed state. This implies also that intra-peptide $\boldsymbol{J}$-coupling will not generate a phase on the NV–center when applying a simple spin label π-pulse.

With the above equations, the outcome of both measurement sequences is exactly the same and can be written as:

$$\begin{aligned} C_{\mathrm{NV}}(\tau) &= \frac{1}{4}\left[2 + \prod_{k}^{M}\left(e^{iF_k\tau} + e^{-iF_k\tau}\right)\right] \\ &= \frac{1}{2}\prod_{k}^{M}\left(1 + \cos(F_k\tau)\right). \end{aligned} \tag{5.6}$$

For the idealized case of a single MTSSL spin, this leads to a coherent oscillation of the NV–center electronic spin with the period defined by the dipolar coupling strength F. As one subtracts the outcome of two measurements, whereby the second ends with a $3\pi/2$-pulse instead of a $\pi/2$-pulse on the NV–center spin, the result is a complete NV–center spin state reversal. This means that if the NV spin state was $|0\rangle$ prior to the measurement, it ends up in $|1\rangle$ for the right timing and vice versa. This coherent behavior can only occur for coupling to few spins. Many different couplings result in the multiplication of many cosines of different frequency, which negates overshoot below $C_{\mathrm{NV}}(\tau) < 0.5$. For many spins in coupling range to the NV–center rather a decay to the mixed state $C_{\mathrm{NV}}(\tau) \geq 0.5$ will be observed.

In the spectrum in figure 5.14b a coherent behavior is observed, visualized through the shaded area in figure 5.16a. However, interpretation of this result still proves to be difficult, because effects of the carbon spin bath are superimposed on the measurement outcome and create additional features (equation 2.10). This can be accounted for by the addition of a spin bath operator to the system Hamiltonian 5.2.

However, an alternative approach is to use the sequence shown in figure 5.16b, where the free evolution time of the NV spin τ' is fixed. This effectively prevents any influence from other magnetic sources on the measurement outcome, that are not actively manipulated by the SL π-pulse and presents a formidable way of addressing specific spin couplings. The result of this measurement in figure 5.16b shows the previously observed spin state inversion in a background-free way. For this, measurements ending in NV $\pi/2$ and NV $3\pi/2$-pulses have been subtracted and a spin state inversion is thus indicated by a crossing of the dashed black line towards the blue shaded area. The variable τ in graph 5.16b is chosen in such a way that it represents the effective interaction time between NV spin and MTSSL spins. A simultaneous π-pulse on NV and spin label corresponds to maximal phase imprint from dipolar interaction ($\tau = 0$), while a spin label π-pulse at the beginning or end of the decoupling sequence has no effect ($\tau = \tau'$). For symmetry purposes, a negative τ represents a sweep in the opposite direction from the end of the sequence.

A comparison with equation 5.6 is now possible. For an estimation of the number of spins that contribute to the signal, spins are placed randomly within the sensing volume of the NV-center. The boundaries are defined by implantation depth (~ 7 nm) on the lower end and by NV-center decoherence on the upper end ($T_2 = 12.6$ µs $\rightarrow$ sensing distance ~ 15 nm). A few simulations using eq. 5.6 are overlaid in figure 5.16b for a few spin configurations. It becomes apparent, that the measured behavior can only be reproduced for very few spins within the coupling volume. However it needs to be pointed out, that when using different parameter sets the outcome of this delay measurement can vary significantly. For example it would also be possible to reproduce the measured oscillation using only a single specifically oriented spin labeled peptide NP$_{10}$N. Hence, due to this qualitative nature of the fit, we can only give an upper bound estimation for the number of spins which is $M \leq 6$. With a larger quantity of spins it is nearly impossible to reproduce the magnitude of spin state inversion exhibited, independent of the position of the spins within the detection volume (figure 5.16b, purple curve).

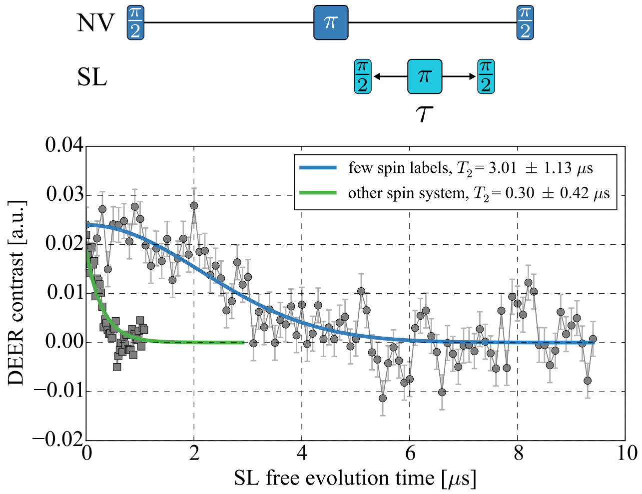

Figure 5.17.: DEER Hahn echo measurement on MTSSL spins. The blue curve is acquired on the NV–center shown in figure 5.14b, the green curve on another NV–center on the same sample, that has a different MTSSL spin configuration.

In a similar measurement the coherence of investigated MTSSL spins can be determined by the pulse sequence shown in figure 5.17. The measured phase coherence time of

$T_2 = (3.0 \pm 1.1)$ µs is in very good agreement with the previously performed standard low temperature pulsed EPR measurements on diluted peptides in solution (figure 5.4). Although these two measurements are performed in different peptide environments and are difficult to compare, this again confirms that the spin-labeled peptides are as well-separated as they were in frozen solution. Another indication for this is the Gaussian decay of coherence, a sign for a proton flip-flop limited decoherence [190] with no electron bath contribution. From any investigated MTSSL spin composition, the presented coherence time (blue fit in fig. 5.17) is by far the longest. As pointed out earlier, other NV–centers can be found that display somewhat distinct peaks in their DEER spectra, however the transversal relaxation time never exceeds 1 µs, most likely limited by electron-electron interaction to other MTSSL spins. As an example, the green curve in figure 5.17 is depicted, acquired on another MTSSL spin environment on the same sample where coherence is lower by an order of magnitude.

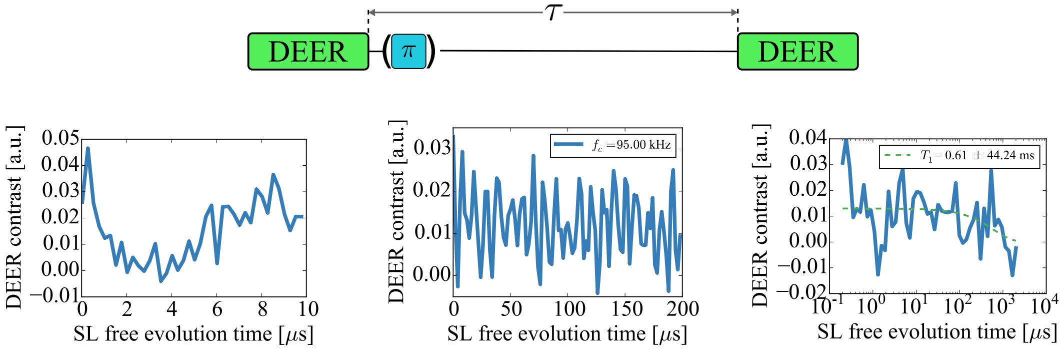

Figure 5.18.: DEER correlation measurement on MTSSL spin labels at different free evolution periods. DEER correlation sequence is shown above the measurements. Relaxation only occurs for timescales above a milliseconds.

To further consolidate the fact that for the case of the spectrum in figure 5.14b MTSSL spin labels do not reside in a spin bath configuration, longitudinal relaxation can be analyzed. Judging from the previously conducted low temperature EPR investigations (figure 5.4), for well-separated peptides, T_1 should be as long as milliseconds. This timescale cannot be accessed using the previous measurement schemes due to the limit imposed by the NV–center T_2. As pointed out in chapter 4.2, one can use DEER correlation spectroscopy to extend the accessible measurement range to the NV–center longitudinal relaxation T_1 instead. At temperatures of 4.2 K, this exceeds 100 ms, even for shallow NV-centers, which we also confirmed here.

Results of DEER correlation measurements on the central transition frequency of the spectrum in figure 5.14b are shown in figure 5.18 for different timescales. The contrast is calculated by subtracting measurements with and without an initial spin flip on MTSSL spins at the beginning of free evolution periods τ. The resulting phase correlation signal shows an unchanged amplitude over the first few milliseconds of free evolution, where thus neither longitudinal relaxation of NV-center nor MTSSL spins occurs. Taking a closer look, the correlation amplitude oscillates with a single frequency of $f_c = 95.0$ kHz, determined by FFT of the shown signal. This is caused by the overlaying effect of the ^{13}C spin bath imposed on the NV–center spin, which is independent of spin dynamics in coupled MTSSL spins [159]. This is consolidated by the fact that the correlation frequency matches the inverse timescale of ^{13}C Larmor precession, $t^{-1}_{^{13}C} = 98.5$ kHz, for the magnetic field of 9.51 mT determined from both ODMR transitions. Therefore the limiting factor in the measurement is very likely the lifetime of ^{13}C. On the ground of this, it is not possible to qualitatively determine the longitudinal relaxation of coupled MTSSL spin labels but it can be confirmed that it exceeds the available measurement range. The measurement does likewise not change for temperatures as high as 77 K since the MTSSL longitudinal relaxation still surpasses the carbon spin bath memory time. Nonetheless this again confirms well separated spin labels.

5.4.2. Coupling Between External Spins

As demonstrated in the last section, coupling to only ~ 3 MTSSL labeled NP$_{10}$N polyprolines is established. This gives the unique ability to have non-invasive coherent control over a single qubit (NV–center electron spin) coupled to electronic spin-pairs with a configured distance, engineered using biochemistry. Low temperature and ultra clean environment (UHV) enable long term stability of this spin network on the nanoscale. Moreover, the previous evidence of proton limited coherence in MTSSL spins facilitates coherent control and quantum communication within this molecular spin network. It was already shown, how NV-MTSSL couplings are extracted (see previous section). With all the above prerequisites, it is furthermore possible to implement new schemes to access the last remaining tensor in Hamiltonian 5.2, i.e. the dipolar coupling $\boldsymbol{J}$ between MTSSL spins. This completes full access to a nanoscale molecular spin network.

Using regular single-frequency DEER spectroscopy, dipolar coupling between MTSSL spins, however, cannot be measured due to the fact that the external spins are not polarized. This effectively means that all external spins are interchangeable[1] and any spectral dipolar contributions are averaged out. The result is observation of shown single

---

[1] Along these lines, numbering of spins in figure 5.19 is of pure symbolic nature. There are already techniques available or in development, however, that can address this issue. See chapter 6.

peaks instead of $\boldsymbol{J}$-split doublets in DEER spectroscopy even for MTSSL pairs with distinct coupling, sketched in figure 5.19a.

Yet, in an analogous manner to regular DEER spectroscopy in EPR, one can utilize a third frequency to address coupled MTSSL pair spins simultaneously. It seems conclusive to perform a second decoupling sequence on the spin labels themselves, as presented in figure 5.17, and additionally sweep a third π-pulse, to investigate its effect on the coherence of the spin labels. The readout is then achieved by mapping this dipolar mediated MTSSL coherence to a phase acquisition on the NV–center and finally a readable population difference. This would amount, in principle, to addressing the two spin labels located on a peptide separately by two distinct RF-frequencies, as the schemes in figure 5.19b+c suggests.

To model the effect of this triple electron-electron resonance scheme (TEER) analytically, we perform unitary time evolution according to the sequence depicted in figure 5.19c. In this case, the $\boldsymbol{J}$ coupling between MTSSL spins has to be taken into account. This was implicitly also done before, yet couplings of the form $\boldsymbol{\sigma}_i \boldsymbol{\sigma}_j$ were canceled out. As mentioned before this is because a single π-pulse does not change the sign of above coupling terms and no phase is acquired. The free unitary evolution is then written:

$$\begin{aligned} U\left(\tau\right) = &\prod_{k}^{M} \exp\Bigl(-i\Delta_{\mathrm{SL}}\sigma_z^k\tau\Bigr)\exp\Bigl(-iF_kS_z\sigma_z^k\tau\Bigr) \\ &\cdot\prod_{kl}\exp\left(-i\left[J_{kl}^{\perp}\left(\sigma_+^k\sigma_-^l-\sigma_-^k\sigma_+^l\right)+J_{kl}^{\|}\sigma_z^k\sigma_z^l\right]\tau\right). \end{aligned}$$

As all other couplings are much smaller, we only consider the intra-peptide coupling of MTSSL spin pairs located on the same peptide. Hence the NV–sensor fluorescence readout after application of the delay sequence shown in figure 5.19c can be calculated using unitary evolution equation 5.3 with $\varrho(\tau) = W\varrho_0W^{\dagger}$. In this case W is, according to figure 5.19:

$$\begin{aligned} W = &U_{\pi/2}^{\mathrm{NV}}U\left(\tau''-2\tau'\right)U_{\pi/2}^{\mathrm{SL}\ 1}U\left(\tau'-\tau\right) \\ &\times U_{\pi}^{\mathrm{SL}\ 2}U\left(\tau\right)U_{\pi}^{\mathrm{SL}\ 1}U\left(\tau'\right)U_{\pi/2}^{\mathrm{SL}\ 1}U_{\pi}^{\mathrm{NV}}U\left(\tau''\right). \end{aligned}$$

For simplicity $U^{\mathrm{SL}\ 1}$ operates in one spin subspace of a pair of external network spins while $U^{\mathrm{SL}\ 2}$ operates on the other one. After a tedious calculation where fast oscillating terms are omitted, the NV–center spin state contrast is found to be:

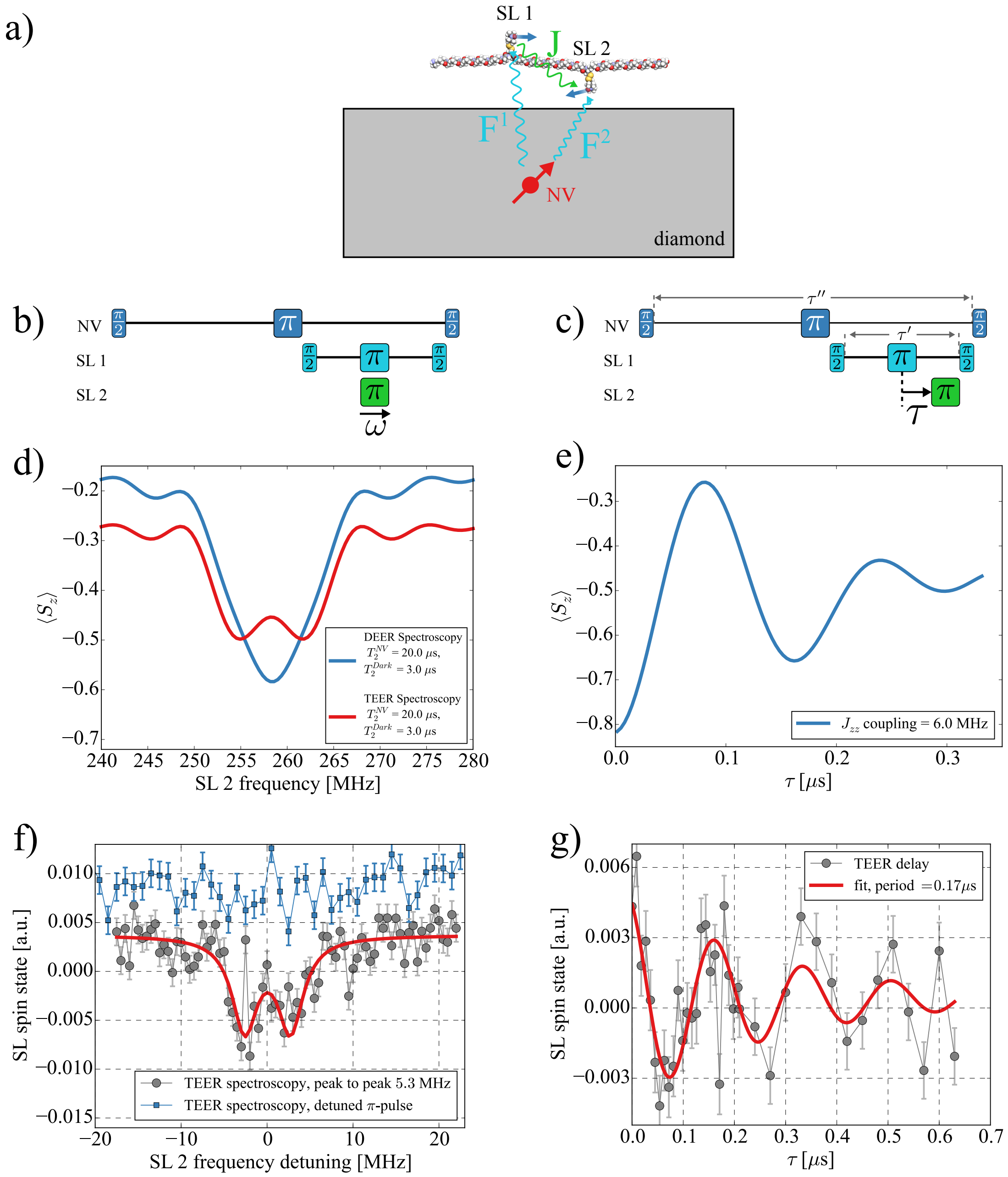

Figure 5.19.: TEER measurements to access dipolar coupling between MTSSL spins. a) Sketch of idealized experiment. b) Pulse scheme for TEER frequency measurement. c) Pulse scheme for TEER delay measurement. d) Numerical simulations of b), used parameters: $F^1_{zz} = 200$ kHz, $F^2_{zz} = 400$ kHz, $J_{zz} = 6$ MHz. e) Numerical simulations of c) with same parameters. f) TEER frequency measurement on NV–center coupled to few NP$_{10}$N. g) TEER delay measurement on same NV–center.

$$C_{\mathrm{NV}}(\tau) \sim 1 - \prod_{k}^{M} \sin^2\left(F_k \tau\right) \cos\left(J^{\|}\tau\right) \cos\left(J^{\perp}\tau\right). \tag{5.7}$$

Thus, sequences shown in figures 5.19b+c are modulated by both NV-MTSSL couplings and, most importantly, MTSSL-MTSSL couplings. Accordingly it is possible to access this coupling by an appropriate timing in the pulse sequence. Fortunately, the coupling between spin labels is much higher than to the NV–center due to the implantation depth, and the effect of F_k will be negligible on the timescale needed for the measurement of $\boldsymbol{J}$-coupling.

For a numerical calculation, the full system Hamiltonian (eq. 5.2) is used, yet only coupling to a single peptide (two MTSSL spins) is regarded for reasons of simplicity and computation time. The results can be seen in figure 5.19d+e. It is perceived that TEER sequences should not only reveal a dipolar coupling between MTSSL spins in a delay measurement, but also in a frequency sweep, in complete analogy to a DEER measurement. According to equation 5.7, the exact form of delay oscillation (figure 5.19e) depends strongly on the dipolar coupling constants between the two MTSSL spins, which are governed by the relative positions of both spins with respect to each other.

The discussed triple resonance scheme are applied on the previously investigated NV–center. Decoupling of the network spins (SL 1) is performed at their Larmor frequency, while sweeping the frequency of a third π-pulse (SL 2). The resulting spectrum is plotted in figure 5.19f and shows two distinct peaks, with a spacing of 5.3 ± 1.0 MHz. This matches what was expected from simulations and implicates a distinct dipolar coupling. To exclude any artifacts from, for example, microwave radiation, additional measurements are performed. If, for example, the decoupling pulse on MTSSL spin labels is detuned, the spectrum is featureless, as is shown for comparison in figure 5.19f.

To support these findings, the SL 2 excitation frequency is fixed at the right peak in the spectrum shown in figure 5.19f and the delay is swept. The result is a surprisingly distinct oscillation, shown in figure 5.19g, with a frequency of 5.8 ± 1.0 MHz, in agreement with the previous measurement. It needs to be pointed out, that for both TEER measurements spectra are averaged for around 24 hours, as contrast is very low compared to the photon shot noise, which is the main source of error in the measurement. This comes from the fact, that each nested measurement of coupling further decreases the contrast. Additionally the same measurements are performed on a cleaned diamond surface with different NV–centers, that show coupling to dangling bonds on the diamond surface (no hyperfine components). An oscillation does not emerge on these samples, as there should be no distinct dipolar J coupling in theses spin systems.

Hence, dipolar coupling of MTSSL spins on NP$_{10}$N with a strength of around 6 MHz can be accessed. This result fits very well to what was obtained in section 5.2 using regular EPR methods and what is expected from the molecular structure. It is rather difficult, however, to determine the exact distance between spins from the measurement results, since the relative strength of dipolar coupling terms $J^{\|}$ and $J^{\perp}$ is unclear. Assuming pure parallel coupling J_{zz} and a peptide orientation parallel to the NV-axis for example, the distance between spin labels would be $r = 2.6$ nm. A careful selection of excitation frequencies can give access to the different dipolar coupling components, however due to the low SNR, these measurements were not conducted here.

5.5. Conclusion

Techniques for electron spin resonance on the nanoscale via NV–mangetometry are presented and applied to a common spin labeled peptide.

For the required long term sample stability a key technique was the use of low temperature and ultra high vacuum conditions. It was then shown how to transition from many-spin sampling to the few spin limit by diamagnetic dilution of the samples. There are various other approaches that have been presented in literature, for example covalent attachment [44] to the diamond surface or embedding molecules into a matrix [2], which can, in principle, also be used. Nonetheless the presented technique has the potential to accomplish single molecule or single spin coupling, which is in principle a matter of finding adequate concentration and sampling more NV–centers. It is important to note, that using electronic spins instead of nuclear spins results in a much larger coupling radius and the potential to study systems on a length-scale only limited by the electronic T_2-time, which can be additionally improved by molecular design, e.g. nuclear spin-free solvents or molecules.

A triple resonance scheme allows to furthermore extract the coupling between the molecular spins, which is an important step towards magnetic resonance studies on single molecules.

Although at present it is not possible to precisely extract relevant molecular distances from the measurements, the ease of synthetically predetermining the length of the peptide and the distance between electron spins as well as the number of spins in each peptide directly paves the way for studying length-scales and angles on arbitrary sequences of amino-acids on a single protein basis. This is of practical use in protein structure determination but can also be utilized to engineer molecular-spin networks, with defined interaction strengths between its constituents and a versatile control and read-out mechanism. The presented methods allow for a coherent control of the spin network, which can among other things be utilized for quantum information processing.

6. Summary & Outlook

In this last chapter, the most relevant parts of this thesis are summarized. Furthermore, it is then outlined how the sensitivity of nanoscale electron spin resonance can further be enhanced by the means of technical developments or alternative readout schemes. Also, possible future experiments are discussed to harness this novel sensing capability, mainly with the focus on single molecular structure determination and quantum information processing.

6.1. Summary

This thesis described the usage of single NV–centers in diamond as a magnetic field sensor for electrons in nanoscale volumes. An important progress demonstrated in this work was the detection of less than 10 spins on molecules attached to peptides and the extraction of the coupling in between them using NV–center magnetometry.

Quantum magnetometry with NV–centers

The NV–center consists of a substitutional nitrogen and a nearest-neighbor carbon vacancy in the diamond lattice. Its electronic energy levels lie within the diamond bandgap and are optically accessible. In the NV–center's frequently encountered negative charge state, the electronic ground and first excited state have a spin quantum number of $S = 1$ and a zero field splitting of a few GHz. A non fluorescent intersystem crossing from the electronic first excited state to a singlet state has spin dependent transition probabilities: high for $m_S = \pm 1$, low for $m_S = 0$. Under illumination with light below wavelengths of 637 nm, the emerging NV–center fluorescence is thus dependent on its spin state. Determination (and polarization) of the spin state through fluorescence photon counting enables optically detected magnetic resonance on single NV–centers.

With additional microwave radiation, electron spin resonance on single NV–centers can be performed, with which the positions of the spin sublevels can be determined. Their energy is influenced by environmental magnetic fields via the Zeeman effect. Application of magnetic resonance protocols allows to determine the Zeeman shift from DC- and AC-magnetic fields with a precision that is only limited by the NV–center coherence time T_2 (typically on the order of tens of microseconds). Using different protocols, magnetic fields in a frequency range from DC up to GHz can be detected, with a sensitivity sufficient to detect a single electron spin in several 10 nm or a single nuclear spin in a few nm distance.

This work presents an advancement in electron spin sensing. First, the relevant quantum mechanical framework was introduced with an emphasis on what is important for magnetic sensing applications. For this, dipolar interaction between the NV–center and external magnetic systems takes a central role. Furthermore, numerical simulation methods for magnetic sensing protocols were discussed.

Low temperature and ultra high vacuum setup

Detection of electronic spins with NV–center magnetometry can be challenging due to photobleaching. Since a high laser power of ~ 1 mW is focused to a typical sample volume of ~ 1 µm^3, this energy induces reactions that can lead to a change in spin properties of the sample. The photobleaching effect can be minimized by placing the sample in a low temperature and ultra high vacuum environment. In this thesis, the apparatus to perform NV–center magnetometry under these conditions was key. To boost sensitivity, problems related to optical collection efficiency of the NV–center fluorescence at low temperature had to be overcome. For this, optical waveguides etched in the sample diamonds were incorporated into the setup, increasing the amount of collected photons by an order of magnitude. Additionally, a free configurable magnetic field of 10 mT was realized in the measurement head to perform ESR experiments. This point is crucial since the magnetic field has to be aligned with the NV–center's principal axis for the best measurement performance.

High magnetic field gradients are a possible route to spatial resolution of spins in magnetic resonance imaging. Using an integrated atomic force microscopy stage as a precise positioning tool, samples can be scanned over a single NV–center. It is shown how to determine the magnetic gradient field from an AFM tip with ferromagnetic coating. This is an important step towards future experiments for spatially resolving single spins.

From nanomagnets to single spins

As a first application of the experimental apparatus and NV-center magnetometry on external spin systems, ferritin proteins with a high iron content were studied. These nanomagnets have a magnetic moment of around $300\ \mu_B$, which randomly changes its orientation along an easy axis. The frequency of these magnetic moment reversals depends exponentially on the temperature. Therefore, the spectrum of these fluctuations ranges from GHz at room temperature to below kHz at $T = 5$ K. The experimental setup allows to perform NV–center magnetometry on ferritin ensembles at controlled temperatures. It is first demonstrated, how the fluctuations can be tracked over the whole spectrum using different measurement protocols. Furthermore, the atomic size of the NV–center magnetic field sensor allows to detect signals from individual ferritin molecules using a different sample preparation, that establishes NV–center coupling to only a few molecules.

To sense external electron spins it is beneficial to move to a detection scheme that involves active manipulation of target spins instead of passive fluctuation-sensing. Addressing the target spins with an additional microwave channel results in phase accumulation on the NV–center due to the dipolar coupling of said spin using a double electron electron resonance scheme. This DEER scheme is used to detect electron spins on the clean diamond surface. In this case, the origin of the signal are most likely uncompensated sp^3 bonds on the diamond surface. Depending on their density, such spin systems exhibit various degrees of couplings among each other, which manifests itself in the NV-DEER signal. Limitations to the accessible distances are due to the lifetime T_1 of the external spin state, and how the dipolar coupling strength to the NV–center compares to its T_2 time. The time-limit imposed by the NV–center coherence time T_2 can, however, be overcome by measuring the correlation between two successive DEER sequences. This allows to use the external electron spin itself as a quantum sensor for its environment.

Detection of electrons on a few peptides

To enable the measurement of arbitrary molecules, electron spins can be attached to specific molecular side-groups via site directed spin labeling. This method is applied to a polyproline peptide, which is labeled with two nitroxide spin labels that have a net electron spin of $S = 1/2$. Using large sample quantities (around 10^{12} spins), the distinct dipolar coupling between these two spin labels can be measured in a regular ESR spectrometer. The presented measurements, however, show a large spread due to the different conformations of the two spin labels. To couple the spin labeled peptides with an NV–center, a diamond with shallow NV–centers was coated with peptides via dropcasting. This results in the observation of the NV-DEER spin label signal on virtually all NV–centers. However, this signal is not stable at ambient conditions due to photobleaching.

An unlimited sample stability was demonstrated here, when the sample is cooled to $T = 5$ K in the UHV environment. The NV-DEER signal linewidth also shows significant broadening due to the freeze-out of spin label rotational dynamics at low temperature. The high spin label density gives rise to strong couplings in these samples, resulting in a strongly reduced spin label lifetime T_1.

To demonstrate few spin detection, diamagnetic dilution of spin labeled peptides with unlabeled peptides was used. The NV–center then couples to only a few spin labels. A first indication of this is a spectrum in which single hyperfine contributions of the ^{14}N nucleus in the nitroxide spin label are resolved. In this work we observed for the first time, how this dipolar coupling induces a coherent evolution of the NV–center spin state. The signal evolution can then be used to estimate the number of dipolar coupled spins, which was found to be less or equal to 6 spin labels for a specific NV–center.

The few spin detection limit additionally allows to investigate couplings between the spin labels. Here, a novel sensing scheme was introduced that allows to determine the dipolar coupling of spin labels on the same peptide. This is in principle an extension of the double resonance technique in regular ESR spectroscopy to a sample of only 3 molecules. The determined coupling strength of 5.6 ± 1.0 MHz fits to what was determined by regular ESR spectroscopy. Due to the different components of the dipolar coupling tensor, it is not possible to directly calculate the distance between the two spin labels from this data. However, this would be possible through additional measurements at different magnetic fields.

The application of NV-DEER on highly stable samples directly paves the way for structure determination on single peptides and proteins. Spatial resolution of these single molecular spins is within reach of the current setup due to the already incorporated AFM capabilities. Furthermore, the adjustable coupling between single spins on peptides can be used to investigate quantum information processing. An outlook on this is given in the next sections.

6.2. Improvements in System Performance

6.2.1. Magnetic Field

Although the magnetic fields of around 10 mT currently available in the cryogenic setup are sufficient to perform nanoscale ESR, field strengths two orders of magnitude larger are highly desirable. Higher magnetic field strengths decouple the NV–center from its environment more effectively [191], allow NMR measurements by the detection of statistical polarization using dynamical decoupling schemes (see chapter 2.2.5), and enable single-shot readout of the NV–center nuclear spin [192]. Single-shot readout constitutes a particularly exciting approach, because the spectral resolution can be greatly enhanced through transfer of quantum state from the electron to the nuclear spin [43]. However, first experiments indicate that there are further challenges to overcome when implementing single-shot readout at low temperatures, which are likely connected to the emergent structure of the low temperature excited state NV–center Hamiltonian.

Improvements on the current vector-magnet design can be achieved by using superconducting coils, which would allow for an order of magnitude higher current densities. However, in terms of magnetic field strength a Helmholtz arrangement is usually superior to the design introduced in chapter 3.2. Yet, due to the space limitations of the current measurement head, incorporation of Helmholtz coils is an extremely challenging task. For this reason a reconstruction of the measurement head with high magnetic field strengths in mind seems to be the most suitable approach and is being currently pursued.

6.2.2. Diamond AFM Tips

An emerging approach to scanning NV–magnetometry, unlike the one presented in section 3.3.2, is to use an inverted geometry where the NV–center is mounted on the tuning fork and scanned over arbitrary samples. This is a challenging task for nanofabrication of diamond. A recent example of progress in producing these diamond tips is shown in figure 6.1. Diamond cantilevers containing NV–centers are etched from a thin membrane and contain a single nanopillar [193]. Such diamond cantilevers were already successfully applied to image vortices in superconductors [113] or interface magnetism in thin magnetic films [111]. A demonstration of coherent sensing techniques in this scanning NV-center approach, i.e. conducting nanoscale NMR or ESR experiments has not yet been achieved, due to the poor coherence properties and stability of NV–centers in the diamond cantilevers. This poor coherence is likely caused by lattice defects introduced during etching steps.

While there is great progress in diamond tip fabrication, this geometry is challenging to implement in the current measurement head. Readout of tuning forks is currently only possible in the AFM scanner unit, which is located above the sample and therefore is not optically accessible. A redesign of the cryogenic sample stage is thus recommended, where tip and sample positions will be exchangeable. Using the scanning diamond technique would allow the application of well-established surface preparation techniques,

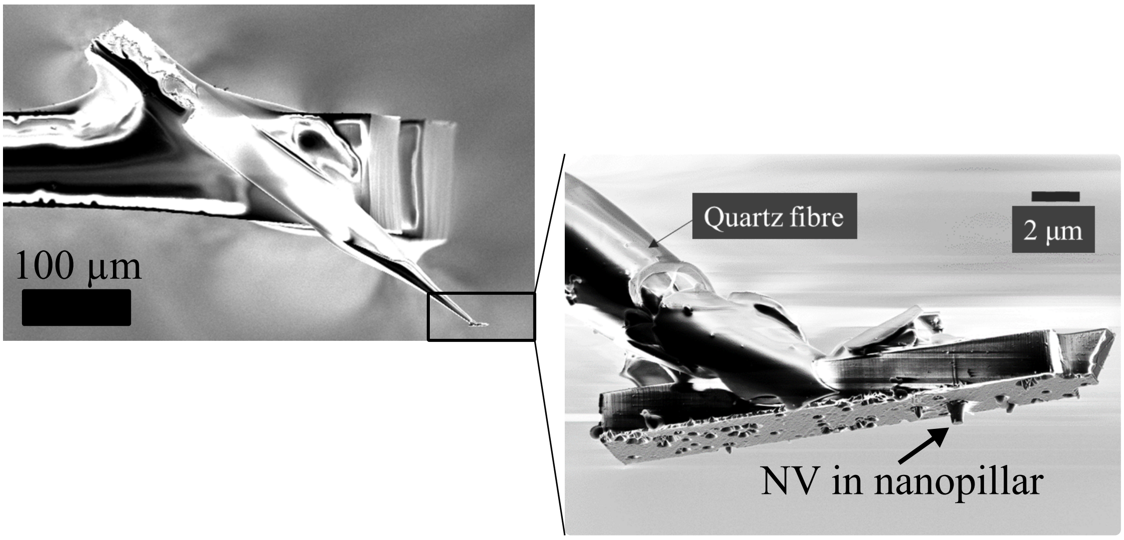

Figure 6.1.: Scanning diamond nanopillar tips containing NV–centers glued to a quartz fiber using a micromanipulator [193].

where atomically flat surfaces are produced in the preparation chamber, on which single molecules can be deposited and subsequently studied in-situ.

6.2.3. In-situ Sample Preparation

Alternatively, the in-situ sample transfer and capabilities in the preparation chamber could enable us to perform epitaxial growth of samples onto the diamond surface. In fact, we have made recent progress in growing thin films of an organic semiconductor, paramagnetic copper phthalocyanine (CuPC) intermixed with its diamagnetic counterpart (HPC) [194], directly onto the diamond surface. We reproduced earlier reported results, where a low concentration of Cu–centers in the otherwise spin-less film revealed comparatively high values in EPR of the electronic $T_1 = 59$ ms and $T_2 = 2.6$ µs respectively [195]. This is shown in figure 6.2, where we deposited a thin film of $\sim 10\%$ CuPC in HPC on a diamond substrate, which shows an island-like growth mode. The measured coherence time $T_2 = 590$ ns of the copper electron spins can be improved by lowering the CuPC/HPC ratio. We can also apply the DEER schemes (see section 4.2) to couple NV–centers to few CuPC spins at low temperatures. With the current magnetic field strength available in the cryogenic measurement head, nonlinear effects like spin state mixing are expected to occur, as the zero field splitting of CuPC electron spins is already around 23 mT [195]. Potentially, this organic semiconductor can serve as a quantum state simulation device, with NV–centers in the underlying diamond as control and readout qubits. It would be particularly interesting to exploit self assembly of molecular networks, which have already been demonstrated for phthalocyanines [196] and could aid in the creation of a regular array of spins. Additionally, the CuPC molecule is an excellent candidate for studying combined nanoscale ESR and NMR methods by NV magnetometry. The copper nuclear magnetic moment and the surrounding hydrogen moments can be addressed simultaneously with its electron spins and their interaction can be studied.

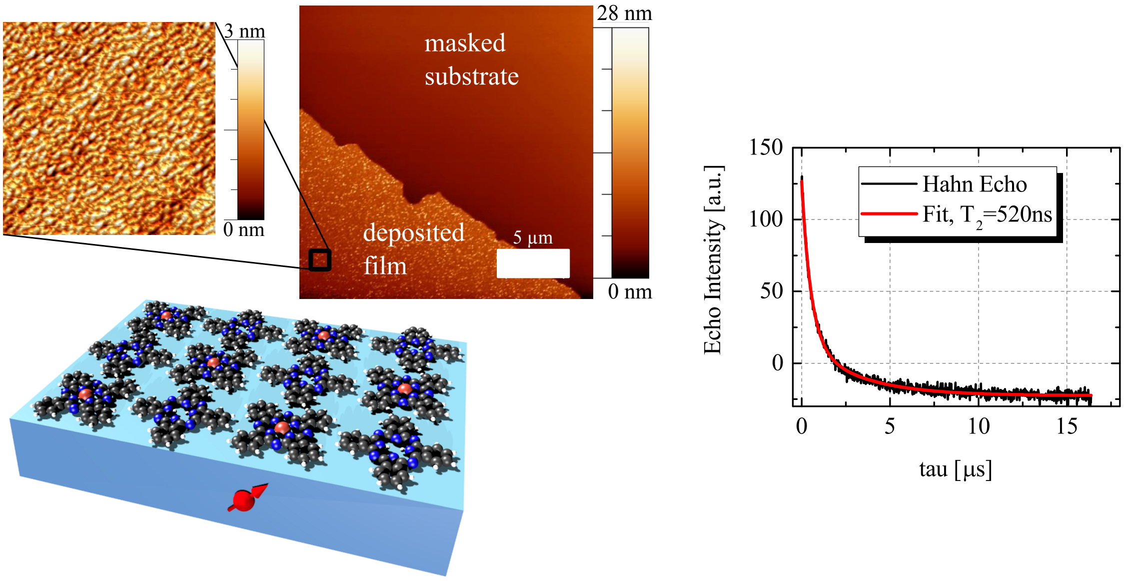

Figure 6.2.: Sketch and AFM measurements of a thin film with composition $\sim 10\%$ CuPC in HPC on diamond [194]. On the right side a EPR Hahn echo measurement of ~ 300 nm of this film grown on a thin quartz plate is presented.

6.3. Spatially Resolving Single Spins

In section 3.3.2, magnetic field gradients from commercial MFM-tips coated with ferromagnetic material were measured. Such gradient fields enable subnanometer spatial resolution of spins, for the first time shown by Grinolds et al. [157]. However, if we consider the proton-limited coherence time for MTSSL spin labels on peptides (section 5.4.1), a much higher magnetic field gradient than 4.5 µT/nm, the value measured in section 3.3.2, is needed. The MTSSL T_2 time of ~ 3 µs (section 5.4.1) suggests a minimum achievable linewidth of 334 kHz. Thus, to achieve a resolution below 1 nm, a magnetic field gradient of 12 µT/nm is required for these spin labels. Note, however, that the actual linewidth measured in the presented experiments is on the order of MHz, since it is limited by T_2^*, which is usually much lower than T_2. Hence a desirable magnetic field gradient should be even an order of magnitude higher. A possible route to such high gradients is to reduce the ferromagnetic film thickness or to restrict the coating to the tip apex. Alternatively, one could test the use of superconducting tips, where the Meissner effect might generate high enough magnetic field gradients.

Using high magnetic field gradients, spin labeling and DEER spectroscopy, it should soon become feasible to study effects like folding on a single protein basis [197]. Additionally, this could open up possibilities to spatially resolve chemical reactions which involve electron spin dynamics, like photosynthesis [198].

Another route to gain spatial information without the help of a scannable sensor, is to vary the angle of applied static magnetic field. Dipolar coupling depends on the orientation Θ of the spin pair to the external magnetic field (see figure 5.8a). Thus, recording the dependence of the dipolar coupling strength on Θ allows to reconstruct the positions of coupled spins [158]. For this approach a well-characterized external magnetic field, as proposed in section 6.2.1 and better SNR are beneficial.

Determination of the dipolar coupling of the external electron spins should allow to reconstruct their distance, as has been done in the regular EPR measurements in section 5.2. This information can be sufficient for example to study structure, dynamics and interactions of proteins in living cells [199]. However, determining the distance from the measured coupling strength in the presented TEER scheme is not straightforward, since both parallel and perpendicular dipolar components contribute to the oscillation. Further developments in the measurement scheme, for example polarizing the external spins by a Hartmann-Hahn approach [200] have to be pursued first. It might then be possible to insert NV–center containing nanodiamonds into a living cell [201] and measure distances of electron spins in-vivo.

6.4. Towards Quantum Spin Networks

The experiments presented in chapter 5 have further implications for the field of quantum information processing. It was shown, that measurement of the long range dipolar coupling in molecular spins with controllable spatial positions [202, 203] is feasible, and thus these techniques can be readily applied to much more complex spin networks. In this respect a large benefit of polypeptide chain molecules is that well defined molecular networks can be produced on large lengthscales with a precision of nanometers, and the spins can be labeled at almost arbitrary positions [204, 205]. The role of the NV–center as a versatile readout tool through dipolar coupling for single spins in such a network has been established here. These readable chains of spins can now be used for the study of quantum phase transitions [206], quantum communication [207, 208] and quantum information transport [209, 210], constituting essential ingredients of a quantum computer.

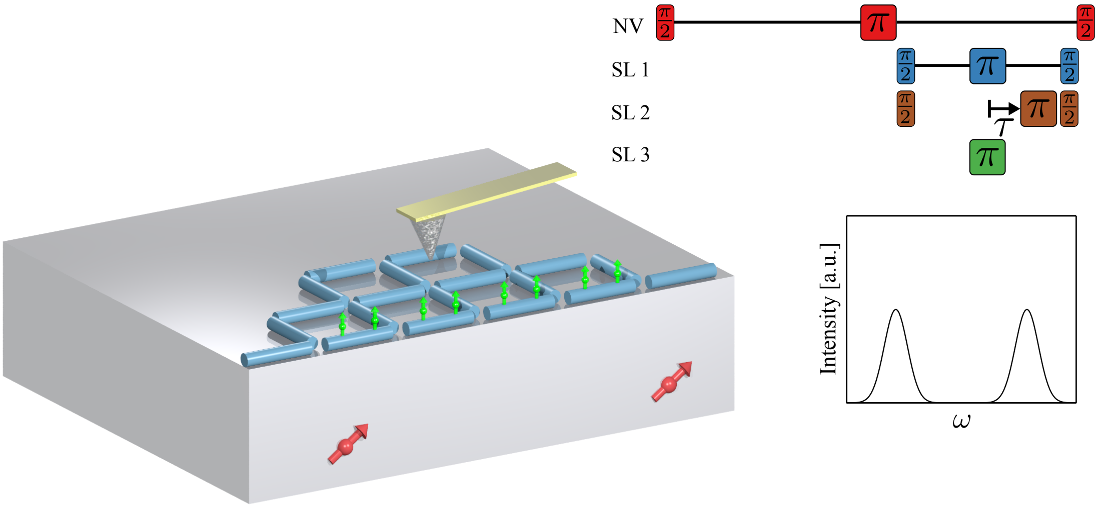

Figure 6.3.: Sketch of a controllable quantum spin network build out of sequenced peptide blocks.

For future experiments, spin lattices from MTSSL labeled polyprolines could be manufactured by ordering the presented P_{10} peptides in a two dimensional network or produce longer polyprolines [169] with more spin labels, as is depicted in figure 6.3. A possible approach to study quantum state transport is to extend the double resonance scheme to more spin labels as it is illustrated in figure 6.3. Alternatively, but much more challenging, one could use a pair of NV–centers separated by a few 10 nm [156, 211], which can be resolved by means of stochastic optical reconstruction microscopy (STORM) [212] or stimulated emission depletion microscopy (STED) [213]. This would allow to study input and output of a single spin chain bus made from MTSSL spin labels. Using the earlier discussed magnetic tips would then furthermore enable to switch dipolar interactions on and off (if $\Delta B > \omega_{dd}$) and thus tune the network coupling to selectively permit communication between single NV–centers.

A. List of Abbreviations

A	Alanine
AC	Alternating current
AFM	Atomic force microscopy
AM	Amplitude modulation
AO	Atomic orbitals
C	Cysteine
CPMG	Carr-Purcell-Meiboom-Gill sequence
CuPC	Copper phthalocyanine
CVD	Chemical vapor deposition
cw	Continuous wave
DC	Direct current
DEER	Double electron electron resonance
DQT	Double quantum transition
EDFS	Echo detected field sweep
EPR	Electron paramagnetic resonance
ES	Excited state
ESEEM	Electron spin echo envelope modulation
ESLAC	Excited state level anticrossing
ESR	Electron spin resonance
FFT	Fast Fourier transform
FID	Free induction decay
FM	Frequency modulation
FPGA	Field-programmable gate array
GPS	Global positioning system
GS	Ground state
GSLAC	Ground state level anticrossing

HPC	Phthalocyanine
HPHT	High pressure high temperature
ISC	Intersystem crossing
LCAO	Linear combination of atomic orbital
MALDI-ToF	Matrix-assisted laser desorption/ionization time-of-flight
MFM	Magnetic force microscopy
MO	Molecular orbital
MRFM	Magnetic resonance force microscopy
MRI	Magnetic resonance imaging
MTSSL	Methanethiosulfonate
NMR	Nuclear magnetic resonance
NV	Nitrogen vacancy
ODMR	Optically detected magnetic resonance
P	proline
SDSL	Site directed spin labeling
SNR	Signal to noise ratio
SS	Spin spin interaction
STED	Stimulated emission depletion microscopy
STORM	Stochastic optical reconstruction microscopy
SO	Spin orbit interaction
SQUID	Superconducting quantum interference device
T_1	Longitudinal relaxation time or lifetime
T_2	Transverse relaxation time or coherence time (Hahn)
T_2^*	Transverse relaxation time or coherence time (FID)
TEER	Triple electron electron resonance
TTL	Transistor-transistor logic
UHV	Ultra high vacuum
UV	ultraviolet
ZPL	Zero phonon line

B. Acknowledgments

The pursuit of a Dr. in physics was truly the toughest, most frustrating, infuriating and in retrospect also the most rewarding thing I have ever done in my whole life. Initially, I did not have any clue how much the topic I was working on over the past four and something years would actually govern my life and thinking during this time and what I would learn from it besides physics. Looking back I am extremely thankful that I was able to complete this path, which had many valleys and detours along the way. I can say with absolute certainty that this would not have been possible without the help I received from many people and here I would like to thank the persons that played a role in the development of this thesis.

First and foremost I want to express my gratitude to Prof. Klaus Kern and Prof. Jörg Wrachtrup for giving me the opportunity to work in this joint project. Although working at the Max-Planck institute for solid state research for most of the time, I have greatly benefited from the distinguished expertise in both their groups. The continuous support I received from them both, as well as their great scientific input has helped me tremendously, especially during tough times.

I cannot express how grateful I am to Amit Finkler. Without his calm supervision and help in whatever aspect, be it in- or outside the lab, this thesis would be nowhere close to where it is now. His broad scientific knowledge, enthusiasm and organizational skills were a constant inspiration to me and I am truly honored to have worked with him. I also want to thank Markus Ternes for supervision and guidance during the project and Friedemann Reinhard for giving me advice and inspiration in the field of NV–center physics, quantum sensing and science in general.

I am thankful to the whole diamond AFM group for the great discussions and projects we had together as well as for making 6C11 a fun place. Eike Oliver Schäfer-Nolte for always having an ingenious technical solution; Thomas White for his great expertise and friendship (and obviously Christmas lab-cleanups along the 90's Mega-Mix); Kebiao Xu for the enlightening discussions about spin physics, programming know-how, and getting me interested in Chinese culture; Felix Weidner for his work on epitaxy in the setup and

Bastian Kern for great scientific input (also by reading this thesis), taking the project to the next level and celebratory whiskey when it was due.

Many of my colleagues have contributed to this work in numerous ways. I would like to especially thank Sebastian Koslowski for his extraordinary friendship, psychological and scientific support and I hope that we will share an office in the near future again. I am indebted to Seyed Ali Momenzadeh for his tremendous work on diamond lithography, which made low temperature measurements in our system possible in the first place. A big thank you goes to Thomas Oeckinghaus, who performed initial room temperature experiments on the nitroxide spins and without whom the whole project would not exist and Durga Bhaktavatsala Rao Dasari for great theoretical support and insight into spin physics. I would like to thank Mykhailo Azarkh and Malte Drescher, who performed most of the regular pulsed EPR in Konstanz and helped me understand it and Andrea Zappe, who prepared the peptides. My deepest gratitude goes to all the members of the 'NV-SPM crew', namely Andreas Brunner, Thomas Haeberle, Thomas Oeckinghaus, Dominik Schmid-Lorch, Kebiao Xu, Anurag Kanase, Philipp Scheiger, Rainer Stöhr and Florestan Ziem. All the enlightening insight and knowledge I gained from discussing and working with all of them has helped me in so many ways I cannot even write them all down. I will definitely miss the awesome weekly meetings we had. I also want to express my gratitude to Matthias Münks, Berthold Jäck, Abhishek Grewal, Claudius Morchutt, Christian Dette, Sabine Abb, Tomasz Michnowicz and Marcel Pristl for all the conversations about science (and its pitfalls) and all the fun we had. Of course, I would also like to thank all the other members of both the nanoscale science department at the MPI for solid state research and the 3rd institute of physics at the University of Stuttgart for their technical help, scientific discussions as well as the fun atmosphere in- and outside the institute.

Last but not least I want to acknowledge the people that were important to me outside the institutes. To my high school physics teacher, Hans Dietrich, who's enthusiasm and excitement about physics lead me to pursue a career as a physicist. To my parents, Sabine and Johannes Schlipf, as well as my three sisters Anna Stolz, Theresa Schlipf and Helena Schlipf and my godmother Helga Jäckel. Without their support in every imaginable way, I would have quit countless times already and I hope I can repay them some day. And finally to my girlfriend Leticia Lima, who never stopped believing in me from the first day we met.

Bibliography

1. Grotz, B. *et al.* Sensing external spins with nitrogen-vacancy diamond. *New J. Phys.* **13,** 055004 (2011) (pages iv, vi, 4, 72).
2. Shi, F. *et al.* Single-protein spin resonance spectroscopy under ambient conditions. *Science* **347,** 1135–1138 (2015) (pages iv, vi, 4, 82, 95, 115).
3. Friedrich, B. & Herschbach, D. Stern and Gerlach: How a Bad Cigar Helped Reorient Atomic Physics. *Physics Today* **56,** 53–59 (2003) (page 1).
4. Chappert, C., Fert, A. & Van Dau, F. N. The emergence of spin electronics in data storage. *Nat Mater* **6,** 813–823 (Nov. 2007) (page 1).
5. Nielsen, M. A. & Chuang, I. L. *Quantum Computation and Quantum Information* (Cambridge University Press, 2010) (page 1).
6. Ladd, T. D. *et al.* Quantum computers. *Nature* **464,** 45–53 (Mar. 2010) (page 1).
7. Mittermaier, A. K. & Kay, L. E. Observing biological dynamics at atomic resolution using NMR. *Trends in Biochemical Sciences* **34,** 601 –611 (2009) (page 2).
8. Colvin, M. T. *et al.* Atomic Resolution Structure of Monomorphic Aβ42 Amyloid Fibrils. *Journal of the American Chemical Society* **138.** PMID: 27355699, 9663–9674 (2016) (page 2).
9. Wälti, M. A. *et al.* Atomic-resolution structure of a disease-relevant Aβ(1–42) amyloid fibril. *Proceedings of the National Academy of Sciences* **113,** E4976–E4984 (2016) (page 2).
10. Tycko, R. Alzheimer's disease: Structure of aggregates revealed. *Nature* **537,** 492–493 (Sept. 2016) (page 2).
11. Fatahi, M. *et al.* DNA double-strand breaks and micronuclei in human blood lymphocytes after repeated whole body exposures to 7T Magnetic Resonance Imaging. *NeuroImage* **133,** 288 –293 (2016) (page 2).

12. Seeber, D. A., Hoftiezer, J. H., Daniel, W. B., Rutgers, M. A. & Pennington, C. H. Triaxial magnetic field gradient system for microcoil magnetic resonance imaging. *Review of Scientific Instruments* **71,** 4263–4272 (2000) (page 2).
13. Glover, P. & Mansfield, S. P. Limits to magnetic resonance microscopy. *Reports on Progress in Physics* **65,** 1489 (2002) (page 2).
14. Rugar, D., Budakian, R., Mamin, H. J. & Chui, B. W. Single spin detection by magnetic resonance force microscopy. *Nature* **430,** 329–332 (2004) (pages 2, 81).
15. Baumann, S. *et al.* Electron paramagnetic resonance of individual atoms on a surface. *Science* **350,** 417–420 (2015) (page 3).
16. Degen, C. L., Reinhard, F. & Cappellaro, P. Quantum sensing. *Rev. Mod. Phys.* **89,** 035002 (2017) (pages 3, 5, 35).
17. Budker, D. & Romalis, M. Optical magnetometry. *Nat Phys* **3,** 227–234 (Apr. 2007) (page 3).
18. Shah, V., Knappe, S., Schwindt, P. D. D. & Kitching, J. Subpicotesla atomic magnetometry with a microfabricated vapour cell. *Nat Photon* **1,** 649–652 (Nov. 2007) (page 3).
19. Ockeloen, C. F., Schmied, R., Riedel, M. F. & Treutlein, P. Quantum Metrology with a Scanning Probe Atom Interferometer. *Phys. Rev. Lett.* **111,** 143001 (14 2013) (page 3).
20. Huntemann, N., Sanner, C., Lipphardt, B., Tamm, C. & Peik, E. Single-Ion Atomic Clock with 3×10^{-18} Systematic Uncertainty. *Phys. Rev. Lett.* **116,** 063001 (6 2016) (page 3).
21. Simmonds, M., Fertig, W. & Giffard, R. Performance of a resonant input SQUID amplifier system. *IEEE Transactions on Magnetics* **15,** 478–481 (1979) (page 3).
22. Finkler, A. *et al.* Self-Aligned Nanoscale SQUID on a Tip. *Nano Letters* **10.** PMID: 20131810, 1046–1049 (2010) (page 3).
23. Vasyukov, D. *et al.* A scanning superconducting quantum interference device with single electron spin sensitivity. *Nat. Nanotechnol.* **8,** 639–644 (2013) (page 3).
24. Halbertal, D. *et al.* Nanoscale thermal imaging of dissipation in quantum systems. *Nature* **539,** 407–410 (Nov. 2016) (page 3).
25. Morello, A. *et al.* Single-shot readout of an electron spin in silicon. *Nature* **467,** 687–691 (Oct. 2010) (page 4).

26. Elzerman, J. M. *et al.* Single-shot read-out of an individual electron spin in a quantum dot. *Nature* **430,** 431–435 (July 2004) (page 4).

27. Vamivakas, A. N. *et al.* Observation of spin-dependent quantum jumps via quantum dot resonance fluorescence. *Nature* **467,** 297–300 (Sept. 2010) (page 4).

28. Wrachtrup, J., von Borczyskowski, C., Bernard, J., Orritt, M. & Brown, R. Optical detection of magnetic resonance in a single molecule. *Nature* **363,** 244–245 (May 1993) (page 4).

29. Gruber, A. *et al.* Scanning Confocal Optical Microscopy and Magnetic Resonance on Single Defect Centers. *Science* **276,** 2012–2014 (1997) (pages 4, 17, 52).

30. Wrachtrup, J. & Jelezko, F. Processing quantum information in diamond. *Journal of Physics: Condensed Matter* **18,** S807–S824 (2006) (pages 4, 22).

31. Maze, J. R. *et al.* Nanoscale magnetic sensing with an individual electronic spin in diamond. *Nature* **455,** 644 (2008) (page 4).

32. Balasubramanian, G. *et al.* Nanoscale imaging magnetometry with diamond spins under ambient conditions. *Nature* **455,** 648 (2008) (pages 4, 5).

33. Dolde, F. *et al.* Electric-field sensing using single diamond spins. *Nat. Phys.* **7,** 459 (June 2011) (page 4).

34. Doherty, M. W. *et al.* Electronic Properties and Metrology Applications of the Diamond NV$^-$ Center under Pressure. *Phys. Rev. Lett.* **112,** 047601 (4 2014) (page 4).

35. Neumann, P. *et al.* High-Precision Nanoscale Temperature Sensing Using Single Defects in Diamond. *Nano Lett.* **13,** 2738–2742 (2013) (page 4).

36. Balasubramanian, G. *et al.* Ultralong spin coherence time in isotopically engineered diamond. *Nat. Mater.* **8,** 383 (2009) (pages 4, 25, 37, 39).

37. Taylor, J. M. *et al.* High-sensitivity diamond magnetometer with nanoscale resolution. *Nat. Phys.* **4,** 810–816 (2008) (pages 4, 36).

38. Ohno, K. *et al.* Engineering shallow spins in diamond with nitrogen delta-doping. *Applied Physics Letters* **101,** 082413 (2012) (pages 4, 10).

39. Staudacher, T. *et al.* Nuclear Magnetic Resonance Spectroscopy on a (5-Nanometer)^3 Sample Volume. *Science* **339,** 561–563 (2013) (pages 4, 39).

40. Mamin, H. J. *et al.* Nanoscale Nuclear Magnetic Resonance with a Nitrogen-Vacancy Spin Sensor. *Science* **339,** 557–560 (2013) (pages 4, 39).

41. Mamin, H. J., Sherwood, M. H. & Rugar, D. Detecting external electron spins using nitrogen-vacancy centers. *Phys. Rev. B* **86,** 195422 (19 2012) (pages 4, 72).
42. Grinolds, M. S. *et al.* Nanoscale magnetic imaging of a single electron spin under ambient conditions. *Nat. Phys.* **9,** 215–219 (2013) (page 4).
43. Aslam, N. *et al.* Nanoscale nuclear magnetic resonance with chemical resolution. *Science.* eprint: `http://science.sciencemag.org/content/early/2017/05/31/science.aam8697.full.pdf` (2017) (pages 4, 34, 75, 121).
44. Lovchinsky, I. *et al.* Nuclear magnetic resonance detection and spectroscopy of single proteins using quantum logic. *Science* **351,** 836–841 (2016) (pages 4, 39, 103, 115).
45. Rondin, L. *et al.* Nanoscale magnetic field mapping with a single spin scanning probe magnetometer. *Appl. Phys. Lett* **100,** 153118 (2012) (page 5).
46. Maletinsky, P. *et al.* A robust scanning diamond sensor for nanoscale imaging with single nitrogen-vacancy centres. *Nature Nanotech.* **7,** 320 (2012) (page 5).
47. Appel, P. *et al.* Fabrication of all diamond scanning probes for nanoscale magnetometry. *Rev. Sci. Instrum.* **87** (2016) (page 5).
48. Rondin, L *et al.* Magnetometry with nitrogen-vacancy defects in diamond. *Rep. Prog. Phys.* **77,** 056503 (2014) (pages 5, 36, 39).
49. Maletinsky, P. & Jacques, V. in *Quantum Information Processing with Diamond* (eds Prawer, S. & Aharonovich, I.) 240 –263 (Woodhead Publishing, 2014) (pages 5, 37).
50. Gogotsi, Y. G., Kailer, A. & Nickel, K. G. Materials: Transformation of diamond to graphite. *Nature* **401,** 663–664 (Oct. 1999) (page 7).
51. Hershey, J. W. *The Book of Diamonds* **12,** 142. eprint: `http://dx.doi.org/10.1021/ed017p600.2` (Hearthside press, New York, 1940) (page 7).
52. Bhagavantam, S. & Bhimasenachar, J. Elastic Constants of Diamond. *Proceedings of the Royal Society of London. Series A, Mathematical and Physical Sciences* **187,** 381–384 (1946) (page 7).
53. *Synthetic Diamond: Emerging CVD Science and Technology* (eds Spear, K. E. & Dismukes, J. P.) (John Wiley& Sons, Inc., 1994) (page 7).
54. Spiegel. *Rosaroter Klunker für Rekordpreis versteigert* Online. Apr. 2017 (page 7).
55. Lončar, M. & Faraon, A. Quantum photonic networks in diamond. *MRS Bulletin* **38,** 144–148 (Feb. 2013) (page 8).

56. Le Sage, D. *et al.* Optical magnetic imaging of living cells. *Nature* **496,** 486 (2013) (page 8).
57. Seo, J.-H. *et al.* Thermal diffusion boron doping of single-crystal natural diamond. *Journal of Applied Physics* **119,** 205703 (2016) (page 8).
58. Walker, J. Optical absorption and luminescence in diamond. *Rep.Prog. Phys.* **42,** 1606–1659 (1979) (page 8).
59. Akaishi, M., Kanda, H. & Yamaoka, S. High Pressure Synthesis of Diamond in the Systems of Grahpite-Sulfate and Graphite-Hydroxide. *Japanese Journal of Applied Physics* **29,** L1172 (1990) (page 9).
60. Gracio, J. J., Fan, Q. H. & Madaleno, J. C. Diamond growth by chemical vapour deposition. *Journal of Physics D: Applied Physics* **43,** 374017 (2010) (page 9).
61. Zaitsev, A. M. *Optical Properties of Diamond* (Springer-Verlag Berlin Heidelberg GmbH, 2001) (page 9).
62. Preez, L. D. *Electron paramagnetic resonance and optical investigations of defect centres in diamond* PhD thesis (University of the Witwatersrand, Science Faculty (Physics), 1965) (page 10).
63. Loubser, J. H. N. & van Wyk, J. A. Optical spin-polarisation in a triplet state in irradiated and annealed type 1b diamonds. *Diamond Research,* 11–14 (1977) (pages 10, 14).
64. Loubser, J. H. N. & van Wyk, J. A. Electron spin resonance in the study of diamond. *Reports on Progress in Physics* **41,** 1201 (1978) (page 10).
65. Santori, C., Barclay, P. E., Fu, K.-M. C. & Beausoleil, R. G. Vertical distribution of nitrogen-vacancy centers in diamond formed by ion implantation and annealing. *Phys. Rev. B* **79,** 125313 (12 2009) (page 10).
66. Pezzagna, S, Naydenov, B, Jelezko, F, Wrachtrup, J & Meijer, J. Creation efficiency of nitrogen-vacancy centres in diamond. *New Journal of Physics* **12,** 065017 (2010) (pages 10, 91).
67. Born, M. & Oppenheimer, R. Zur Quantentheorie der Molekeln. *Annalen der Physik* **389,** 457–484 (1927) (page 11).
68. Doherty, M. W. *et al.* Theory of the ground-state spin of the NV- center in diamond. *Phys. Rev. B* **85,** 205203 (20 2012) (pages 11, 41).
69. Dresselhaus, M., Dresselhaus, G. & Jorio, A. *Group Theory: Application to the Physics of Condensed Matter* (Springer, 2007) (page 11).

70. Goss, J. P., Jones, R., Breuer, S. J., Briddon, P. R. & Öberg, S. The Twelve-Line 1.682 eV Luminescence Center in Diamond and the Vacancy-Silicon Complex. *Phys. Rev. Lett.* **77,** 3041–3044 (14 1996) (page 11).

71. Gali, A., Fyta, M. & Kaxiras, E. Ab initio supercell calculations on nitrogen-vacancy center in diamond: Electronic structure and hyperfine tensors. *Phys. Rev. B* **77,** 155206 (15 2008) (page 11).

72. Doherty, M. W., Manson, N. B., Delaney, P & Hollenberg, L. C. L. The negatively charged nitrogen-vacancy centre in diamond: the electronic solution. *New Journal of Physics* **13,** 025019 (2011) (pages 12, 14).

73. Hauf, M. V. *et al.* Chemical control of the charge state of nitrogen-vacancy centers in diamond. *Phys. Rev. B* **83,** 081304 (8 2011) (page 12).

74. Pfender, M. *et al.* Protecting a diamond quantum memory by charge state control. arXiv: `1702.01590 [quant-ph]` (2017) (page 12).

75. Mita, Y. Change of absorption spectra in type-Ib diamond with heavy neutron irradiation. *Phys. Rev. B* **53,** 11360–11364 (17 1996) (page 13).

76. Aslam, N, Waldherr, G, Neumann, P, Jelezko, F & Wrachtrup, J. Photo-induced ionization dynamics of the nitrogen vacancy defect in diamond investigated by single-shot charge state detection. *New J. Phys.* **15,** 013064 (2013) (pages 13, 16).

77. Lee, S.-Y. *et al.* Readout and control of a single nuclear spin with a metastable electron spin ancilla. *Nat. Nanotech.* **8,** 487–492 (July 2013) (page 13).

78. Rogers, L. *et al.* Multiple intrinsically identical single-photon emitters in the solid state. *Nat. Commun.* **5s,** – (Aug. 2014) (page 13).

79. Widmann, M. *et al.* Coherent control of single spins in silicon carbide at room temperature. *Nat. Mater.* **14,** 164–168 (Dec. 2014) (page 13).

80. Chatzidrosos, G. *et al.* Protecting a diamond quantum memory by charge state control. arXiv: `1706.02201 [quant-ph]` (2017) (page 13).

81. Manson, N. B., Harrison, J. P. & Sellars, M. J. Nitrogen-vacancy center in diamond: Model of the electronic structure and associated dynamics. *Phys. Rev. B* **74,** 104303 (10 2006) (page 14).

82. Felton, S. *et al.* Hyperfine interaction in the ground state of the negatively charged nitrogen vacancy center in diamond. *Phys. Rev. B* **79,** 075203 (7 2009) (page 14).

83. Doherty, M. W. *et al.* The nitrogen-vacancy colour centre in diamond. *Phys. Rep.* **528.** The nitrogen-vacancy colour centre in diamond, 1 –45 (2013) (pages 14, 16, 40).
84. Acosta, V. M., Jarmola, A., Bauch, E. & Budker, D. Optical properties of the nitrogen-vacancy singlet levels in diamond. *Phys. Rev. B* **82,** 201202 (20 2010) (page 14).
85. Batalov, A. *et al.* Low Temperature Studies of the Excited-State Structure of Negatively Charged Nitrogen-Vacancy Color Centers in Diamond. *Phys. Rev. Lett.* **102,** 195506 (19 2009) (pages 14, 40).
86. Rogers, L. J., McMurtrie, R. L., Sellars, M. J. & Manson, N. B. Time-averaging within the excited state of the nitrogen-vacancy centre in diamond. *New Journal of Physics* **11,** 063007 (2009) (page 14).
87. Fuchs, G. D. *et al.* Excited-State Spectroscopy Using Single Spin Manipulation in Diamond. *Phys. Rev. Lett.* **101,** 117601 (11 2008) (page 14).
88. Batalov, A. *et al.* Temporal Coherence of Photons Emitted by Single Nitrogen-Vacancy Defect Centers in Diamond Using Optical Rabi-Oscillations. *Phys. Rev. Lett.* **100,** 077401 (7 2008) (page 16).
89. Harrison, J, Sellars, M. & Manson, N. Optical spin polarisation of the N-V centre in diamond. *Journal of Luminescence* **107.** Proceedings of the 8th International Meeting on Hole Burning, Single Molecule, and Related Spectroscopies: Science and Applications, 245 –248 (2004) (page 16).
90. Harrison, J., Sellars, M. & Manson, N. Measurement of the optically induced spin polarisation of N-V centres in diamond. *Diamond and Related Materials* **15.** Diamond 2005Proceedings of Diamond 2005, the 16th European Conference on Diamond, Diamond-Like Materials, Carbon Nanotubes, Nitrides & Silicon Carbide, 586 –588 (2006) (page 17).
91. Brossel, J. & Bitter, F. A New "Double Resonance" Method for Investigating Atomic Energy Levels. Application to Hg^3P_1. *Phys. Rev.* **86,** 308–316 (3 1952) (page 17).
92. Cavenett, B. Optically detected magnetic resonance (O.D.M.R.) investigations of recombination processes in semiconductors. *Advances in Physics* **30,** 475–538 (1981) (page 17).
93. Chen, W. M. Applications of optically detected magnetic resonance in semiconductor layered structures. *Thin Solid Films* **364,** 45 –52 (2000) (page 17).

94. Dréau, A. *et al.* Avoiding power broadening in optically detected magnetic resonance of single NV defects for enhanced dc magnetic field sensitivity. *Phys. Rev. B* **84,** 195204 (19 2011) (page 21).
95. Neumann, P. *Towards a room temperature solid state quantum processor — The nitrogen-vacancy center in diamond* PhD thesis (3. Physikalisches Institut, Universität Stuttgart, 2011) (page 22).
96. Zaiser, S. *et al.* Enhancing quantum sensing sensitivity by a quantum memory. *Nat. Commun.* **7** (2016) (pages 22, 75).
97. Levitt, M. H. *Spin Dynamics: Basics of Nuclear Magnetic Resonance, 2nd Edition* (John Wiley & Sons, Ltd, 2008) (pages 23, 40).
98. Jarmola, A., Acosta, V. M., Jensen, K., Chemerisov, S. & Budker, D. Temperature- and Magnetic-Field-Dependent Longitudinal Spin Relaxation in Nitrogen-Vacancy Ensembles in Diamond. *Phys. Rev. Lett.* **108,** 197601 (19 2012) (pages 25, 65).
99. Häberle, T. *Nanoscale Magnetic Resonance Imaging* PhD thesis (3. Physikalisches Institut der Universität Stuttgart, Jan. 18, 2017) (pages 30, 49).
100. Hahn, E. L. Spin Echoes. *Phys. Rev.* **80,** 580–594 (4 1950) (page 31).
101. Wang, Z.-H. & Takahashi, S. Spin decoherence and electron spin bath noise of a nitrogen-vacancy center in diamond. *Physical Review B* **87** (2013) (page 33).
102. Luan, L. *et al.* Decoherence imaging of spin ensembles using a scanning single-electron spin in diamond. *Sci. Rep.* **5,** 8119 (2015) (page 33).
103. Carr, H. Y. & Purcell, E. M. Effects of Diffusion on Free Precession in Nuclear Magnetic Resonance Experiments. *Phys. Rev.* **94,** 630–638 (3 1954) (page 34).
104. Wang, Z.-H., de Lange, G., Ristè, D., Hanson, R. & Dobrovitski, V. V. Comparison of dynamical decoupling protocols for a nitrogen-vacancy center in diamond. *Phys. Rev. B* **85,** 155204 (15 2012) (page 34).
105. Viola, L., Knill, E. & Lloyd, S. Dynamical Decoupling of Open Quantum Systems. *Phys. Rev. Lett.* **82,** 2417–2421 (12 1999) (page 34).
106. Nöbauer, T. *et al.* Smooth Optimal Quantum Control for Robust Solid-State Spin Magnetometry. *Phys. Rev. Lett.* **115,** 190801 (19 2015) (page 34).
107. Pfender, M. *et al.* Nonvolatile quantum memory enables sensor unlimited nanoscale spectroscopy of finite quantum systems. eprint: `1610.05675` (Oct. 2016) (page 34).
108. Rosskopf, T., Zopes, J., Boss, J. M. & Degen, C. L. A quantum spectrum analyzer enhanced by a nuclear spin memory. eprint: `1610.03253` (Oct. 2016) (page 34).

109. Ishikawa, T. *et al.* Optical and Spin Coherence Properties of Nitrogen-Vacancy Centers Placed in a 100 nm Thick Isotopically Purified Diamond Layer. *Nano Letters* **12.** PMID: 22404419, 2083–2087 (2012) (page 36).

110. Tetienne, J.-P. *et al.* Nanoscale imaging and control of domain-wall hopping with a nitrogen-vacancy center microscope. *Science* **344,** 1366–1369 (2014) (page 37).

111. Gross, I. *et al.* Direct measurement of interfacial Dzyaloshinskii-Moriya interaction in $X|\text{CoFeB}|\text{MgO}$ heterostructures with a scanning NV magnetometer $(X = \text{Ta}, \text{TaN}, \text{and W})$. *Phys. Rev. B* **94,** 064413 (6 2016) (pages 37, 121).

112. Kosub, T. *et al.* Purely antiferromagnetic magnetoelectric random access memory. *Nat. Commun.* **8,** 13985 (2017) (page 37).

113. Thiel, L. *et al.* Quantitative nanoscale vortex imaging using a cryogenic quantum magnetometer. *Nat. Nanotechnol.* **11,** 677–681 (May 2016) (pages 37, 121).

114. Pelliccione, M. *et al.* Scanned probe imaging of nanoscale magnetism at cryogenic temperatures with a single-spin quantum sensor. *Nat. Nanotechnol.* **advance online publication** (May 2016) (page 37).

115. Tetienne, J.-P. *et al.* Quantum imaging of current flow in graphene. *Sci. Adv.* **3** (2017) (page 37).

116. Cole, J. H. & Hollenberg, L. C. L. Scanning quantum decoherence microscopy. *Nanotechnology* **20,** 495401 (2009) (page 37).

117. Hall, L. T., Cole, J. H., Hill, C. D. & Hollenberg, L. C. L. Sensing of Fluctuating Nanoscale Magnetic Fields Using Nitrogen-Vacancy Centers in Diamond. *Phys. Rev. Lett.* **103,** 220802 (22 2009) (page 37).

118. Steinert, S. *et al.* Magnetic spin imaging under ambient conditions with sub-cellular resolution. *Nat. Commun.* **4,** 1607 (Mar. 2013) (page 37).

119. Ziem, F. C., Götz, N. S., Zappe, A., Steinert, S. & Wrachtrup, J. Highly Sensitive Detection of Physiological Spins in a Microfluidic Device. *Nano Lett.* **13,** 4093–4098 (2013) (pages 37, 66).

120. Ermakova, A. *et al.* Detection of a Few Metallo-Protein Molecules Using Color Centers in Nanodiamonds. *Nano Lett.* **13.** PMID: 23738579, 3305–3309 (2013) (pages 37, 66).

121. Schmid-Lorch, D. *et al.* Relaxometry and Dephasing Imaging of Superparamagnetic Magnetite Nanoparticles Using a Single Qubit. *Nano Lett.* **15,** 4942–4947 (2015) (page 37).

122. Pelliccione, M., Myers, B. A., Pascal, L. M. A., Das, A. & Bleszynski Jayich, A. C. Two-Dimensional Nanoscale Imaging of Gadolinium Spins via Scanning Probe Relaxometry with a Single Spin in Diamond. *Phys. Rev. Applied* **2,** 054014 (5 2014) (page 37).

123. Tetienne, J.-P. *et al.* Spin relaxometry of single nitrogen-vacancy defects in diamond nanocrystals for magnetic noise sensing. *Phys. Rev. B* **87,** 235436 (23 2013) (page 37).

124. Rosskopf, T. *et al.* Investigation of Surface Magnetic Noise by Shallow Spins in Diamond. *Phys. Rev. Lett.* **112,** 147602 (14 2014) (page 37).

125. Wood, J. D. A. *et al.* Microwave-Free Nuclear Magnetic Resonance at Molecular Scales. arXiv: `1610.01737v1 [cond-mat.mes-hall]` (Oct. 6, 2016) (pages 37, 38).

126. Sushkov, A. O. *et al.* All-Optical Sensing of a Single-Molecule Electron Spin. *Nano Letters* **14,** 6443 (2014) (pages 38, 103).

127. Wood, J. D. A. *et al.* Wide-band, nanoscale magnetic resonance spectroscopy using quantum relaxation of a single spin in diamond. *Phys. Rev. B* **94.** eprint: `1604.00160` (Apr. 2016) (page 38).

128. Hanson, R., Dobrovitski, V. V., Feiguin, A. E., Gywat, O. & Awschalom, D. D. Coherent Dynamics of a Single Spin Interacting with an Adjustable Spin Bath. *Science* **320,** 352–355 (2008) (page 38).

129. Abragam, A. & Pryce, M. H. L. Theory of the Nuclear Hyperfine Structure of Paramagnetic Resonance Spectra in Crystals. *Proceedings of the Royal Society of London A: Mathematical, Physical and Engineering Sciences* **205,** 135–153 (1951) (page 40).

130. Schweiger, A. & Jeschke, G. *Principles of Pulse Electron Paramagnetic Resonance* (Oxford University Press, 2001) (pages 40, 44).

131. Gatteschi, D., Sessoli, R. & Villain, J. *Molecular Nanomagnets* (Oxford University Press, 2006) (page 40).

132. Neumann, P *et al.* Excited-state spectroscopy of single NV defects in diamond using optically detected magnetic resonance. *New J. Phys.* **11,** 013017 (2009) (page 40).

133. He, X.-F., Manson, N. B. & Fisk, P. T. H. Paramagnetic resonance of photoexcited N-V defects in diamond. II. Hyperfine interaction with the $^{14}\mathrm{N}$ nucleus. *Phys. Rev. B* **47,** 8816–8822 (14 1993) (page 40).
134. Rempp, F. *Decoherence properties of the NV-center in diamond* PhD thesis (University of Stuttgart, 2011) (page 42).
135. Johansson, J., Nation, P. & Nori, F. QuTiP 2: A Python framework for the dynamics of open quantum systems. *Computer Physics Communications* **184,** 1234 –1240 (2013) (page 45).
136. Schäfer-Nolte, E.-O. *Development of a Diamond-based Scanning Probe Spin Sensor Operating at Low Temperature in Ultra High Vacuum* PhD thesis (University of Stuttgart, 2014) (pages 49, 52, 61).
137. Schäfer-Nolte, E., Reinhard, F., Ternes, M., Wrachtrup, J. & Kern, K. A diamond-based scanning probe spin sensor operating at low temperature in ultra-high vacuum. *Rev. Sci. Instrum.* **85,** 013701 (2014) (page 49).
138. Giessibl, F. J., Hembacher, S, Herz, M, Schiller, C. & Mannhart, J. Stability considerations and implementation of cantilevers allowing dynamic force microscopy with optimal resolution: the qPlus sensor. *Nanotechnology* **15,** S79 (2004) (page 51).
139. Momenzadeh, S. A. *et al.* Nanoengineered Diamond Waveguide as a Robust Bright Platform for Nanomagnetometry Using Shallow Nitrogen Vacancy Centers. *Nano Lett.* **15,** 165–169 (2015) (pages 53, 65, 92).
140. Häberle, T. *et al.* Nuclear Quantum-Assisted Magnetometer. *Rev. Sci. Instrum.* **88,** 013702 (Oct. 12, 2016) (page 54).
141. Tetienne, J.-P. *et al.* Magnetic-field-dependent photodynamics of single NV defects in diamond: an application to qualitative all-optical magnetic imaging. *New J. Phys.* **14,** 103033 (2012) (pages 56, 100).
142. Mamin, H. J., Rettner, C. T., Sherwood, M. H., Gao, L. & Rugar, D. High field-gradient dysprosium tips for magnetic resonance force microscopy. *Appl. Phys. Lett.* **100,** 013102 (2012) (page 58).
143. Häberle, T., Schmid-Lorch, D., Karrai, K., Reinhard, F. & Wrachtrup, J. High-Dynamic-Range Imaging of Nanoscale Magnetic Fields Using Optimal Control of a Single Qubit. *Phys. Rev. Lett.* **111,** 170801 (17 2013) (page 58).

144. Schäfer-Nolte, E. *et al.* Tracking Temperature Dependent Relaxation Times of Individual Ferritin Nanomagnets with a Wide-band Quantum Spectrometer. *Phys. Rev. Lett.* **113,** 217204 (2014) (page 61).

145. Munro, H. N. & Linder, M. C. Ferritin: structure, biosynthesis, and role in iron metabolism. *Physiological Reviews* **58,** 317–396 (1978) (page 61).

146. Theil, E. C. Ferritin protein nanocages–the story. *Nanotechnology perceptions* **8,** 7–16 (2012) (page 62).

147. Bauminger, E. R. & Nowik, I. Magnetism in plant and mammalian ferritin. *Hyperfine Interactions* **50,** 489–497 (1989) (page 62).

148. Gilles, C. *et al.* Magnetic hysteresis and superantiferromagnetism in ferritin nanoparticles. *Journal of Magnetism and Magnetic Materials* **241,** 430 –440 (2002) (page 62).

149. Papaefthymiou, G. C. The Mössbauer and magnetic properties of ferritin cores. *Biochimica et Biophysica Acta (BBA) - General Subjects* **1800.** Ferritin: Structures, Properties and Applications, 886 –897 (2010) (page 62).

150. Mørup, S., Madsen, D. E., Frandsen, C., Bahl, C. R. H. & Hansen, M. F. Experimental and theoretical studies of nanoparticles of antiferromagnetic materials. *Journal of Physics: Condensed Matter* **19,** 213202 (2007) (page 62).

151. Wajnberg, E., El-Jaick, L. J., Linhares, M. P. & Esquivel, D. M. Ferromagnetic Resonance of Horse Spleen Ferritin: Core Blocking and Surface Ordering Temperatures. *Journal of Magnetic Resonance* **153,** 69 –74 (2001) (page 62).

152. Madsen, D. E., Hansen, M. F. & Mørup, S. The correlation between superparamagnetic blocking temperatures and peak temperatures obtained from ac magnetization measurements. *Journal of Physics: Condensed Matter* **20,** 345209 (2008) (page 64).

153. Madsen, D. E., Hansen, M. F., Bendix, J & Mørup, S. On the analysis of magnetization and Mössbauer data for ferritin. *Nanotechnology* **19,** 315712 (2008) (page 66).

154. Milov, A. D., Salikhov, K. M. & Shirov, M. D. Application of ELDOR in electron-spin echo for paramagnetic center space distribution in solids. *Fiz. Tverd. Tela* **23,** 975–982 (1981) (page 70).

155. De Lange, G. *et al.* Controlling the quantum dynamics of a mesoscopic spin bath in diamond. *Scientific Reports* **2,** 382– (Apr. 2012) (page 72).

156. Neumann, P. *et al.* Quantum register based on coupled electron spins in a room-temperature solid. *Nat. Phys.* **6,** 249 (2010) (pages 72, 125).

157. Grinolds, M. S. *et al.* Subnanometre resolution in three-dimensional magnetic resonance imaging of individual dark spins. *Nat. Nanotechnol.* **9,** 279–284 (Apr. 2014) (pages 72, 123).

158. Sushkov, A. O. *et al.* Magnetic Resonance Detection of Individual Proton Spins Using Quantum Reporters. *Phys. Rev. Lett.* **113,** 197601 (19 2014) (pages 72, 75, 77, 124).

159. Laraoui, A. *et al.* High-resolution correlation spectroscopy of ^{13}C spins near a nitrogen-vacancy centre in diamond. *Nat. Commun.* **4,** 1651 (Apr. 2013) (pages 75, 76, 111).

160. Cross, T. A. & Opella, S. J. Protein structure by solid-state NMR. *J. Am. Chem. Soc.* **105,** 306–308 (1983) (page 81).

161. Frauenfelder, H., Petsko, G. A. & Tsernoglou, D. Temperature-dependent X-ray diffraction as a probe of protein structural dynamics. *Nature* **280,** 558–563 (1979) (page 81).

162. Ni, Q. Z. *et al.* High Frequency Dynamic Nuclear Polarization. *Acc. Chem. Res.* **46,** 1933–1941 (2013) (page 81).

163. Parthasarathy, S., Nishiyama, Y. & Ishii, Y. Sensitivity and Resolution Enhanced Solid-State NMR for Paramagnetic Systems and Biomolecules under Very Fast Magic Angle Spinning. *Acc. Chem. Res.* **46,** 2127–2135 (2013) (page 81).

164. Garman, E. F. Developments in X-ray Crystallographic Structure Determination of Biological Macromolecules. *Science* **343,** 1102–1108 (2014) (page 81).

165. Borbat, P. P. & Freed, J. H. in *Structural Information from Spin-Labels and Intrinsic Paramagnetic Centres in the Biosciences* (eds Timmel, C. R. & Harmer, J. R.) 1–82 (Springer Berlin Heidelberg, Berlin, Heidelberg, 2013) (page 81).

166. Artzi, Y., Twig, Y. & Blank, A. Induction-detection electron spin resonance with spin sensitivity of a few tens of spins. *Appl. Phys. Lett.* **106,** 084104 (2015) (page 81).

167. Bienfait, A. *et al.* Reaching the quantum limit of sensitivity in electron spin resonance. *Nat. Nanotech.* **11,** 253–257 (2016) (page 81).

168. Schlipf, L. *et al.* A molecular quantum spin network controlled by a single qubit. *Science Advances* **3.** eprint: `http://advances.sciencemag.org/content/3/8/e1701116.full.pdf` (2017) (page 82).

169. Schuler, B., Lipman, E. A., Steinbach, P. J., Kumke, M. & Eaton, W. A. Polyproline and the "spectroscopic ruler" revisited with single-molecule fluorescence. *Proc. Natl. Acad. Sci.* **102,** 2754–2759 (2005) (pages 82, 91, 125).

170. Ungar-Waron, H., Gurari, D., Hurwitz, E. & Sela, M. Role of a rigid polyproline spacer inserted between hapten and carrier in the induction of anti-hapten antibodies and delayed hypersensitivity. *Eur. J. Immunol.* **3,** 201–205 (1973) (page 82).

171. Qi, M., Groß, A., Jeschke, G., Godt, A. & Drescher, M. Gd(III)-PyMTA Label Is Suitable for In-Cell EPR. *J. Am. Chem. Soc.* **136,** 15366–15378 (2014) (pages 82, 84, 91).

172. Berliner, L. J., Grunwald, J., Hankovszky, H. & Hideg, K. A novel reversible thiol-specific spin label: Papain active site labeling and inhibition. *Anal. Biochem.* **119,** 450 –455 (1982) (page 82).

173. Borbat, P. P., Costa-Filho, A. J., Earle, K. A., Moscicki, J. K. & Freed, J. H. Electron Spin Resonance in Studies of Membranes and Proteins. *Science* **291,** 266–269 (2001) (page 82).

174. Owenius, R., Engström, M., Lindgren, M. & Huber, M. Influence of Solvent Polarity and Hydrogen Bonding on the EPR Parameters of a Nitroxide Spin Label Studied by 9-GHz and 95-GHz EPR Spectroscopy and DFT Calculations. *The Journal of Physical Chemistry A* **105,** 10967–10977 (2001) (pages 83, 85).

175. Liang, Z., Lou, Y., Freed, J. H., Columbus, L. & Hubbell, W. L. A Multifrequency Electron Spin Resonance Study of T4 Lysozyme Dynamics Using the Slowly Relaxing Local Structure Model. *J. Phys. Chem. B* **108,** 17649–17659 (2004) (page 83).

176. DeSensi, S. C., Rangel, D. P., Beth, A. H., Lybrand, T. P. & Hustedt, E. J. Simulation of Nitroxide Electron Paramagnetic Resonance Spectra from Brownian Trajectories and Molecular Dynamics Simulations. *Biophysical Journal* **94,** 3798 –3809 (2008) (page 86).

177. Sato, H. *et al.* Impact of Electron Electron Spin Interaction on Electron Spin Relaxation of Nitroxide Diradicals and Tetraradical in Glassy Solvents Between 10 and 300 K. *The Journal of Physical Chemistry B* **112.** PMID: 18284225, 2818–2828 (2008) (page 88).

178. Mkami, H. E., Ward, R., Bowman, A., Owen-Hughes, T. & Norman, D. G. The spatial effect of protein deuteration on nitroxide spin-label relaxation: Implications for EPR distance measurement. *Journal of Magnetic Resonance* **248,** 36 –41 (2014) (page 88).

179. Robinson, B. H., Haas, D. A. & Mailer, C. Molecular Dynamics in Liquids: Spin-Lattice Relaxation of Nitroxide Spin Labels. *Science* **263,** 490–493 (1994) (page 88).

180. Pereg-Barnea, T. *et al.* Absolute values of the London penetration depth in $\mathrm{YBa_2Cu_3O_{6+y}}$ measured by zero field ESR spectroscopy on Gd doped single crystals. *Phys. Rev. B* **69,** 184513 (2004) (page 89).

181. Jeschke, G. DEER Distance Measurements on Proteins. *Annu. Rev. Phys. Chem.* **63,** 419–446 (2012) (page 89).

182. Pannier, M, Veit, S, Godt, A, Jeschke, G & Spiess, H. Dead-Time Free Measurement of Dipole–Dipole Interactions between Electron Spins. *J. Magn. Reson.* **142,** 331 –340 (2000) (page 89).

183. Jeschke, G. in *Structural Information from Spin-Labels and Intrinsic Paramagnetic Centres in the Biosciences* (eds Timmel, C. R. & Harmer, J. R.) 83–120 (Springer Berlin Heidelberg, Berlin, Heidelberg, 2013) (page 91).

184. Jeschke, G. *et al.* DeerAnalysis2006 - a comprehensive software package for analyzing pulsed ELDOR data. *Appl. Magn. Reson.* **30,** 473–498 (2006) (page 91).

185. Yunker, P. J., Still, T., Lohr, M. A. & Yodh, A. G. Suppression of the coffee-ring effect by shape-dependent capillary interactions. *Nature* **476,** 308–311 (Aug. 2011) (page 92).

186. Moerner, W. E. & Orrit, M. Illuminating Single Molecules in Condensed Matter. *Science* **283,** 1670–1676 (1999) (page 97).

187. Ruggiero, M. T., Sibik, J., Orlando, R., Zeitler, J. A. & Korter, T. M. Measuring the Elasticity of Poly-l-Proline Helices with Terahertz Spectroscopy. *Angewandte Chemie (International Ed. in English)* **55,** 6877–6881 (Mar. 2016) (pages 99, 102).

188. Mamin, H. J. *et al.* Multipulse Double-Quantum Magnetometry with Near-Surface Nitrogen-Vacancy Centers. *Phys. Rev. Lett.* **113,** 030803 (2014) (page 104).
189. Huang, P. *et al.* Observation of an anomalous decoherence effect in a quantum bath at room temperature. *Nat. Commun.* **2,** 570 (2011) (pages 105, 106).
190. Abragam, A. *The Principles of Nuclear Magnetism* (Oxford University Press, 1983) (page 110).
191. Reinhard, F. *et al.* Tuning a Spin Bath through the Quantum-Classical Transition. *Phys. Rev. Lett.* **108,** 200402 (20 2012) (page 120).
192. Neumann, P. *et al.* Single-Shot Readout of a Single Nuclear Spin. *Science* **329,** 542 (2010) (page 121).
193. Kanase, A. *Fabrication of Next-Generation Scanning Diamond Nanopillars* MA thesis (Universität Stuttgart, 2016) (pages 121, 122).
194. Weidner, F. *Paramagnetic electron-spin network* Bachelor thesis. 2016 (pages 122, 123).
195. Warner, M. *et al.* Potential for spin-based information processing in a thin-film molecular semiconductor. *Nature* **503,** 504–508 (Nov. 2013) (page 122).
196. Abel, M., Clair, S., Ourdjini, O., Mossoyan, M. & Porte, L. Single Layer of Polymeric Fe-Phthalocyanine: An Organometallic Sheet on Metal and Thin Insulating Film. *Journal of the American Chemical Society* **133.** PMID: 21192107, 1203–1205 (2011) (page 123).
197. Dobson, C. M. Protein folding and misfolding. *Nature* **426,** 884–890 (Dec. 2003) (page 124).
198. Norris, J. R., Uphaus, R. A., Crespi, H. L. & Katz, J. J. Electron Spin Resonance of Chlorophyll and the Origin of Signal I in Photosynthesis. *Proceedings of the National Academy of Sciences* **68,** 625–628 (1971) (page 124).
199. Roser, P., Schmidt, M. J., Drescher, M. & Summerer, D. Site-directed spin labeling of proteins for distance measurements in vitro and in cells. *Org. Biomol. Chem.* **14,** 5468–5476 (24 2016) (page 124).
200. Hartmann, S. R. & Hahn, E. L. Nuclear Double Resonance in the Rotating Frame. *Phys. Rev.* **128,** 2042 (5 1962) (page 124).
201. Kucsko, G. *et al.* Nanometre-scale thermometry in a living cell. *Nature* **500,** 54–58 (Aug. 2013) (page 124).

202. Gopinath, A., Miyazono, E., Faraon, A. & Rothemund, P. W. K. Engineering and mapping nanocavity emission via precision placement of DNA origami. *Nature* **535,** 401–405 (2016) (page 124).

203. Luo, Q., Hou, C., Bai, Y., Wang, R. & Liu, J. Protein Assembly: Versatile Approaches to Construct Highly Ordered Nanostructures. *Chem. Rev.* **116,** 13571–13632 (2016) (page 124).

204. Rothemund, P. W. K. Folding DNA to create nanoscale shapes and patterns. *Nature* **440,** 297–302 (2006) (page 124).

205. Barth, J. V., Costantini, G. & Kern, K. Engineering atomic and molecular nanostructures at surfaces. *Nature* **437,** 671–679 (2005) (page 124).

206. Zhu, S.-L. Scaling of Geometric Phases Close to the Quantum Phase Transition in the XY Spin Chain. *Phys. Rev. Lett.* **96,** 077206 (7 2006) (page 125).

207. Marchukov, O. V., Volosniev, A. G., Valiente, M., Petrosyan, D. & Zinner, N. T. Quantum spin transistor with a Heisenberg spin chain. *Nature Communications* **7,** 13070 (Aug. 2016) (page 125).

208. Bose, S. Quantum Communication through an Unmodulated Spin Chain. *Phys. Rev. Lett.* **91,** 207901 (2003) (page 125).

209. Ajoy, A. & Cappellaro, P. Perfect quantum transport in arbitrary spin networks. *Phys. Rev. B* **87,** 064303 (2013) (page 125).

210. Ajoy, A. & Cappellaro, P. Quantum Simulation via Filtered Hamiltonian Engineering: Application to Perfect Quantum Transport in Spin Networks. *Phys. Rev. Lett.* **110,** 220503 (2013) (page 125).

211. Jakobi, I *et al.* Efficient creation of dipolar coupled nitrogen-vacancy spin qubits in diamond. *Journal of Physics: Conference Series* **752,** 012001 (2016) (page 125).

212. Pfender, M., Aslam, N., Waldherr, G., Neumann, P. & Wrachtrup, J. Single-spin stochastic optical reconstruction microscopy. *Proc. Natl. Acad. Sci.* **111,** 14669 (2014) (page 125).

213. Rittweger, E., Han, K. Y., Irvine, S. E., Eggeling, C. & Hell, S. W. STED microscopy reveals crystal colour centres with nanometric resolution. *Nat. Photon.* **3,** 144–147 (Mar. 2009) (page 125).